ISSN No. 0737-5352-25

PROGRESS IN VISIBILITY MODELING

Kirk A. Fuller
Dennis M. O'Brien
Graeme L. Stephens

Research Supported by DOE DE-FG02-90ER61067 &
NPS NOAA-NPS-NA90RAH00077

CIRA Cooperative Institute for Research in the Atmosphere

Colorado State University

ISSN 0737-5352-25

Progress in Visibility Modeling

by

Kirk A. Fuller, Dennis M. O'Brien, and Graeme L. Stephens

Department of Atmospheric Science
Colorado State University
Fort Collins, CO 80523

Research supported by DOE-FG02-90ER61067 & NPS
NOAA-NPS-NA90RAH00077

December 1992

TABLE OF CONTENTS

PROGRESS IN VISIBILITY MODELING

K. A. Fuller, Dennis M. O'Brien
and
Graeme L. Stephens

Department of Atmospheric Science, Colorado State University, Fort Collins, CO 80523

Abstract

The cross section for total scattering by a cluster of spheres is derived from an integration, over a closed spherical surface, of the scattered Poynting flux associated with the different pairs of spheres in the ensemble. With the use of the addition theorem for vector spherical harmonics, the integral can be evaluated analytically. The pair-wise cross sections can be rearranged into an expression for the scattering cross section of sphere aggregates which is analogous to that obtained from Lorenz-Mie theory for a single sphere. This latter formulation, however, is more difficult to treat numerically than is the summation over pair-wise cross sections.

The cross section for total scattering by a cluster of spheres thus derived is applied to a study of the effects of scavenging and aggregation on the specific absorption of carbon. Results are presented for polarization- and orientation-dependent absorption cross sections of sulfate haze elements and cloud droplets with small carbon grains (spheres) attached to their surfaces. Soot typically occurs as aggregates of carbon spherules. In order to address the validity of certain assumptions that are made in the analysis of such structures by fractal theory, comparisons between the absorption cross sections of free carbon, linear chains, and tightly clumped carbon spheres are also provided.

Monte Carlo integration of the radiative transfer equation is the technique most easily adapted to complex scattering geometries. It is demonstrated that the multidimensional integrals can be evaluated more accurately and more efficiently with quasi Monte Carlo integration and that the convergence of the multiple scattering series can be accelerated by estimating the rate of decay of the tail of the series. Each of these techniques has been found to be robust and applicable to scattering with any geometry.

Chapter I. Introduction

Scattering and absorption of electromagnetic (em) radiation by systems wherein two or more spheres may come in contact or in close proximity to one another is relevant to a very broad range of topics. Some examples are surface-enhanced Raman scattering, spectral hole-burning memories, radiative transfer in atmospheres, extinction of microwave signals by planetary rings, propagation of radiation through interplanetary and interstellar dust, combustion diagnostics, and colloid electrooptics. A brief historical review of the study of em scattering by ensembles of closely spaced particles has been recently given by Fuller.[1]

The total scattering cross section, σ_s, of a particle is given by

$$\sigma_s = \int_\Omega \frac{\text{Energy scattered/unit time/unit solid angle}}{\text{Incident energy flux (energy/unit area/unit time)}}\, d\Omega. \tag{1}$$

For a spherical scatterer, this integral can be solved analytically. The response of a *cluster* of spheres to em radiation derives from the natural modes of the individual spheres, but the modes of each sphere couple to those of all other spheres in the ensemble and the mathematical description of the scattered radiation is inherently more complicated than that for isolated spheres. With the use of the addition theorem for vector spherical harmonics (vsh), not only can the scattered fields of the cluster be determined; the σ_s integral can once again be solved analytically. The cross section for total extinction, σ_e, can be found with relative ease from the optical theorem and the absorption cross section of the cluster is simply

$$\sigma_a = \sigma_e - \sigma_s. \tag{2}$$

Without analytic solutions for the cross sections, it is doubtful that the gram-specific absorption efficiencies of small, highly absorbing grains attached to (scavenged by) large, weakly absorbing haze elements or cloud droplets could be calculated.

A review of the Lorenz-Mie treatment of the scattering cross sections of spheres is provided in the next chapter in order to set down, in a more familiar context, definitions and identities that will be used in the study of multisphere systems. That discussion will not assume the high symmetry that would otherwise be appropriate for the treatment of single spheres. This is done in order to make the transition to systems of interacting spheres a bit smoother and to more clearly compare the scattering cross sections of single and multiple sphere systems. Paralleling the theory for single spheres, a theory is then developed for the scattering cross sections of ensembles of spheres. Treatments of this problem have also been rendered by Borghese et al.[2] and by Mackowski.[3] Detailed comparisons of these works and that presented here are best made after a discussion of the theory has been provided and is therefore presented in II.4. For completeness, the addition theorem for vector spherical harmonics, as it pertains to the determination of scattering cross sections, is provided in the Appendix.

In terms of number density, the atmospheric aerosol is dominated by a submicron fraction comprised mainly of sulfate species and light-absorbing carbon (soot). These particles not only degrade visibility, but are likely, to some degree, to influence climate. The ubiquity of soot

and its dominance as an absorber of visible radiation in the atmosphere are well known. In anthropogenic haze, individual haze elements frequently occur in the form of sulfate/soot composite particles. For example, recent work by Podzimek[4] indicates that in a polluted urban-marine environment one can encounter haze droplets containing insoluble inclusions and with small particles deposited on their surfaces. The concentration of insoluble attached particles was found to be comparable to the number of insoluble particles moving freely in air. In the above study, it was estimated that the carbon content of the haze was $\approx 1.4\ \mu g/m^3$, that internally mixed particles accounted for between $1.5 - 10\%$ of the aerosol "surface area," and that surface contaminants accounted for between $2 - 9\%$ of the aerosol "surface area." The occurrence of carbon on or within cloud droplets is of interest as a possible contributor to the so-called cloud absorption anomaly.[5] Light-absorbing carbon may also attach itself to dust grains. Soot, in turn, typically occurs as clusters of carbon spherules. Until recently, no radiation models existed which could explicitly account for the effects of aggregation and scavenging on the absorption efficiency of carbon because no comprehensive treatment of scattering and absorption by particles with the relevant morphologies was available.

Numerical studies of the modification of scattering and absorption cross sections of atmospheric carbon grains by scavenging have been conducted based on the theory presented in Chapter II and will be discussed in Chapter III.

Given the importance of Monte Carlo methods in visibility modeling, research into improving the efficiency of Monte Carlo integration of the radiative transfer equation has been conducted. This work has already been published [D. M. O'Brien, "Accelerated quasi Monte Carlo integration of the radiative transfer equation," J. Quant. Spectrosc. Radiat. Transfer **48**, 41-59(1992)]. For completeness, a copy of this article has been included here as Chapter IV, with consequent independent numbering of equations, figures, tables, and references.

Chapter II. Scattering and Absorption Cross Sections of Compounded Spheres—Theory

II.2. Cross Sections for a Single Sphere: Reduced Symmetry Case

II.2.A. The scattered electric fields

The ability of a particle to scatter light depends upon its characteristic size, x, its refractive index $N(\lambda)$, and the wavelength, λ, of the incident light *in vacuo*. Parameters of the form kx and Nkx ($k = 2\pi/\lambda$) are typically used to describe the 'optical' dimensions of the scattering system. For a sphere, x is simply its radius, a.

The scattering geometry is depicted in Fig. 1. Rather than restricting the wave vector, $\mathbf{k}_0$, of the incident radiation to be parallel to $\hat{\mathbf{e}}_z$, we will require only that it lie in the the xz-plane, oriented at an angle α from the z-axis. The angle γ specifies the polarization of the incident field $\mathbf{E}_0$. The incident fields are expanded in the vector space spanned by the vector spherical harmonics, $\mathbf{N}_{mn}^{(j)}$ and $\mathbf{M}_{mn}^{(j)}$, where wave functions with superscripts (1) and (3) depend radially on the spherical Bessel functions, $j_n(kr)$ and the spherical Hankel functions of the first kind, $h_n^{(1)}(kr)$, respectively. The Ricatti-Bessel functions are often encountered in light scattering and are here defined by the relations $\zeta_n(x) = xj_n(x)$ and $\xi_n(x) = xh_n^{(1)}(x)$. Explicit expressions for the vsh are

$$\mathbf{M}_{mn}^{(j)} = \left(M\Theta_{mn}^{(j)} \hat{\mathbf{e}}_\theta + M\Phi_{mn}^{(j)} \hat{\mathbf{e}}_\phi \right) \exp(\imath m\phi) \tag{3}$$

$$\mathbf{N}_{mn}^{(j)} = \left(NR_{mn}^{(j)} \hat{\mathbf{e}}_r + N\Theta_{mn}^{(j)} \hat{\mathbf{e}}_\theta + N\Phi_{mn}^{(j)} \hat{\mathbf{e}}_\phi \right) \exp(\imath m\phi), \tag{4}$$

where, for example, if $j = 3$

$$M\Theta_{mn}^{(3)} = \frac{\imath\, \xi_n(kr)}{kr} \pi_{mn}(\cos\theta) \tag{5}$$

$$M\Phi_{mn}^{(3)} = -\frac{\xi_n(kr)}{kr} \tau_{mn}(\cos\theta) \tag{6}$$

$$NR_{mn}^{(3)} = \frac{\xi_n(kr)}{(kr)^2} n(n+1) P_n^m(\cos\theta) \tag{7}$$

$$N\Theta_{mn}^{(3)} = \frac{\xi_n'(kr)}{kr} \tau_{mn}(\cos\theta) \tag{8}$$

$$N\Phi_{mn}^{(3)} = \frac{\imath\, \xi_n'(kr)}{kr} \pi_{mn}(\cos\theta), \tag{9}$$

with

$$\pi_{mn}(\cos\theta) = \frac{m}{\sin\theta} P_n^m(\cos\theta), \tag{10}$$

$$\tau_{mn}(\cos\theta) = \frac{d}{d\,\theta} P_n^m(\cos\theta). \tag{11}$$

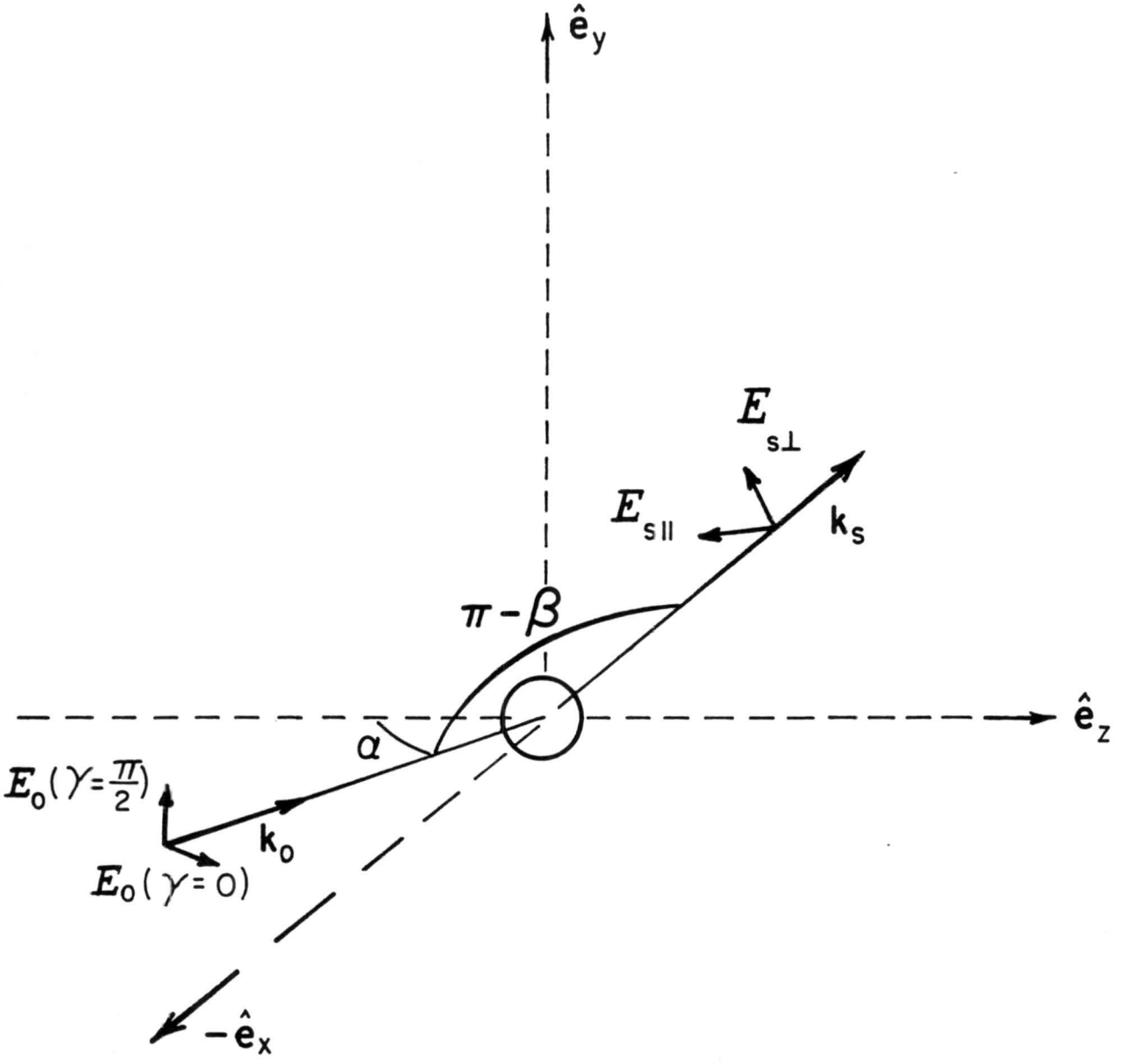
$\hat{e}_y$
$E_{s\perp}$
$E_{s\parallel}$
k_s
$\pi - \beta$
$\hat{e}_z$
α
$E_0(\gamma = \frac{\pi}{2})$
k_0
$E_0(\gamma = 0)$
$-\hat{e}_x$

$P_n^m(\cos\theta)$ are the associated Legendre functions of order n and degree m. The primes indicate differentiation with respect to the argument.

The sign convention to be adopted here is prescribed by the propagation factor $\exp(\imath\mathbf{k}\cdot\mathbf{r}-\imath\omega t)$, and the harmonic time dependence will be suppressed henceforth. Restriction of $\mathbf{k}_0$ to the xz-plane results in a significant simplification of the coefficients involved in the plane wave expansion, without loss of generality, giving

$$\mathbf{E}_0\exp(\imath\mathbf{k}_0\cdot\mathbf{r}) = |\mathbf{E}_0|\sum_{n=1}^{\infty}\sum_{m=-n}^{n}\left(p_{mn}\mathbf{N}_{mn}^{(1)}+q_{mn}\mathbf{M}_{mn}^{(1)}\right), \tag{12}$$

where p_{mn} and q_{mn} are of the form

$$p_{mn} = -\imath^n\frac{2n+1}{n(n+1)}\frac{(n-m)!}{(n+m)!}\begin{bmatrix}-\imath\tau_{mn}(\cos\alpha)\\ \pi_{mn}(\cos\alpha)\end{bmatrix}, \quad \gamma=\begin{bmatrix}0\\ \pi/2\end{bmatrix} \tag{13}$$

and

$$q_{mn} = \imath^n\frac{2n+1}{n(n+1)}\frac{(n-m)!}{(n+m)!}\begin{bmatrix}\imath\pi_{mn}(\cos\alpha)\\ -\tau_{mn}(\cos\alpha)\end{bmatrix}, \quad \gamma=\begin{bmatrix}0\\ \pi/2\end{bmatrix}. \tag{14}$$

Recursion relations for τ_{mn}, π_{mn}, p_{mn}, and q_{mn} have been worked out by Fuller.[6]

In Fig. 1, radiation is scattered into an angle β, relative to the $\mathbf{k}_0$ direction, with polarization components $\mathbf{E}_{s\|}$ and $\mathbf{E}_{s\perp}$ that are, respectively, parallel and perpendicular to the plane swept out by the scattering angle. The scattered field can be expanded as

$$\mathbf{E}_s = |\mathbf{E}_0|\sum_{n=1}^{\infty}\sum_{m=-n}^{n}\left(AE_{mn}\mathbf{N}_{mn}^{(3)}+AH_{mn}\mathbf{M}_{mn}^{(3)}\right), \tag{15}$$

where the expansion coefficients AE_{mn} and AH_{mn} correspond, respectively, to the transverse magnetic (TM) and transverse electric (TE) modes of the sphere. For a single sphere, these take on the form

$$\begin{aligned} AE_{mn} &= p_{mn}\,a_n \\ AH_{mn} &= q_{mn}\,b_n, \end{aligned} \tag{16}$$

where a_n and b_n are the familiar amplitude coefficients of Lorenz-Mie theory:

$$\begin{aligned} a_n &= \frac{N\psi_n'(\varrho)\,\psi_n(\eta)-\psi_n(\varrho)\,\psi_n'(\eta)}{N\xi_n'(\varrho)\,\psi_n(\eta)-\xi_n(\varrho)\,\psi_n'(\eta)} \\ b_n &= \frac{N\psi_n(\varrho)\,\psi_n'(\eta)-\psi_n'(\varrho)\,\psi_n(\eta)}{N\xi_n(\varrho)\,\psi_n'(\eta)-\xi_n'(\varrho)\,\psi_n(\eta)}, \end{aligned} \tag{17}$$

with ϱ and η representing ka and Nka, respectively. The expansion of the scattered field in the highest symmetry case, i.e., when $\mathbf{k}_0 \parallel \hat{\mathbf{e}}_z$, can be recovered as follows: Write $P_n^m(x)$ and, subsequently, τ_{mn} and π_{mn} as hypergeometric functions[7] and let $x \to 1$. It is seen that

$$\begin{aligned} P_n^m(\pm 1) &= (\pm 1)^n \, \delta_{0,m} \\ \tau_{mn}(\pm 1) &= (\pm)^{n+1} \, \frac{n}{2}(n+1)\delta_{1,m} \\ \pi_{mn}(\pm 1) &= -(\pm)^n \, \frac{n}{2}(n+1)\delta_{1,m}, \end{aligned} \tag{18}$$

where $\delta_{l,m}$ is the Kronecker delta symbol. Now,

$$P_n^{-m} = (-1)^m \, (n,m) \, P_n^m, \tag{19}$$

where $(n,m) = (n-m)!/(n+m)!$, and hence

$$\begin{aligned} \tau_{-m,n} &= -(-1)^m \, (n,m) \tau_{mn} \\ \pi_{-m,n} &= (-1)^m \, (n,m) \pi_{mn}. \end{aligned} \tag{20}$$

If $\gamma = \pi/2$ then

$$\begin{aligned} p_{-m,n} &= -(-1)^m \, (n,-m) p_{mn}, \\ q_{-m,n} &= (-1)^m \, (n,-m) q_{mn}, \end{aligned} \tag{21}$$

and if $\gamma = 0$ then

$$\begin{aligned} p_{-m,n} &= (-1)^m \, (n,-m) p_{mn}, \\ q_{-m,n} &= -(-1)^m \, (n,-m) q_{mn}. \end{aligned} \tag{22}$$

The expansion of the scattered fields now simplifies to

$$\mathbf{E}_s = |\mathbf{E}_0| \sum_{n=1}^{\infty} \imath^n \frac{2n+1}{n(n+1)} \left(\imath a_n \mathbf{N}_{e1n}^{(3)} - b_n \mathbf{M}_{o1n}^{(3)} \right), \tag{23}$$

for -$\hat{\mathbf{e}}_x$ polarization. This is the form that one commonly encounters when the scattering properties of isolated spheres are of interest.[8]

II.2.B. The cross sections

The differential scattering cross section of a particle is defined as

$$\frac{d\sigma}{d\Omega} = \frac{\text{Energy scattered/unit time/unit solid angle}}{\text{Incident energy flux (energy/unit area/unit time)}}. \tag{24}$$

The total scattering cross section, σ_s, is then found from

$$\sigma_s = \frac{1}{|\langle \mathbf{S}_0 \rangle|} \frac{1}{2} Re \int_0^{2\pi} \int_0^{\pi} \langle \mathbf{E}_s \times \mathbf{H}_s^* \rangle \cdot \hat{\mathbf{e}}_r \; r^2 \sin\theta \, d\theta \, d\phi, \tag{25}$$

where $\mathbf{S}_0 = \mathbf{E}_0 \times \mathbf{H}_0^*$ is the Poynting flux of the incident field and $<>$ represents a time average over an interval that is much larger than the period of the stimulating radiation. The extinction cross section may be found from the optical theorem, viz.,

$$\sigma_e = \frac{4\pi}{k^2} Re(\mathbf{E}_s(0) \cdot \hat{\mathbf{e}}_\theta), \tag{26}$$

and by conservation of energy, the absorption cross section is

$$\sigma_a = \sigma_e - \sigma_s. \tag{27}$$

By integrating Eq. (25) over an imaginary spherical surface that is concentric with the scatterer, it can be shown that the scattering cross section of a sphere is

$$\sigma_s = \frac{2\pi}{k^2} \sum_{n=1}^{\infty} (2n+1)(|a_n|^2 + |b_n|^2). \tag{28}$$

Once again, it will prove useful to carry out this analysis for an angle of incidence, $\alpha \neq 0$. In the abscence of free charge and current densities, the free space Maxwell's equations for time-harmonic fields lead to

$$\mathbf{H}_s = \frac{-\imath}{\omega \mu_0} \nabla \times \mathbf{E}_s. \tag{29}$$

The vsh have the property

$$\nabla \times \mathbf{M}_{mn} = k\mathbf{N}_{mn} \text{ and } \nabla \times \mathbf{N}_{mn} = k\mathbf{M}_{mn}. \tag{30}$$

Thus

$$\mathbf{H}_s^* = |\mathbf{E}_0| \frac{\imath k}{\omega \mu_0} \sum_{n=1}^{\infty} \sum_{m=-n}^{n} \left(A H_{mn}^* (\mathbf{N}_{mn}^{(3)})^* + A E_{mn}^* (\mathbf{M}_{mn}^{(3)})^* \right), \tag{31}$$

and

$$\sigma_s = \int_0^{2\pi} \int_0^{\pi} Re \Bigg[\imath \sum_{n=1}^{\infty} \sum_{m=-n}^{n} \left(A E_{mn} (\mathbf{N}_{mn}^{(3)}) + A H_{mn} (\mathbf{M}_{mn}^{(3)}) \right) \times \sum_{n'=1}^{\infty} \sum_{m'=-n'}^{n'} \left(A H_{m'n'}^* (\mathbf{N}_{m'n'}^{(3)})^* + A E_{m'n'}^* (\mathbf{M}_{m'n'}^{(3)})^* \right) \Bigg] \cdot \hat{\mathbf{e}}_r \; r^2 \sin\theta \, d\theta \, d\phi. \tag{32}$$

In carrying out the above integration, it is noted that

$$\oint \left(\mathbf{N}_{m,n} \times \mathbf{N}^*_{m',n'}\right) \cdot \hat{\mathbf{e}}_r \, r^2 \sin\theta \, d\theta \, d\phi = \oint \left(\mathbf{M}_{m,n} \times \mathbf{M}^*_{m',n'}\right) \cdot \hat{\mathbf{e}}_r \, r^2 \sin\theta \, d\theta \, d\phi = 0 \tag{33}$$

and

$$\oint \left(\mathbf{N}_{m,n} \times \mathbf{M}^*_{m',n'}\right) \cdot \hat{\mathbf{e}}_r \, r^2 \sin\theta \, d\theta \, d\phi = -\oint \left(\mathbf{M}_{m',n'} \times \mathbf{N}^*_{m,n}\right) \cdot \hat{\mathbf{e}}_r \, r^2 \sin\theta \, d\theta \, d\phi = \mathcal{N}(m,n), \tag{34}$$

where

$$\mathcal{N}(m,n) = \frac{-4\pi\imath}{k^2} \frac{n(n+1)}{2n+1)} \frac{(n+m)!}{(n-m)!} \xi^*_n \xi'_n \delta_{m,m'} \delta_{n,n'}. \tag{35}$$

As noted by Bohren and Huffman,[6] the Wronskian of the spherical Bessel and Neuman functions leads to

$$Re(\imath \xi^*_n \xi'_n) = -1, \tag{36}$$

and thus

$$\sigma_s = \frac{4\pi}{k^2} \sum_{n=1}^{\infty} \sum_{m=-n}^{n} \frac{n(n+1)}{(2n+1)} \frac{(n+m)!}{(n-m)!} \left(|AE_{mn}|^2 + |AH_{mn}|^2 \right) \tag{37}$$

II.3. Cross Sections for Sphere Aggregates

Having established the mathematical form of the total scattering cross section of a sphere with a scattering geometry that does not exploit the symmetry of a single sphere, one can now make the transition to scattering by clusters. The scattering geometry for such a case is depicted in Fig. 2. The spheres in the cluster are centered about the ${}^{\ell}O$ origins, where ℓ is an index that identifies specific constituents of a set of L spheres. Let the position vector that locates the observer with respect to the ℓth sphere be given by

$${}^{\ell}\mathbf{r} = {}^{\ell}r \, {}^{\ell}\hat{\mathbf{e}}_r + {}^{\ell}\theta \, {}^{\ell}\hat{\mathbf{e}}_\theta + {}^{\ell}\phi \, {}^{\ell}\hat{\mathbf{e}}_\phi, \tag{38}$$

where, for example, ${}^{\ell}\hat{\mathbf{e}}_r$ is a unit vector in the ℓth coordinate frame and points in the ${}^{\ell}\mathbf{r}$ direction. Henceforth, the dimensionless position vector $k\,{}^{\ell}\mathbf{r}$ will be used. In Fig. 2, the unit vectors associated with the ℓ'th origin have been displaced from the ${}^{\ell'}x\,{}^{\ell'}y$-plane to the ${}^{\ell}x\,{}^{\ell}y$-plane. The constituent spheres (with radii ${}^{\ell}a$) are now characterized by the size parameter $k\,{}^{\ell}a \equiv {}^{\ell}\wp$ and complex refractive index ${}^{\ell}N$. The dimensionless center-to-center distance between spheres ℓ and ℓ' is denoted by $kd_{\ell,\ell'}$. The principal or primary coordinate sytem will be that in which the integration of the Poynting flux is carried out and coincides to the case $\ell = 1$. It will be convenient in such instances to visualize ${}^{\ell}O$ in Fig. 2 as the origin of this system, and any other ${}^{\ell'}O$, $\ell' \neq 1$ as a secondary origin. The $L-1$ secondary coordinate systems are related to the principal coordinate system by pure translations.

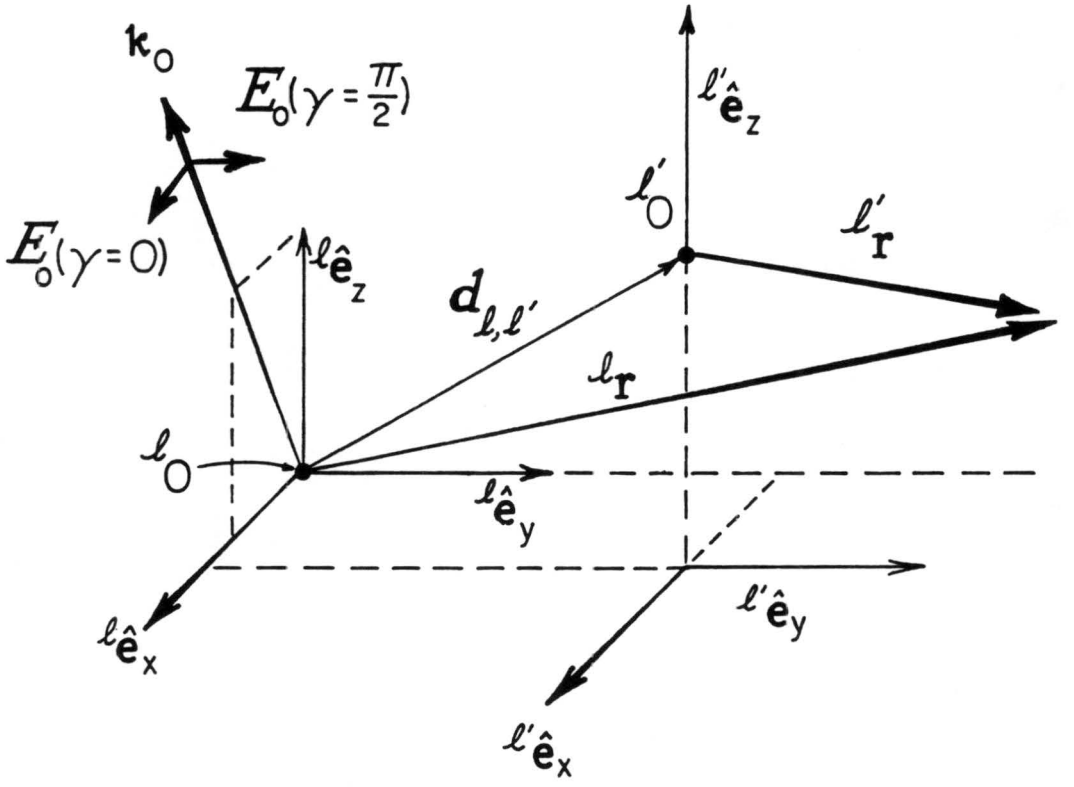
k_0
$E_0(\gamma = \frac{\pi}{2})$
$E_0(\gamma = 0)$
$\ell\hat{e}_z$
$d_{\ell,\ell'}$
$\ell'\hat{e}_z$
ℓ'_0
ℓ'_r
ℓ_r
ℓ_0
$\ell\hat{e}_y$
$\ell\hat{e}_x$
$\ell'\hat{e}_y$
$\ell'\hat{e}_x$

II.3.A. The scattered fields

The first definitive solution to the problem of scattering by more than one sphere was obtained by Bruning and Lo,[9] and theirs is the notation adopted here. The scattered fields are expanded as

$$\begin{aligned}\mathbf{E}_s &= \sum_{n=1}^{\infty}\sum_{m=-n}^{n}\sum_{\ell=1}^{L}\left({}^{\ell}AE_{mn}\,{}^{\ell}\mathbf{N}_{mn}^{(3)} + {}^{\ell}AH_{mn}\,{}^{\ell}\mathbf{M}_{mn}^{(3)}\right) \\ &= \sum_{\ell=1}^{L}{}^{\ell}\mathbf{E}_s\end{aligned}, \tag{39}$$

where the expansion coefficients ${}^{\ell}AE_{mn}$ and ${}^{\ell}AH_{mn}$ correspond, respectively, to the TM and TE modes of the ℓth sphere, and ${}^{\ell}\mathbf{N}_{mn}^{(3)}$ and ${}^{\ell}\mathbf{M}_{mn}^{(3)}$ are the vector spherical harmonics in the ℓth coordinate system.

In order to apply boundary conditions successfully, one must be able to expand the fields scattered by the ℓ'th sphere about the center of any ℓth constituent of the cluster. This can be accomplished through the use of the addition theorem for vector spherical harmonics[10,11] which states, in part, that

$$\begin{aligned}{}^{\ell'}\mathbf{M}_{mn}^{(3)} &= \sum_{\nu=1}^{\infty}\sum_{\mu=-\nu}^{\nu}\left({}^{\ell}\mathbf{M}_{\mu\nu}^{(1)}A_{\mu\nu}^{mn}(k\mathbf{d}_{\ell',\ell}) + {}^{\ell}\mathbf{N}_{\mu\nu}^{(1)}B_{\mu\nu}^{mn}(k\mathbf{d}_{\ell',\ell})\right) \\ {}^{\ell'}\mathbf{N}_{mn}^{(3)} &= \sum_{\nu=1}^{\infty}\sum_{\mu=-\nu}^{\nu}\left({}^{\ell}\mathbf{N}_{\mu\nu}^{(1)}A_{\mu\nu}^{mn}(k\mathbf{d}_{\ell',\ell}) + {}^{\ell}\mathbf{M}_{\mu\nu}^{(1)}B_{\mu\nu}^{mn}(k\mathbf{d}_{\ell',\ell})\right).\end{aligned} \tag{40}$$

The translation coefficients $A_{\mu\nu}^{mn}(k\mathbf{d}_{\ell',\ell})$ and $B_{\mu\nu}^{mn}(k\mathbf{d}_{\ell',\ell})$ are a rather complicated function of Clebsch-Gordan coefficients and of the geometry of the cluster. It is seen from the Appendix that $A_{\mu\nu}^{mn}(k\mathbf{d}_{\ell,\ell'}) = (-1)^{n+\nu}A_{\mu\nu}^{mn}(k\mathbf{d}_{\ell',\ell})$ and $B_{\mu\nu}^{mn}(k\mathbf{d}_{\ell,\ell'}) = -(-1)^{n+\nu}B_{\mu\nu}^{mn}(k\mathbf{d}_{\ell',\ell})$.

By applying the condition that at any surface the tangential components of both the total electric and the total magnetic field strengths must be continuous in conjunction with the above addition theorem, one is led to the following set of $2L$ coupled linear equations involving the (as yet undetermined) scattering coefficients:

$${}^{\ell}AE_{mn} = {}^{\ell}a_n\left[{}^{\ell}p_{mn} + \sum_{\ell'\neq\ell}\sum_{\nu}\sum_{\mu}\left({}^{\ell'}AE_{\mu\nu}A_{mn}^{\mu\nu} + {}^{\ell'}AH_{\mu\nu}B_{mn}^{\mu\nu}\right)\right] \tag{41}$$

$${}^{\ell}AH_{mn} = {}^{\ell}b_n\left[{}^{\ell}q_{mn} + \sum_{\ell'\neq\ell}\sum_{\nu}\sum_{\mu}\left({}^{\ell'}AH_{\mu\nu}A_{mn}^{\mu\nu} + {}^{\ell'}AE_{\mu\nu}B_{mn}^{\mu\nu}\right)\right]. \tag{42}$$

The coefficients of the plane wave expansion about an ℓth secondary origin are obtained by simply multiplying ${}^{1}p_{mn}$ and ${}^{1}q_{mn}$ by the phase factor $\exp(\imath\,\mathbf{k}_0\cdot\mathbf{d}_{1,\ell})$. Eq. (42) can be cast in

the form of a matrix equation in which the translation coefficients give rise to the coefficient matrix, and the scattering coefficients can then be found by direct matrix inversion.

Alternatively, the scattering coefficients may be found by the order-of-scattering (OS) mehtod of Fuller and Kattawar.[12,13] For ease of visualization, the following description is limited to just two spheres, but the extension to clusters of three or more is straightforward. The OS process can be visualized as follows: First, plane wave radiation strikes one sphere which then scatters a field (as prescribed by the standard Lorenz-Mie theory) both to the field point and to the other sphere. This second sphere then responds to the field incident on it from the first sphere, scattering radiation to the field point and back to the first sphere. This process is continued indefinitely, and the total scattered field is obtained as a vector sum of these partial fields plus a sum of of the partial fields which arise from plane wave radiation incident on the second sphere.

The total field scattered by the pair is thus

$$\sum_{j=0}^{\infty}\sum_{\ell=1}^{L} {}^{\ell}\mathbf{E}_s^{(j)}, \tag{43}$$

where the jth-order partial fields ${}^{\ell}\mathbf{E}_s^{(j)}$ are in turn expressed as

$${}^{\ell}\mathbf{E}_s^{(j)} = \sum_{n,m}\left({}^{\ell}a_{mn}^{(j)}\, {}^{\ell}\mathbf{N}_{mn}^{(3)} + {}^{\ell}b_{mn}^{(j)}\, {}^{\ell}\mathbf{M}_{mn}^{(3)} \right). \tag{44}$$

From here, one follows the same routine as was used to derive Eqs. (41) and (42) to arrive at, for the case of two spheres,

$$\begin{aligned}
{}^{1}a_{mn}^{(j)} &= {}^{1}a_n \sum_{\nu}\sum_{\mu}\left({}^{2}a_{\mu\nu}^{(j-1)} A_{mn}^{\mu\nu} + {}^{2}b_{\mu\nu}^{(j-1)} B_{mn}^{\mu\nu} \right) \\
{}^{1}b_{mn}^{(j)} &= {}^{1}b_n \sum_{\nu}\sum_{\mu}\left({}^{2}b_{\mu\nu}^{(j-1)} A_{mn}^{\mu\nu} + {}^{2}a_{\mu\nu}^{(j-1)} B_{mn}^{\mu\nu} \right) \\
{}^{2}a_{mn}^{(j)} &= {}^{2}a_n \sum_{\nu}\sum_{\mu}\left({}^{1}a_{\mu\nu}^{(j-1)} A_{mn}^{\mu\nu} + {}^{1}b_{\mu\nu}^{(j-1)} B_{mn}^{\mu\nu} \right) \\
{}^{2}b_{mn}^{(j)} &= {}^{2}b_n \sum_{\nu}\sum_{\mu}\left({}^{1}b_{\mu\nu}^{(j-1)} A_{mn}^{\mu\nu} + {}^{1}a_{\mu\nu}^{(j-1)} B_{mn}^{\mu\nu} \right).
\end{aligned} \tag{45}$$

In addition to quantifying the partial fields which combine to produce the net scattered field, Eq. (45) allows one to see exactly what role each of the νth-degree, μth-order ${}^{1}a_{\mu\nu}^{(j-1)}$ and ${}^{1}b_{\mu\nu}^{(j-1)}$ modes arriving from sphere 1 play in stimulating the nth-degree, mth-order ${}^{2}a_{mn}^{(j)}$

and ${}^2b_{mn}^{(j)}$ modes in sphere 2 for any jth order of scattering. The expansion coefficients of the total scattered field are then given by

$$\begin{aligned} {}^{\ell}AE_{mn} &= \sum_{j=0}^{\infty} {}^{\ell}a_{mn}^{(j)} \\ {}^{\ell}AH_{mn} &= \sum_{j=0}^{\infty} {}^{\ell}b_{mn}^{(j)}. \end{aligned} \tag{46}$$

As noted in the following chapter, the OS method has proven to be especially important in the efficient calculation of the scattering cross sections associated with large, lossless droplets that have small carbon grains attached to their surfaces.

II.3.B. The cross sections

In order to determine the total power, W, radiated from a surface Σ enclosing an ensemble of scatterers, the integral

$$\int_{\Sigma} \mathbf{S} \cdot \hat{\mathbf{r}}\, r^2 \sin\theta d\theta d\phi = \int_{\Sigma} (\mathbf{E} \times \mathbf{H}^*) \cdot \hat{\mathbf{r}}\, r^2 \sin\theta d\theta d\phi \tag{47}$$

must be evaluated, where, for a system of L particles,

$$\mathbf{E} = \mathbf{E}_0 + \sum_{\ell=1}^{L} {}^{\ell}\mathbf{E}_s \tag{48}$$

and

$$\mathbf{H} = \mathbf{H}_0 + \sum_{\ell=1}^{L} {}^{\ell}\mathbf{H}_s. \tag{49}$$

The radiated power is thus

$$\begin{aligned} W = &\sum_{\ell} \int_{\Sigma} (\mathbf{E}_0 \times {}^{\ell}\mathbf{H}_s^* + {}^{\ell}\mathbf{E}_s \times \mathbf{H}_0^*) \cdot \hat{\mathbf{e}}_r\, r^2 \sin\theta\, d\theta\, d\phi \\ &+ \sum_{\ell} \int_{\Sigma} ({}^{\ell}\mathbf{E}_s \times {}^{\ell}\mathbf{H}_s^*) \cdot \hat{\mathbf{e}}_r\, r^2 \sin\theta\, d\theta\, d\phi \\ &+ \sum_{\ell} \sum_{\ell' \neq \ell} \int_{\Sigma} ({}^{\ell}\mathbf{E}_s \times {}^{\ell'}\mathbf{H}_s^*) \cdot \hat{\mathbf{e}}_r\, r^2 \sin\theta\, d\theta\, d\phi \end{aligned} \tag{50}$$

The first integral in Eq. (50) represents the interference between the incident electromagnetic field and the fields scattered by each of the monomers in the system. As in the case

of a single particle, this interference term corresponds to the total power removed from the incident beam. The evaluation of this integral will not be pursued at this time since the extinction cross section is readily found from the optical theorem. The second integral is equal to the total power scattered by the ℓth sphere while the third integral accounts for the fact that relative phases of the fields of the ℓth and ℓ'th scatterers will vary over the surface of integration, contributing further to the scattering cross section of the ensemble. The surface of integration is henceforth assumed to be a sphere centered about the principal origin.

The equation for the total scattering cross section is thus

$$|\langle \mathbf{S}_0 \rangle| \sigma_s = \frac{1}{2} Re \sum_{\ell} \sum_{\ell'} \int_0^{2\pi} \int_0^{\pi} ({}^{\ell}\mathbf{E}_s \times {}^{\ell'}\mathbf{H}_s^*) \cdot \hat{\mathbf{e}}_r \, r^2 \sin\theta \, d\theta \, d\phi. \tag{51}$$

It is noted that the integration is to be carried out in one set of coordinates, but ${}^{\ell}\mathbf{E}_s$ is referenced to a second coordinate system and ${}^{\ell'}\mathbf{H}_s$ is referenced to a yet another. The notation

$$\sigma_s = \sum_{\ell} \sum_{\ell'} {}^{\ell\ell'}\sigma_s \tag{52}$$

is now introduced.

In principle, one could simply evaluate

$$\sigma_s = \int_0^{2\pi} \int_0^{\pi} \left(\sum_{\ell} {}^{\ell}\mathbf{E}_s \times \sum_{\ell'} {}^{\ell'}\mathbf{H}_s^* \right) \cdot \hat{\mathbf{e}}_r \, r^2 \sin\theta \, d\theta \, d\phi \tag{53}$$

numerically but this provides only a rather limited solution to the problem.

Use is once again made of the addition theorem. In Eq (39), it is to be understood that the transformation of coordinates is carried out at the surfaces of the scatterers and thus $k^{\ell}r < kd_{\ell\ell'}$. In this case, the dependence of the translation coefficients on the distances between spheres is governed by spherical Hankel functions. When evaluating the integrals over a surface that contains all scatterers in the collection, $k^{\ell}r > kd_{\ell\ell'}$. The dependence on $kd_{\ell\ell'}$ is, in this case, governed by spherical Bessel functions and the corresponding translation coefficients are here denoted as $\widetilde{A}_{\mu\nu}^{mn}(k\mathbf{d}_{\ell',\ell})$ and $\widetilde{B}_{\mu\nu}^{mn}(k\mathbf{d}_{\ell',\ell})$. The addition theorem takes the form

$$\begin{aligned} {}^{\ell'}\mathbf{M}_{mn}^{(3)} &= \sum_{\nu=1}^{\infty} \sum_{\mu=-\nu}^{\nu} \left({}^{\ell}\mathbf{M}_{\mu\nu}^{(3)} \widetilde{A}_{\mu\nu}^{mn}(k\mathbf{d}_{\ell',\ell}) + {}^{\ell}\mathbf{N}_{\mu\nu}^{(3)} \widetilde{B}_{\mu\nu}^{mn}(k\mathbf{d}_{\ell',\ell}) \right) \\ {}^{\ell'}\mathbf{N}_{mn}^{(3)} &= \sum_{\nu=1}^{\infty} \sum_{\mu=-\nu}^{\nu} \left({}^{\ell}\mathbf{N}_{\mu\nu}^{(3)} \widetilde{A}_{\mu\nu}^{mn}(k\mathbf{d}_{\ell',\ell}) + {}^{\ell}\mathbf{M}_{\mu\nu}^{(3)} \widetilde{B}_{\mu\nu}^{mn}(k\mathbf{d}_{\ell',\ell}) \right). \end{aligned} \tag{54}$$

The scattered fields of each sphere can thus be expressed in terms of the basis functions of

the principal origin, viz.,

$$
\begin{aligned}
{}^{\ell}\mathbf{E}_s = & \sum_{n=1}^{\infty}\sum_{m=-n}^{n} \\
& \left[{}^{\ell}A E_{mn}\sum_{\nu=1}^{\infty}\sum_{\mu=-\nu}^{\nu}\left({}^{1}\mathbf{N}_{\mu\nu}^{(3)}\widetilde{A}_{\mu\nu}^{mn}(k\mathbf{d}_{\ell,1})+{}^{1}\mathbf{M}_{\mu\nu}^{(3)}\widetilde{B}_{\mu\nu}^{mn}(k\mathbf{d}_{\ell,1})\right)\right. \\
& \left.+{}^{\ell}A H_{mn}\sum_{\nu=1}^{\infty}\sum_{\mu=-\nu}^{\nu}\left({}^{1}\mathbf{N}_{\mu\nu}^{(3)}\widetilde{B}_{\mu\nu}^{mn}(k\mathbf{d}_{\ell,1})+{}^{1}\mathbf{M}_{\mu\nu}^{(3)}\widetilde{A}_{\mu\nu}^{mn}(k\mathbf{d}_{\ell,1})\right)\right]
\end{aligned}
\tag{55}
$$

and

$$
\begin{aligned}
{}^{\ell'}\mathbf{H}_s^{*} = & \frac{\imath k}{\omega\mu_0}\sum_{n=1}^{\infty}\sum_{m=-n}^{n} \\
& \left[{}^{\ell'}A H_{mn}^{*}\sum_{\nu=1}^{\infty}\sum_{\mu=-\nu}^{\nu}\left({}^{1}\mathbf{N}_{\mu\nu}^{(3)}\widetilde{A}_{\mu\nu}^{mn}(k\mathbf{d}_{\ell',1})+{}^{1}\mathbf{M}_{\mu\nu}^{(3)}\widetilde{B}_{\mu\nu}^{mn}(k\mathbf{d}_{\ell',1})\right)^{*}\right. \\
& \left.+{}^{\ell'}A E_{mn}^{*}\sum_{\nu=1}^{\infty}\sum_{\mu=-\nu}^{\nu}\left({}^{1}\mathbf{N}_{\mu\nu}^{(3)}\widetilde{B}_{\mu\nu}^{mn}(k\mathbf{d}_{\ell',1})+{}^{1}\mathbf{M}_{\mu\nu}^{(3)}\widetilde{A}_{\mu\nu}^{mn}(k\mathbf{d}_{\ell',1})\right)^{*}\right].
\end{aligned}
\tag{56}
$$

The summations in the addition theorem are uniformly convergent and the series can therefore be integrated term-by-term, giving

$$
\begin{aligned}
{}^{\ell\ell'}\sigma_s = & \frac{4\pi}{k^2}Re\sum_{m,n}\sum_{\mu,\nu}\frac{\nu(\nu+1)(\nu+\mu)!}{(2\nu+1)(\nu-\mu)!}\times \\
& \left[\left({}^{\ell}A E_{mn}\,{}^{\ell'}A E_{\mu\nu}^{*}+{}^{\ell}A H_{mn}\,{}^{\ell'}A H_{\mu\nu}^{*}\right)\sum_{m',n'}\left(\widetilde{A}_{\mu\nu}^{mn}(\widetilde{A}_{\mu\nu}^{m'n'})^{*}+\widetilde{B}_{\mu\nu}^{mn}(\widetilde{B}_{\mu\nu}^{m'n'})^{*}\right)\right. \\
& \left.+\left({}^{\ell}A E_{mn}\,{}^{\ell'}A H_{\mu\nu}^{*}+{}^{\ell}A H_{mn}\,{}^{\ell'}A E_{\mu\nu}^{*}\right)\sum_{m',n'}\left(\widetilde{A}_{\mu\nu}^{mn}(\widetilde{B}_{\mu\nu}^{m'n'})^{*}+\widetilde{B}_{\mu\nu}^{mn}(\widetilde{A}_{\mu\nu}^{m'n'})^{*}\right)\right].
\end{aligned}
\tag{57}
$$

It is to be noted that ${}^{\ell\ell'}\sigma_s = {}^{\ell'\ell}\sigma_s{}^{*}$ and thus

$$
{}^{\ell\ell'}\sigma_s + {}^{\ell'\ell}\sigma_s = 2Re({}^{\ell\ell'}\sigma_s). \tag{58}
$$

This allows the total scattering cross section to be expressed as

$$
\sigma_s = \sum_{\ell}{}^{\ell\ell}\sigma_s + 2Re\sum_{\ell}{}^{1\ell}\sigma_s + 2Re\sum_{\ell>1}\sum_{\ell'>\ell}{}^{\ell\ell'}\sigma_s, \tag{59}
$$

demonstrating that, as with the case of a single sphere, σ_s is an inherently real quantity—the real part of Eq. (51) need not be taken because the integral itself is real-valued.

The terms in Eq. (57) can be rearranged to give

$$\sigma_s = \frac{4\pi}{k^2} \sum_{m,n} \frac{n(n+1)(n+m)!}{(2n+1)(n-m)!} \left(|\mathcal{A}_{mn}|^2 + |\mathcal{B}_{mn}|^2 \right) \tag{60}$$

where

$$\begin{aligned} \mathcal{A}_{mn} &= \sum_{\ell} \sum_{\mu,\nu} \left({}^{\ell}AE_{\mu\nu}\, \widetilde{A}^{\mu\nu}_{mn} + {}^{\ell}AH_{\mu\nu}\, \widetilde{B}^{\mu\nu}_{mn} \right) \\ \mathcal{B}_{mn} &= \sum_{\ell} \sum_{\mu,\nu} \left({}^{\ell}AE_{\mu\nu}\, \widetilde{B}^{\mu\nu}_{mn} + {}^{\ell}AH_{\mu\nu}\, \widetilde{A}^{\mu\nu}_{mn} \right). \end{aligned} \tag{61}$$

The structure of this equation is identical to that for single spheres, where the amplitude coefficients of the natural modes of the sphere have been replaced with amplitude coefficients that may be associated with the natural modes of the cluster. These latter modes depend, in turn, on the amplitudes of the normal modes of the monomers in the cluster and on the precise information on the geometry of the cluster that is contained in the translation coefficients.

II.3.C. Special cases

As noted in the previous subsection and in Section 4, some important features of the cross sections are made visible by choosing different ways in which to write them. Additionally, there are commonly encountered special cases and approximations to scattering by more complicated particles that require only simplified versions of Eqs. (57) and (60).

When coordinate translations are constrained to the z-axis we have

$${}^{\ell'}\mathbf{M}^{(3)}_{mn} = \sum_{\substack{\nu = \\ max(1,m)}}^{\infty} \left({}^{\ell}\mathbf{M}^{(3)}_{m\nu} \widetilde{A}^{mn}_{m\nu}(k\mathbf{d}_{\ell',\ell}) + {}^{\ell}\mathbf{N}^{(3)}_{m\nu} \widetilde{B}^{mn}_{m\nu}(k\mathbf{d}_{\ell',\ell}) \right) \tag{62}$$

$${}^{\ell'}\mathbf{N}^{(3)}_{mn} = \sum_{\substack{\nu = \\ max(1,m)}}^{\infty} \left({}^{\ell}\mathbf{N}^{(3)}_{m\nu} \widetilde{A}^{mn}_{m\nu}(k\mathbf{d}_{\ell',\ell}) + {}^{\ell}\mathbf{M}^{(3)}_{m\nu} \widetilde{B}^{mn}_{m\nu}(k\mathbf{d}_{\ell',\ell}) \right). \tag{63}$$

As defined above, $kd_{1,1} = 0$. As shown in the appendix,

$$\lim_{kd_{\ell,\ell'} \to 0} \widetilde{A}^{m,n}_{\mu,\nu} = \delta_{n,\nu}\delta_{m,\mu} \tag{64}$$

and

$$\lim_{kd_{\ell,\ell'} \to 0} \widetilde{B}^{m,n}_{\mu,nu} = 0, \tag{65}$$

with the result

$$
{}^{1\ell'}\sigma_s = \frac{4\pi}{k^2} Re \sum_{m,n} \frac{n(n+1)(n+m)!}{(2n+1)(n-m)!} \times
$$

$$
\sum_{n'} \Bigg[\Big({}^{1}AE_{mn}\, {}^{\ell'}AE^{*}_{mn'} + {}^{1}AH_{mn}\, {}^{\ell'}AH^{*}_{mn'} \Big) (\widetilde{A}^{mn'}_{mn})^{*} + \tag{66}
$$

$$
\Big({}^{1}AE_{mn}\, {}^{\ell'}AH^{*}_{mn'} + {}^{1}AH_{mn}\, {}^{\ell'}AE^{*}_{mn'} \Big) (\widetilde{B}^{mn'}_{mn})^{*} \Bigg].
$$

Obviously, when $\ell = \ell' = 1$,

$$
\widetilde{A}^{mn}_{\mu\nu} (\widetilde{A}^{m'n'}_{\mu\nu})^{*} = \delta_{m,\mu} \delta_{m,m'} \delta_{n,\nu} \delta_{n,n'} \tag{67}
$$

$$
\widetilde{B}^{mn}_{\mu\nu} (\widetilde{B}^{m'n'}_{\mu\nu})^{*} = \widetilde{A}^{mn}_{\mu\nu} (\widetilde{B}^{m'n'}_{\mu\nu})^{*} + \widetilde{B}^{mn}_{\mu\nu} (\widetilde{A}^{m'n'}_{\mu\nu})^{*} = 0. \tag{68}
$$

Thus

$$
{}^{11}\sigma_s = \frac{4\pi}{k^2} \sum_{m,n} \frac{n(n+1)(n+m)!}{(2n+1)(n-m)!} \left(\left| {}^{1}AE_{m,n} \right|^2 + \left| {}^{1}AH_{m,n} \right|^2 \right). \tag{69}
$$

When $\ell \neq 1$, the phase of the scattered fields at points on the surface of integration will contain a phase shift that is dependent on the angle into which they are scattered. When a sphere of sufficiently large radius is considered, this phase factor can be expressed as

$$
\exp(-\imath k d_{1,\ell} \cos \psi_{1,\ell}), \tag{70}
$$

where

$$
\cos \psi_{1,\ell} = \sin \theta_{1,\ell} \sin \theta \cos(\phi_{1,\ell} - \phi) + \cos \theta_{1,\ell} \cos \theta \,. \tag{71}
$$

When $\ell, \ell' \neq 1$ in the integral of the Poynting flux, this leads to an even more complicated integrand. On the other hand, if $\ell = \ell'$ then the relative phase of the scattered electric field of a particle is exactly canceled by the complex conjugate of the relative phase of its scattered magnetic field. Thus

$$
{}^{\ell\ell}\sigma_s = \frac{4\pi}{k^2} \sum_{m,n} \frac{n(n+1)(n+m)!}{(2n+1)(n-m)!} \left(\left| {}^{\ell}AE_{m,n} \right|^2 + \left| {}^{\ell}AH_{m,n} \right|^2 \right), \tag{72}
$$

which it must if the solution obtained from Lorenz-Mie theory is to be recovered in cases where dependent scattering can be ignored. It then follows from Eq. (57) that

$$
\sum_{m',n'} \left(\widetilde{A}^{mn}_{\mu\nu}(k\mathbf{d}_{\ell,1}) \left(\widetilde{A}^{m'n'}_{\mu\nu}(k\mathbf{d}_{\ell,1}) \right)^{*} + \widetilde{B}^{mn}_{\mu\nu}(k\mathbf{d}_{\ell,1}) \left(\widetilde{B}^{m'n'}_{\mu\nu}(k\mathbf{d}_{\ell,1}) \right)^{*} \right) = \delta_{m,\mu} \delta_{n,\nu} \tag{73}
$$

and that

$$\sum_{m',n'}\left(\widetilde{A}_{\mu\nu}^{mn}(k\mathbf{d}_{\ell,1})\big(\widetilde{B}_{\mu\nu}^{m'n'}(k\mathbf{d}_{\ell,1})\big)^{*}+\widetilde{B}_{\mu\nu}^{mn}(k\mathbf{d}_{\ell,1})\big(\widetilde{A}_{\mu\nu}^{m'n'}(k\mathbf{d}_{\ell,1})\big)^{*}\right)=0. \tag{74}$$

Applying the same argument to Eq. (60) gives

$$\sum_{m,n}\frac{n(n+1)(n+m)!}{(2n+1)(n-m)!}\left(\widetilde{A}_{\mu\nu}^{mn}(k\mathbf{d}_{\ell,1})\big(\widetilde{A}_{\mu\nu}^{m'n'}(k\mathbf{d}_{\ell,1})\big)^{*}+\widetilde{B}_{\mu\nu}^{mn}(k\mathbf{d}_{\ell,1})\big(\widetilde{B}_{\mu\nu}^{m'n'}(k\mathbf{d}_{\ell,1})\big)^{*}\right)$$
$$=\delta_{m,\mu}\delta_{n,\nu} \tag{75}$$

and

$$\sum_{m,n}\frac{n(n+1)(n+m)!}{(2n+1)(n-m)!}\left(\widetilde{A}_{\mu\nu}^{mn}(k\mathbf{d}_{\ell,1})\big(\widetilde{B}_{\mu\nu}^{m'n'}(k\mathbf{d}_{\ell,1})\big)^{*}+\widetilde{B}_{\mu\nu}^{mn}(k\mathbf{d}_{\ell,1})\big(\widetilde{A}_{\mu\nu}^{m'n'}(k\mathbf{d}_{\ell,1})\big)^{*}\right)=0. \tag{76}$$

These relations provide valuable tests for convergence of the series expression of the scattering cross section of a cluster.

II.4. Discussion

As a means of checking Eqs. (59) and (60), Eq (53) was evaluated by Simpson's rule for cases involving pairs of spheres, linear chains of five spheres, and tightly packed clumps of five spheres. Complete agreement with the numerical integration was found in all cases. Such comparisons are rather limited, however, since the time required to perform the numerical integrations rises dramatically with modest increases in the size of the largest monomer. For this reason, comparisons were limited to size parameters of ≈ 11 or less for pairs of spheres. Available machine memory limited application of the theory for sphere clusters to $\ell_{\mathcal{D}} \approx 3$ for the cases involving five spheres. Nonetheless, the excellent agreement that was obtained in the comparisons that could be made is believed to be sufficient verification of the theory presented here.

Other work has been conducted on the scattering cross sections of sphere clusters, most notably, that of Borghese et al.[2] and of Mackowski,[3] and a discussion of it is warranted here. Borghese et al. have developed, independently, a theory for em scattering by clusters of spheres and have provided an expression for σ_s that is similar to Eq. (60). Agreement with their formula is easily obtained for the cases they considered, but they only tabulated values of σ_s for $0.001 \leq \ell_{\mathcal{D}} \leq 0.1$. Although Borghese et al. needed to retain terms through $n = 3$ in their expansions in order to get convergence of the series to four significant figures, such was not the case here. Their spheres are within the Rayleigh limit and dipolar contributions were always sufficient in the use of both Eqs. (59) and (60). Borghese et al. also noted that an increasing number of terms had to be retained in their series as the separation of the spheres was increased. Once again, such a complication was not encountered in the course of the comparisons made in the present study.

Borghese et al. found that their values of σ_s failed to converge to the sum of the cross sections of independent spheres for their smaller particles when $kd_{1,2} = 200ka$ and attributed this to interactions among higher order multipoles. This seems not to be credible, however, since in such cases $kd_{1,2} < 1$. Under such conditions the particles are not significantly out of phase in there response to the incident radiation and hence behave approximately as a single Rayleigh scatterer with twice the volume of a single sphere. This leads to a scattering efficiency that is four times that of the isolated spheres and this is what has been observed. The scattering cross section of a pair of identical, noninteracting Rayleigh particles is readily distilled from Eq. (59) by retaining only the contributions of the electric dipoles: Here

$$\sigma_s = {}^{11}\sigma_s + {}^{22}\sigma_s + 2Re\left({}^{12}\sigma_s\right) = 2\left[{}^{11}\sigma_s + Re\left({}^{12}\sigma_s\right)\right]. \tag{77}$$

When $\gamma = \pi/2$, Eq. (59) for ${}^{12}\sigma_s$ reduces to

$$\begin{aligned} Re\left({}^{12}\sigma_s\right) &= \frac{9\pi|{}^1a_1|^2}{k^2}\cos\left(kd\cos\alpha\right)\left[2a(1,1,-1,1,0)j_0\left(kd\right) + a(1,1,-1,1,2)j_2\left(kd\right)\right] \\ &= \frac{-9\pi|{}^1a_1|^2}{k^2}\frac{\cos\left(kd\cos\alpha\right)}{kd}\left[\left(\frac{1}{kd^2} - 1\right)\sin kd - \frac{\cos kd}{kd}\right], \end{aligned} \tag{78}$$

where $kd = kd_{1,2}$ and an expression for the coefficients $a(m,n,\mu,\nu,p)$ is given in the Appendix. The ratio of the scattering efficiency of the pair to those of the individuals can now be written as

$$\frac{Q_s}{({}^1Q + {}^2Q)} = 1 - \frac{3}{2}\frac{\cos\left(kd\cos\alpha\right)}{kd}\left[\left(\frac{1}{kd^2} - 1\right)\sin kd - \frac{\cos kd}{kd}\right]. \tag{79}$$

For sufficiently small kd this ratio is 2, as expected. Any variation from Eq. (79) is a measure of the strength of electrodynamic coupling between the dipoles.

The above discussion of the work of Borghese et al. should not be interpreted as an indictment of the validity their theory: on the contrary, in a later paper[14] they compared the extinction and phase shift efficiencies of pairs spheres of more appreciable size ($\wp \approx 3$) to experimental data. The agreement was good and their values have been reproduced with the use of Eqs. (26) and (38). It is also worth taking this opportunity to correct an oversight made by Fuller[1] wherein the latter paper of Borghese et al. was not included in a list of the few theoretical treatments of the cluster problem that included some type of experimental verification.

Mackowski[3] derives expressions for the cross sections of multiple sphere configurations, as well. As in the work of Borghese et al., his expression for σ_s is obtained by transforming the scattering coefficients of the different spheres into a representation about a principal origin (this transformation is the same as that given in Eqs. (61) above) and evaluating integrals similar to those in Eqs. (33) and (34). The result is an expression that is nearly identical to Eq. (60).

The more prominent accomplishment of Mackowski's research on the multiple sphere problem, however, has been the development of a set of recursion relations for the translation

coefficients that obviates the need for the Gaunt coefficients defined in the Appendix. The reduction in time and, more importantly, computer memory required for sphere aggregate calculations makes this one of the most significant breakthroughs in the problem in thirty years and will undoubtedly lead to investigations on aggregates of more and larger monomers than would have otherwise been possible.

In the implementation of Eq. (60) and, most likely, of its counterparts given in the works of Borghese et al. and Mackowski, the convergence of the series depends on the maximum value of $kd_{\ell,\ell'}$. This requires a larger set of scattering coefficients and hence the solution of a larger system of equations. These increases are rapid and make such solutions more cumbersome for large separations between spheres ℓ and ℓ'. Fortunately, it was found in the course of this research that the increase is not due to couplings between increasingly higher multipoles, but simply to an increasing number of terms needed in the addition theorem to accurately transform multipole coefficients from one set of coordinates to another. Thus, just as larger spheres require more terms in the series expansion of the incident fields to ensure that the boundary conditions are matched, so must the number of translation coefficients be increased for larger separations to ensure that the fields of the ℓth sphere are accurately transformed to the basis functions centered about the ℓ'th sphere. This requires only the calculation of additional translation coefficients—a task which is much easier than solving larger sets of equations and made even more so by the work of Mackowski—and computing the innermost summations in Eq. (57). The number of translation coefficients required for a prescribed accuracy can be found from the criteria laid out by Eqs. (73)-(76).

Chapter III. Scattering and Absorption Cross Sections of Compounded Spheres—Calculations.

III.1. Calculations for scavenging by haze and cloud elements

Results are presented in this section that illustrate the effects that the dispersion of carbon grains onto droplet surfaces may have on the mass absorption efficieny of atmospheric carbon. The scattering geometry for the surface dispersion calculations is shown in the insets of Figs. 3–10. At present, it is assumed that the concentration of the soot component of the aerosol or cloud is low enough so that only single grains of carbon need be considered. It is further assumed that the grains are of a spherical morphology. Soot concentrations that would involve two or more grains per aerosol particle will be the subject of future research.

It is popular (and, at times, useful) to define the efficiency factors for extinction, scattering and absorption to be, in order,

$$Q_e = \frac{\sigma_e}{G}, \quad Q_s = \frac{\sigma_s}{G}, \quad \text{and} \quad Q_a = \frac{\sigma_a}{G}, \tag{80}$$

where G is the geometric shadow of the particle and σ denotes the respective cross sections. In view of the complex morphologies of sphere aggregates, however, a better choice for efficiency factors is the gram-specific cross section, A, the units of which are m^2/g:

$$A = \frac{\sigma}{m} = \frac{\sigma}{(\text{specific gravity})(\text{ particle volume})}. \tag{81}$$

Figs. 3–10 catalogue the calculated specific absorption cross sections of selected sizes of carbon grains attached to nonabsorbing sulfate particles with radii of 0.5 and 1.0μm or to water droplets with radii of 3.0 and 5.0μm. The variation in specific absorption with the orientation of the particle is displayed for mutually orthogonal polarizations of the incident beam. It is noted that for a single sphere of radius $a << \lambda$,

$$\begin{aligned} A_a(\lambda) &= \frac{3k}{\rho} Im\left(\frac{N^2-1}{N^2+2}\right) \\ &= \frac{9k\,|N|^2 \sin\left(2\tan^{-1}\left[Im(N)/Re(N)\right]\right)}{\rho\left[|N|^4 + 4(1 + Re^2\{N\} - Im^2\{N\})\right]} \end{aligned} \tag{82}$$

At $\lambda = 5.5 \times 10^{-7}$ m this gives a specific absorption cross section of $\approx 3.654\ m^2/g$ for a sphere of carbon having a refractive index $N = 1.80 + 0.5i$ and specific gravity $\rho = 1.8 g/cm^3$. This limit is very near the specific absorption of the isolated 0.01μm carbon grain depicted by the narrower line in, for example, Fig. 3. The above wavelength and parameters for carbon are assumed throughout the rest of this work.

The basic features of the dependence of A_a on orientation can be understood from geometric optics: An optically large sphere with a refractive index of ≈ 1.5 will focus light into a

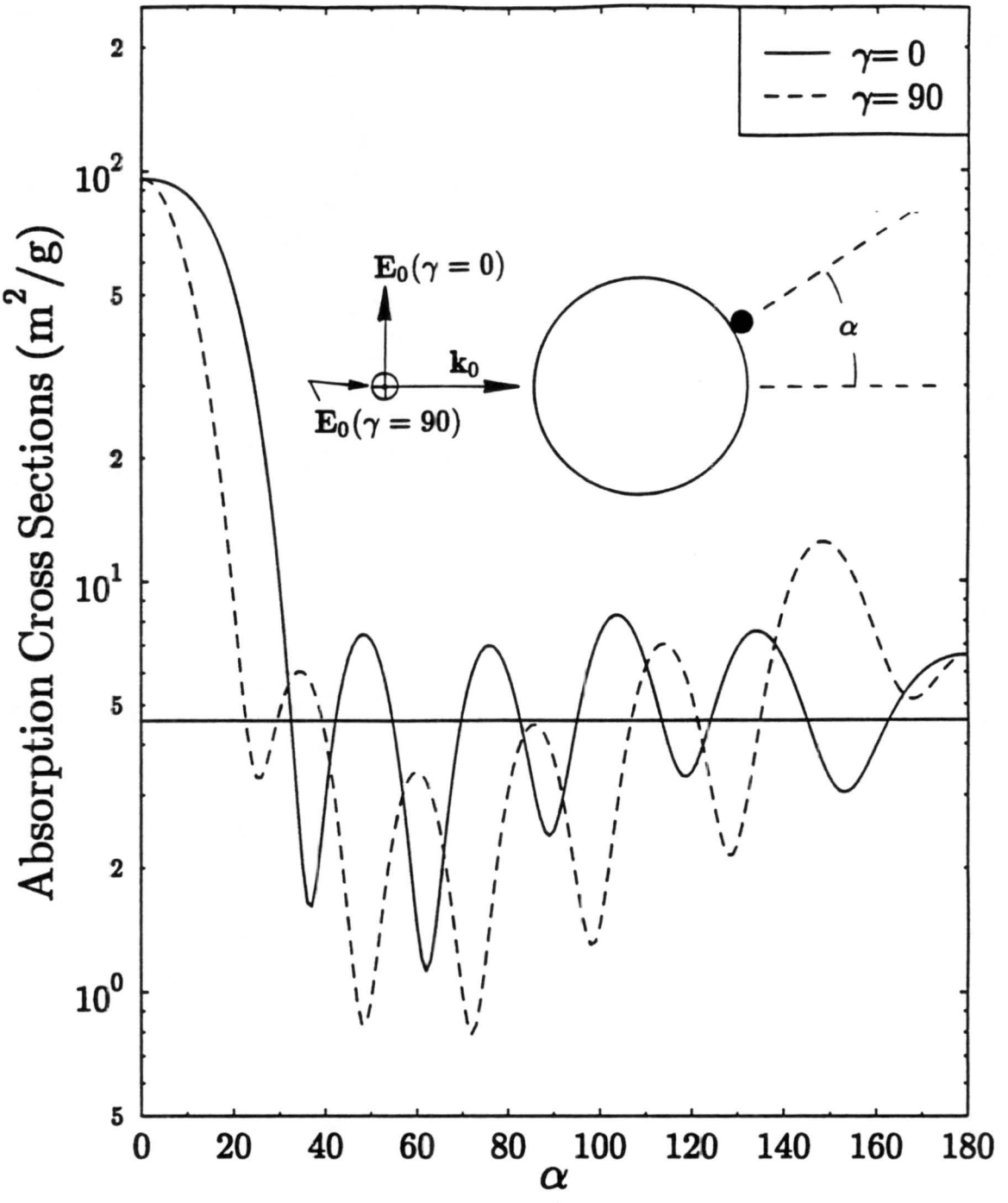
γ= 0
γ= 90
Absorption Cross Sections (m²/g)
α
E₀(γ = 0)
k₀
E₀(γ = 90)
α
2
10²
5
2
10¹
5
2
10⁰
5
0
20
40
60
80
100
120
140
160
180
α

region near its surface. If the refractive index is ≈ 1.33 then light will be focused into a volume slightly less than half a radius from the sphere surface. The refractive effects of the sphere will prevent most of the incident radiation from reaching regions other than the focal volume on the shadow side of the surface. Reflections from the shadow surface of the sphere will produce a secondary focal volume narrowly centered about the illuminated side of the droplet. Such features of a spherical lense are manifested in the behavior of the absorption cross sections of the carbon grains as a finction of particle orientation in each of Figs. 3–10. The larger the optical size of the host particle, the more accurate the geometric optics picture. When carbon grains are found within the focal volumes of the larger particles, their absorption cross sections can be enhanced by well over an order of magnitude.

Carbon spheres with radii of 0.01, 0.05, and 0.10μm are considered. In each of Figs. 3–10, $A_a(\alpha)$ is displayed for both polarizations. The intermediate-sized grain is considered first and, in the figure that immediately follows, both the largest and smallest grains are studied. For comparison, the specific absorption cross sections of the corresponding carbon particles in isolation are also provided.

III.1.A. Carbon on a concentrated sulfate particle

The refractive index of the host particles considered in Figs. 3–6 is taken to be $1.52+0.0i$; appropriate for sulfuric acid droplets or ammonium sulfate particles at low relative humidities. The absorption cross sections of carbon spheres attached to other particles not only depend on the orientation of the system relative to the incident beam, but, as is seen in the figures, on the polarization of the beam, as well. This is primarily because the stucture of the electric fields along a specified equator of the host have a strong polarization dependence. In fact, the smaller carbon grains act as probes of the source function, $\mathbf{E} \cdot \mathbf{E}^*$, at the surface. (The magnetic fields are not probed since the absorption arises only from the coupling of the local electric field to current densities which are themselves proportional to that field.) In this regard, attention is called to the increased detail seen in $A_a(\alpha)$ for the 0.01μm carbon grain considered in Fig. 4 over that for the 0.05μm grain of Fig. 3. On the other hand, $A_a(\alpha)$ for a 0.10μm grain is considerably smoother. The larger the grain, the less sensitive its A_a to rapid variations in $\mathbf{E} \cdot \mathbf{E}^*$. This effect of an increasing grain size is reminiscent of the convolution of a noisy function with a Gaussian profile of increasing width.

For the polarization $\gamma = 0$, the incident electric vector has a component that lies along the line of centers of the two spheres, giving rise to a radial component of $\mathbf{E}$ at their surfaces. The electrodynamic coupling of the radial component of the field that arises when $\gamma = 0$ in addition to the coupling of the tangential component explains why $A_a(\alpha)$ tends to be larger than for the case $\gamma = 90°$.

The lensing effect is seen to be stronger for the larger sulfate host, as is the refractive shielding in the region $30° < \alpha < 90°$. This latter effect serves to hide the carbon from the incident radiation, thereby offsetting to some degree, the increased heating of the grain within the focal volume of the host. Once again, both of these effets are explained qualitatively by the geometric optics picture. Attention is called to the fact that in Fig. 6 $A_a(8°) > A_a(0°)$ for the smaller carbon grain. This is a consequence of prominences in the source function near the surface of the particle, just off the beam axis. Such prominences are commonly seen in source functions associated with morphology-dependent resonances.[1]

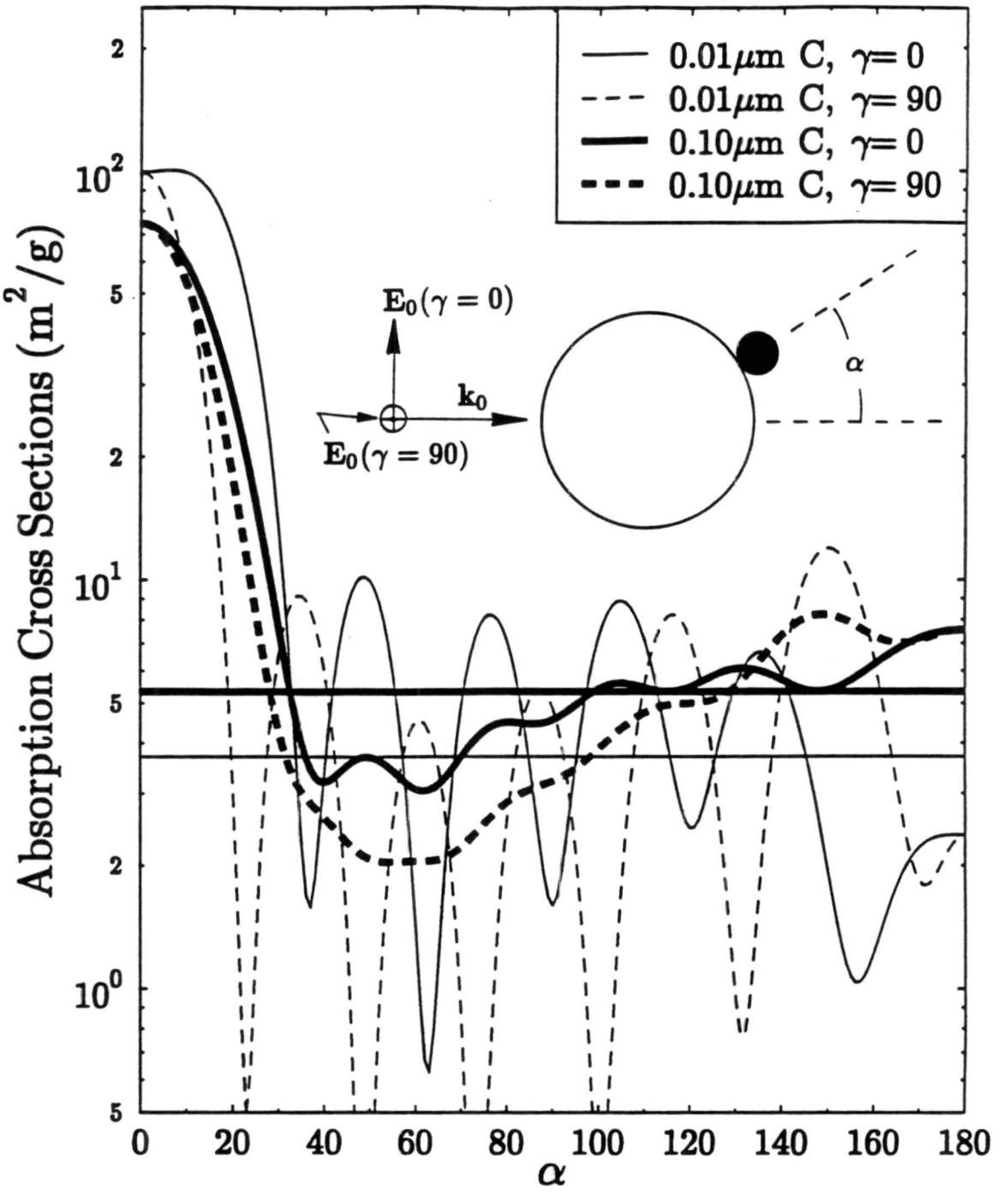
0.01μm C, γ= 0
0.01μm C, γ= 90
0.10μm C, γ= 0
0.10μm C, γ= 90
E0(γ = 0)
k0
E0(γ = 90)
α
Absorption Cross Sections (m2/g)
α
2
10^2
5
2
10^1
5
2
10^0
5
0
20
40
60
80
100
120
140
160
180

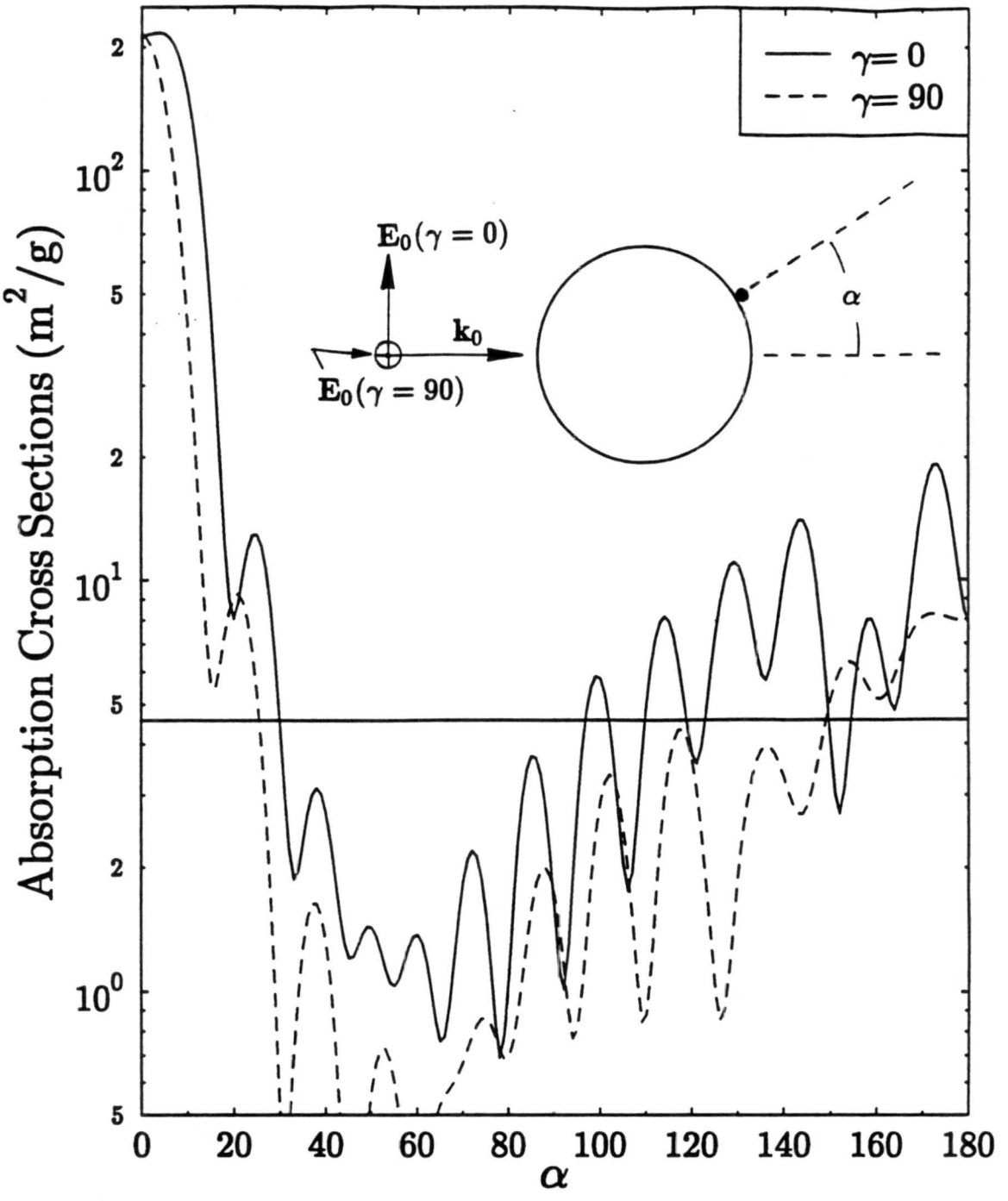
γ= 0
γ= 90
E0(γ = 0)
k0
E0(γ = 90)
α
Absorption Cross Sections (m2/g)
α
0
20
40
60
80
100
120
140
160
180
2
10^2
5
2
10^1
5
2
10^0
5

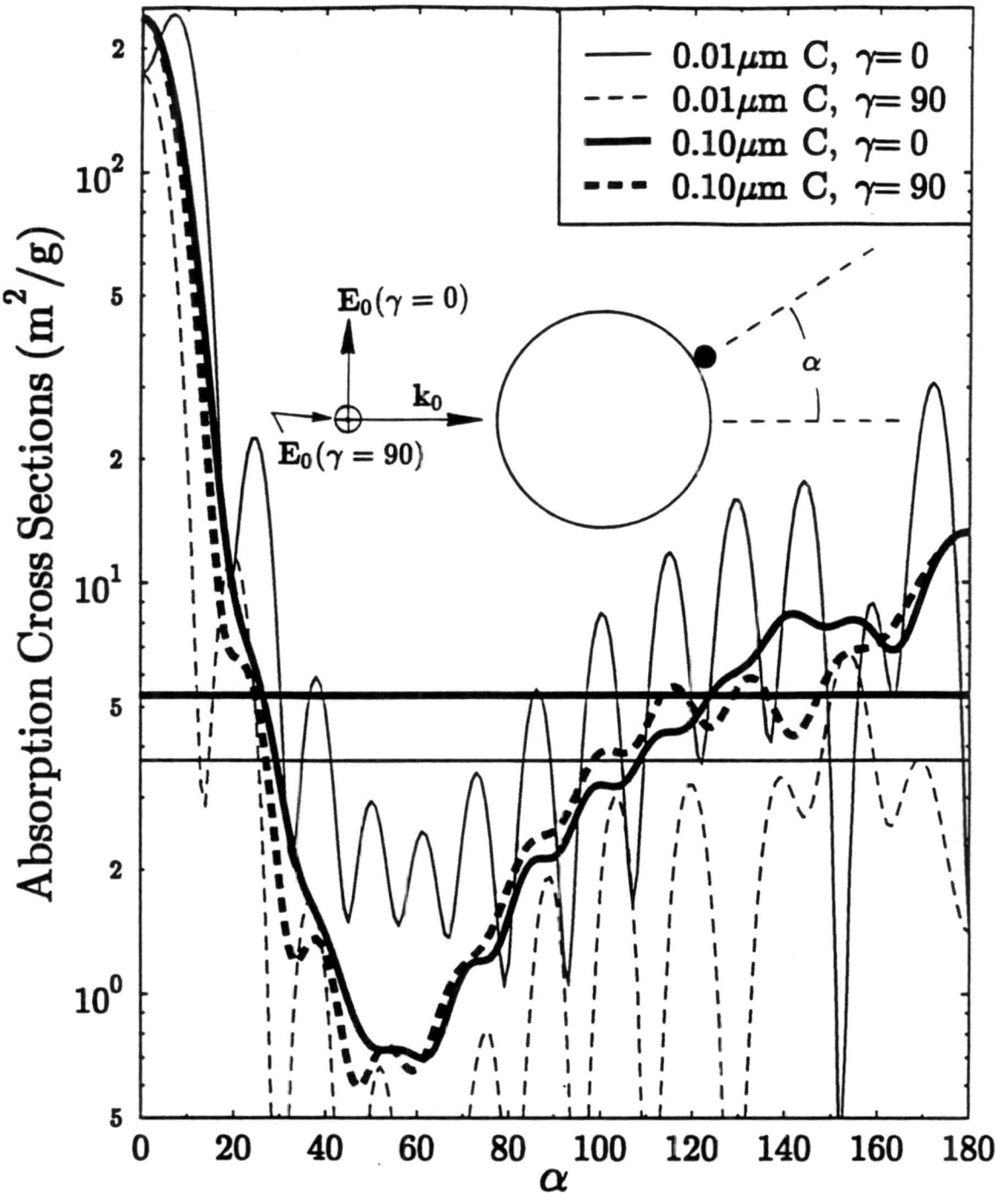
0.01μm C, γ= 0
0.01μm C, γ= 90
0.10μm C, γ= 0
0.10μm C, γ= 90
E0(γ = 0)
k0
E0(γ = 90)
α
Absorption Cross Sections (m2/g)
α
0
20
40
60
80
100
120
140
160
180
2
5
10^2
10^1
10^0

III.1.B. Carbon on a water droplet

The absorption cross sections of carbon particles attached to cloud droplets have also been investigated and some of the results are displayed in Figs. 7–10. There is a strong enhancement of A_a near $\alpha = 0$, as expected, and an off axis prominence is evidenced consistently for the polarization $\gamma = 0$. Attention is also called to a second peak in A_a near $\alpha = 17°$. This second peak locates the so-called critical ring.[15]

The lensing effect of the water droplets does not enhance the absorption cross sections to as great of a degree as it does in the case of the smaller sulfate particles, primarily because the sulfates have a higher refractive index and hence their focal volume is centered at or very near the surface. On the other hand, the intersection of the caustic with the surface of the water droplets near $\alpha = 17°$ produces an enhancement in A_a over a somewhat greater range in orientation. The caustic more sharply defines a boundary between regions with high values of $|E|^2$ and those where $|E|^2 \approx 0$ for the optically large water droplets and hence refractive shielding of carbon grains by cloud droplets is more pronounced than by haze elements.

III.2. Calculations for carbon agglomerates

Of considerable interest in the study of interstellar and interplanetary dust, extraterrestrial atmospheres (especially that of Titan), and combustion-generated soot aerosols are the optical properties of aggregates of carbonaceous monomers. Two general cases, ramiform and aciniform aggregates, are considered here. These cases are represented by, respectively, linear chains and tightly packed clusters of five spheres. Although this limited set of examples can hardly constitute an exhaustive survey of the optical properties of soot agglomerates, it subjects certain approximations that are fundamental assumptions in the application of fractal optics to this problem to comparisons with exact calculations.

The mass extinction and absorption cross sections for a linear chain of carbon spheres are shown as a function of orientation in Figs. 11–13. Similar results for a tightly packed hexahedral cluster are provided in Figs. 14–16. For comparison, the cross sections for isolated monomers and for equivalent-volume spheres are also shown.

The scattering geometry for the ramified aggregates is shown in the insets of Figs. 11 and 12. As seen in Fig. 11, extinction by the smallest monomers is due almost entirely to absorption. This is not unexpected since the mass scattering coefficient of small particles is proportional to their volume, whereas the mass absorption cross section is independent of their size, as seen in Eq. (3). For the same reasons, the extinction cross section of the isolated spheres (free carbon) is nearly identical to that of the equivalent volume sphere. Fig. 11 also provides a demonstration of how polaroid J-sheet generates polarized light. Extinction by the linear chain is about twice as great when the incident field is parallel to the chain than when it is perpendicular to it. Such dichroism is also clearly seen in Fig. 12 but the radii of the monomers are five times those in Fig. 11; scattering is no longer negligible and there is considerable separation betweeen the curves for extinction and absorption. In Fig. 12 the size parameter of the spherules is 1.142 and scattering now accounts for about half of the extinction. The polarization dependence of the cross sections is now reversed, with the case of endfire incidence now leading to the greatest extinction. It is also noted that in the transition from $ka = 0.5712$ to $ka = 1.142$ for the primary spheres in the chain, the extinction cross

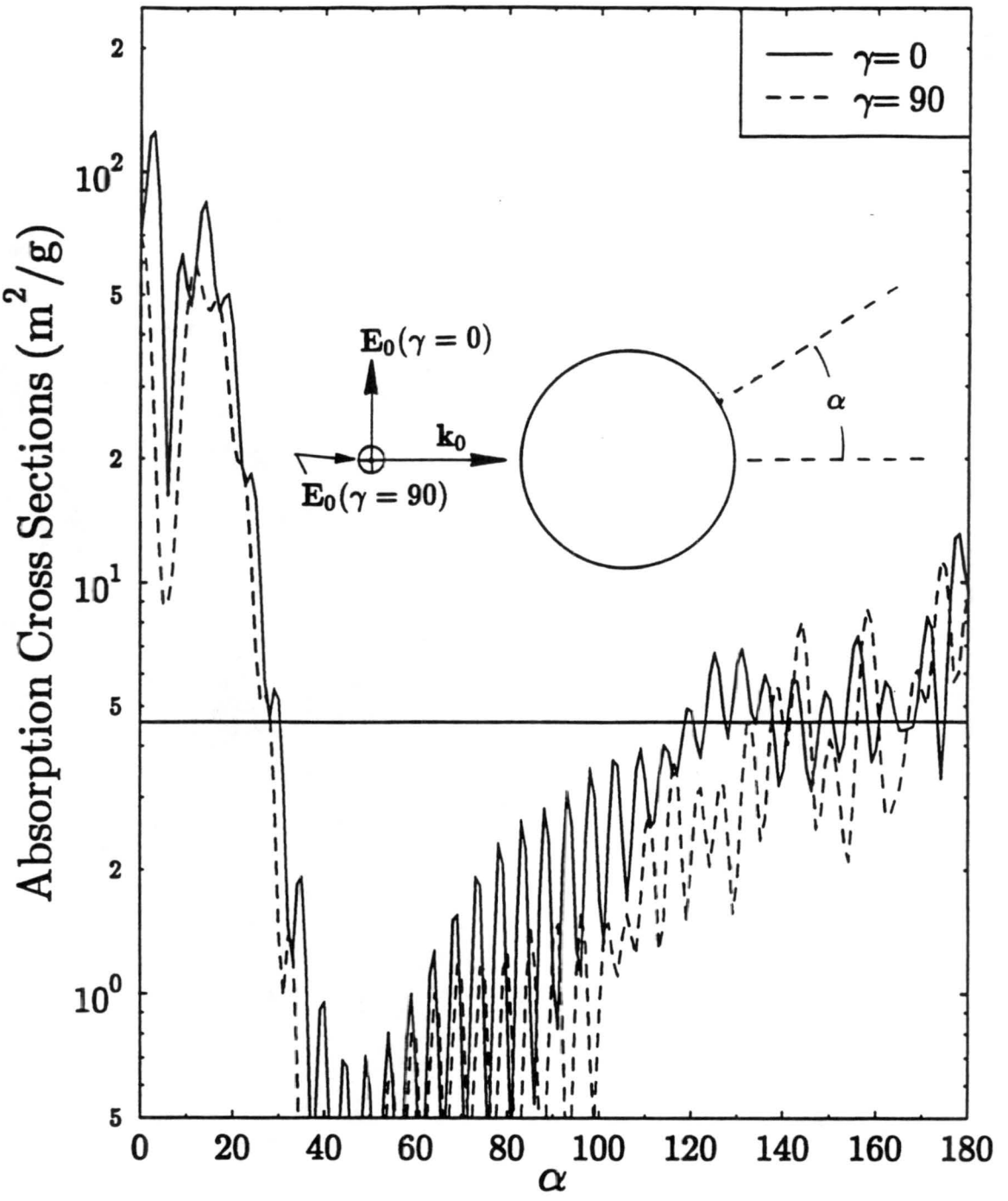
γ= 0
γ= 90
Absorption Cross Sections (m²/g)
E₀(γ = 0)
k₀
E₀(γ = 90)
α
α
2
10²
5
2
10¹
5
2
10⁰
5
0
20
40
60
80
100
120
140
160
180

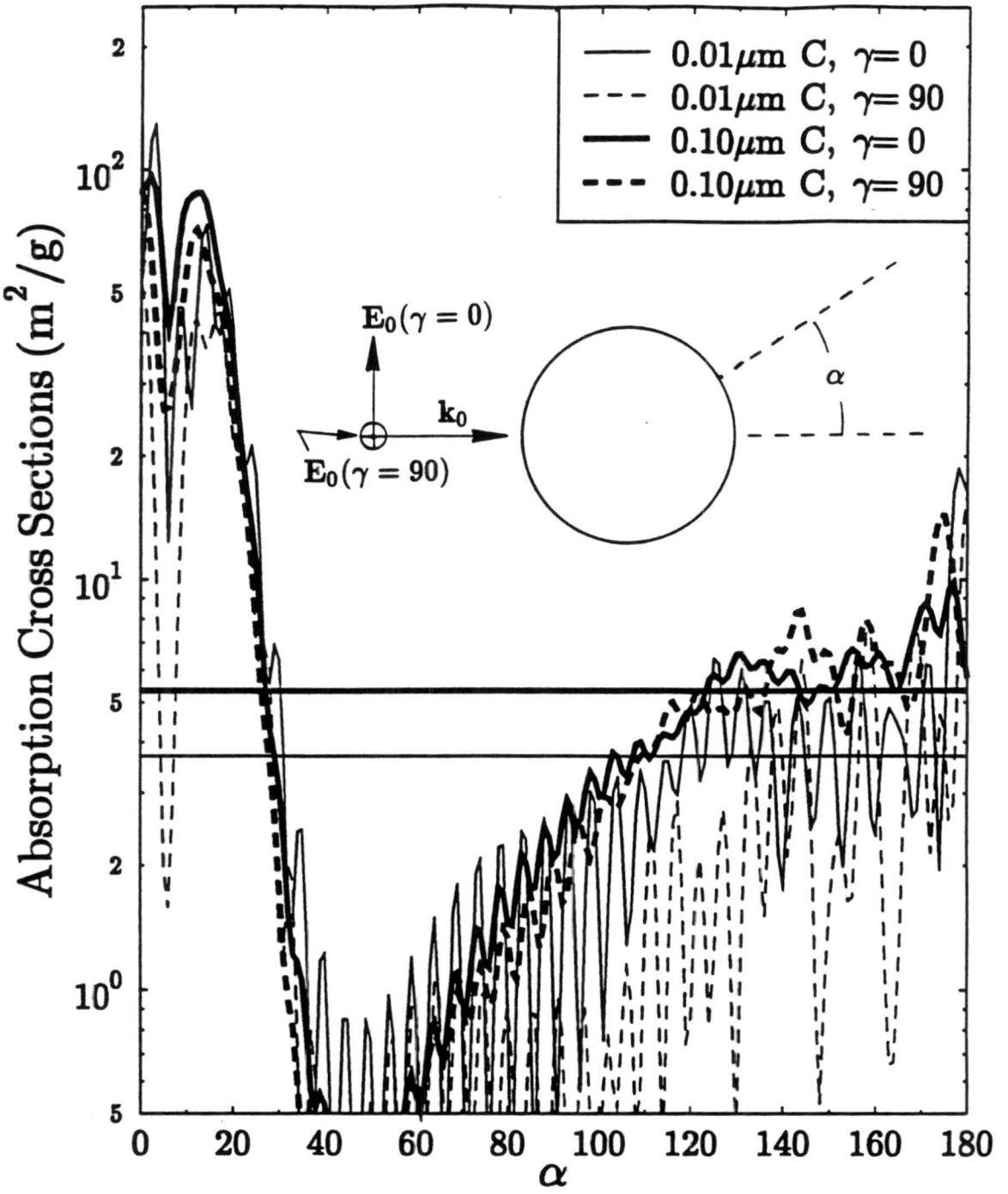
0.01μm C, γ= 0
0.01μm C, γ= 90
0.10μm C, γ= 0
0.10μm C, γ= 90
E0(γ = 0)
k0
E0(γ = 90)
α
Absorption Cross Sections (m2/g)
α
2
10^2
5
2
10^1
5
2
10^0
5
0
20
40
60
80
100
120
140
160
180

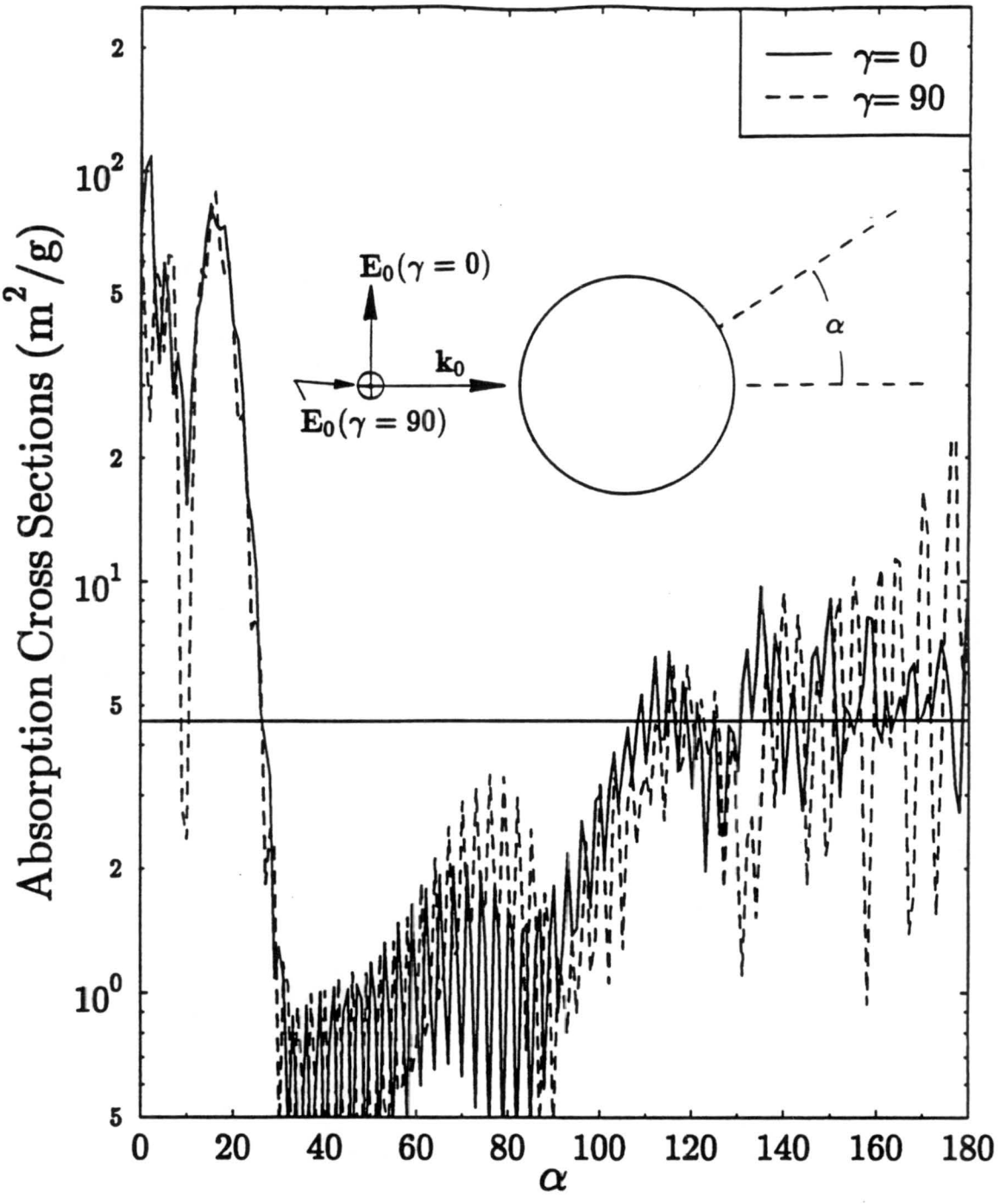
γ= 0
γ= 90
$\mathbf{E}_0(\gamma = 0)$
$\mathbf{k}_0$
$\mathbf{E}_0(\gamma = 90)$
α
Absorption Cross Sections (m^2/g)
α
2
10^2
5
2
10^1
5
2
10^0
5
0
20
40
60
80
100
120
140
160
180

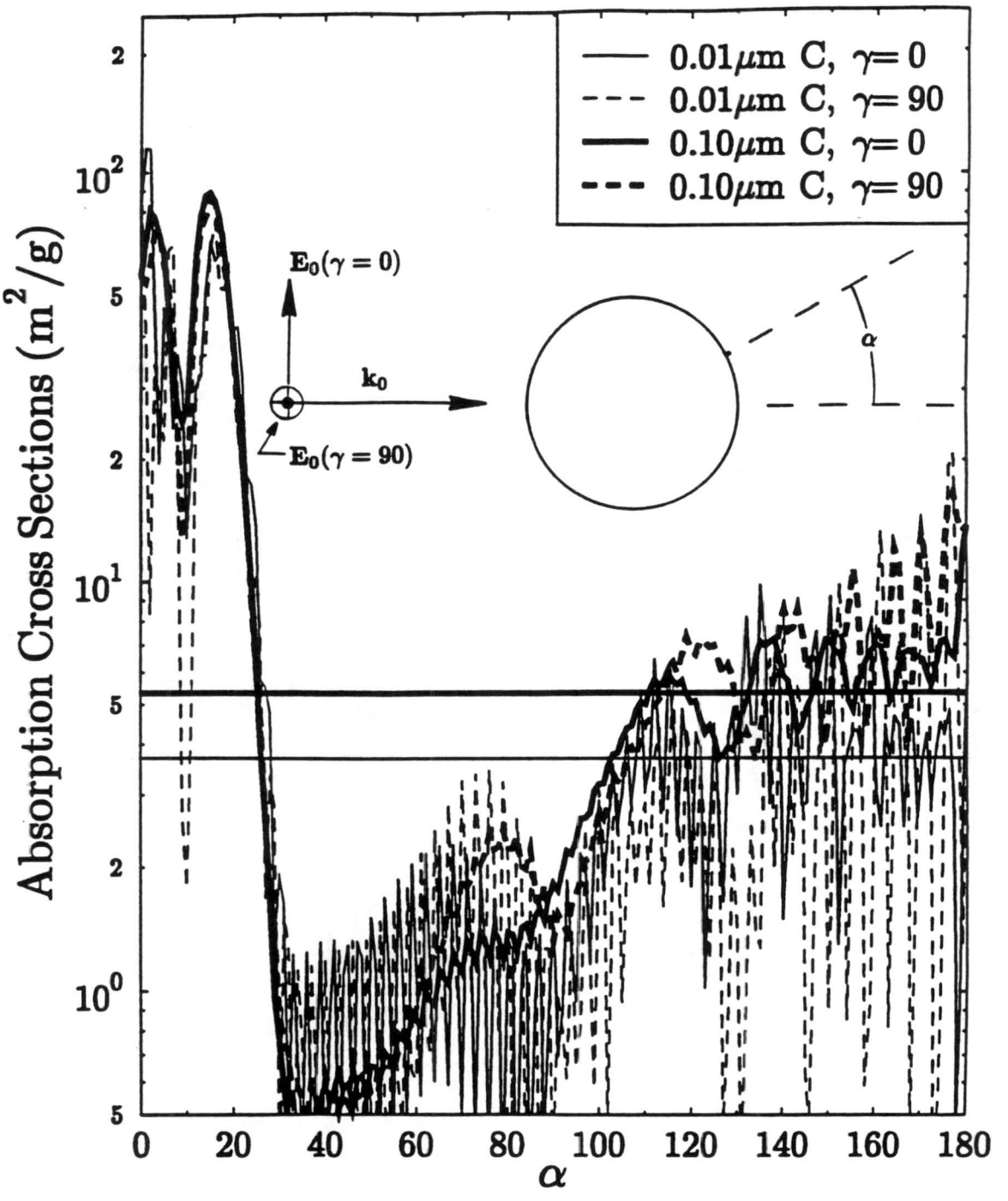
0.01μm C, γ= 0
0.01μm C, γ= 90
0.10μm C, γ= 0
0.10μm C, γ= 90
E0(γ = 0)
k0
E0(γ = 90)
α
Absorption Cross Sections (m2/g)
α
0
20
40
60
80
100
120
140
160
180

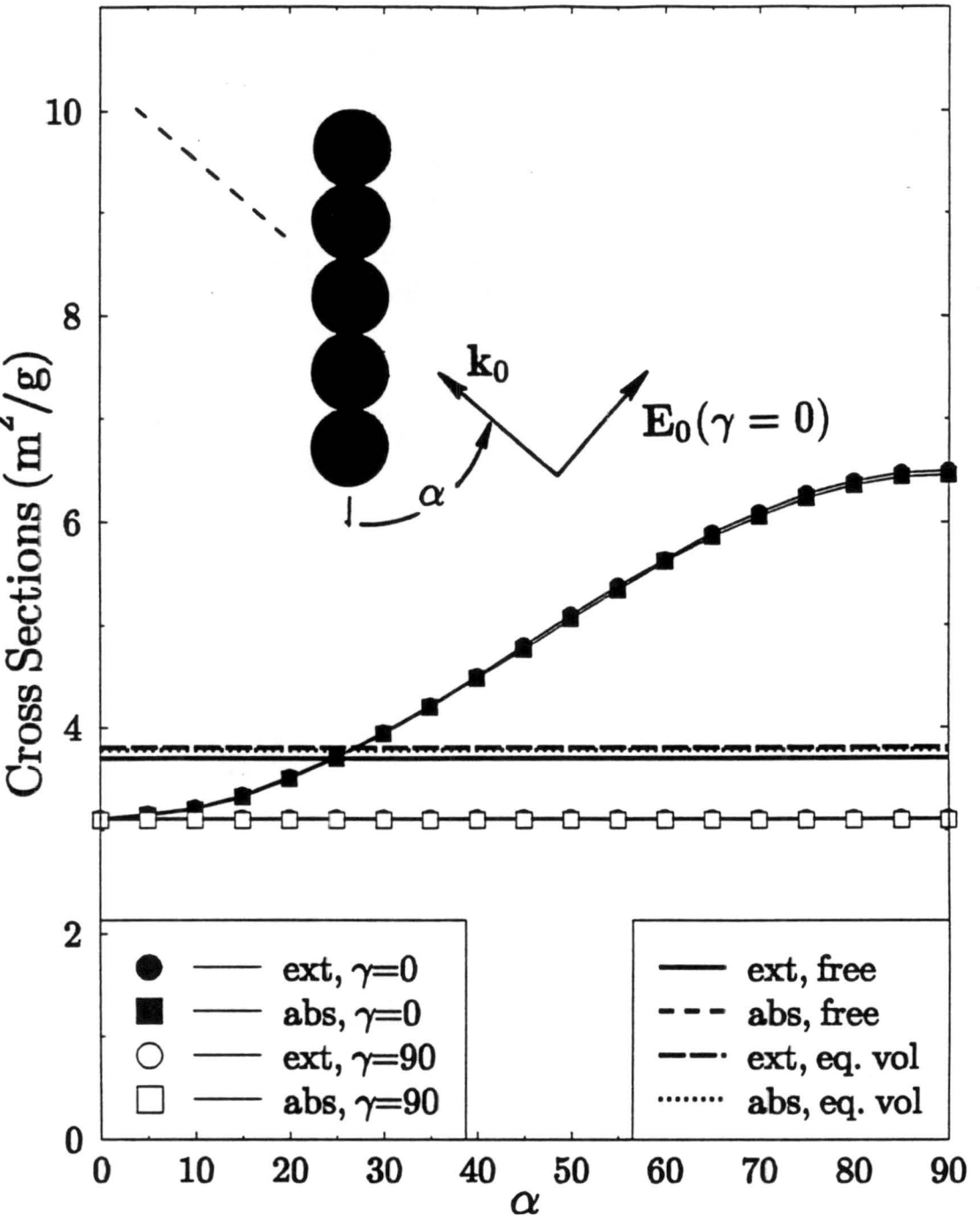
Cross Sections (m^2/g)
10
8
6
4
2
0
0
10
20
30
40
50
60
70
80
90
α
$\mathbf{k}_0$
$\mathbf{E}_0(\gamma = 0)$
α
ext, γ=0
abs, γ=0
ext, γ=90
abs, γ=90
ext, free
abs, free
ext, eq. vol
abs, eq. vol

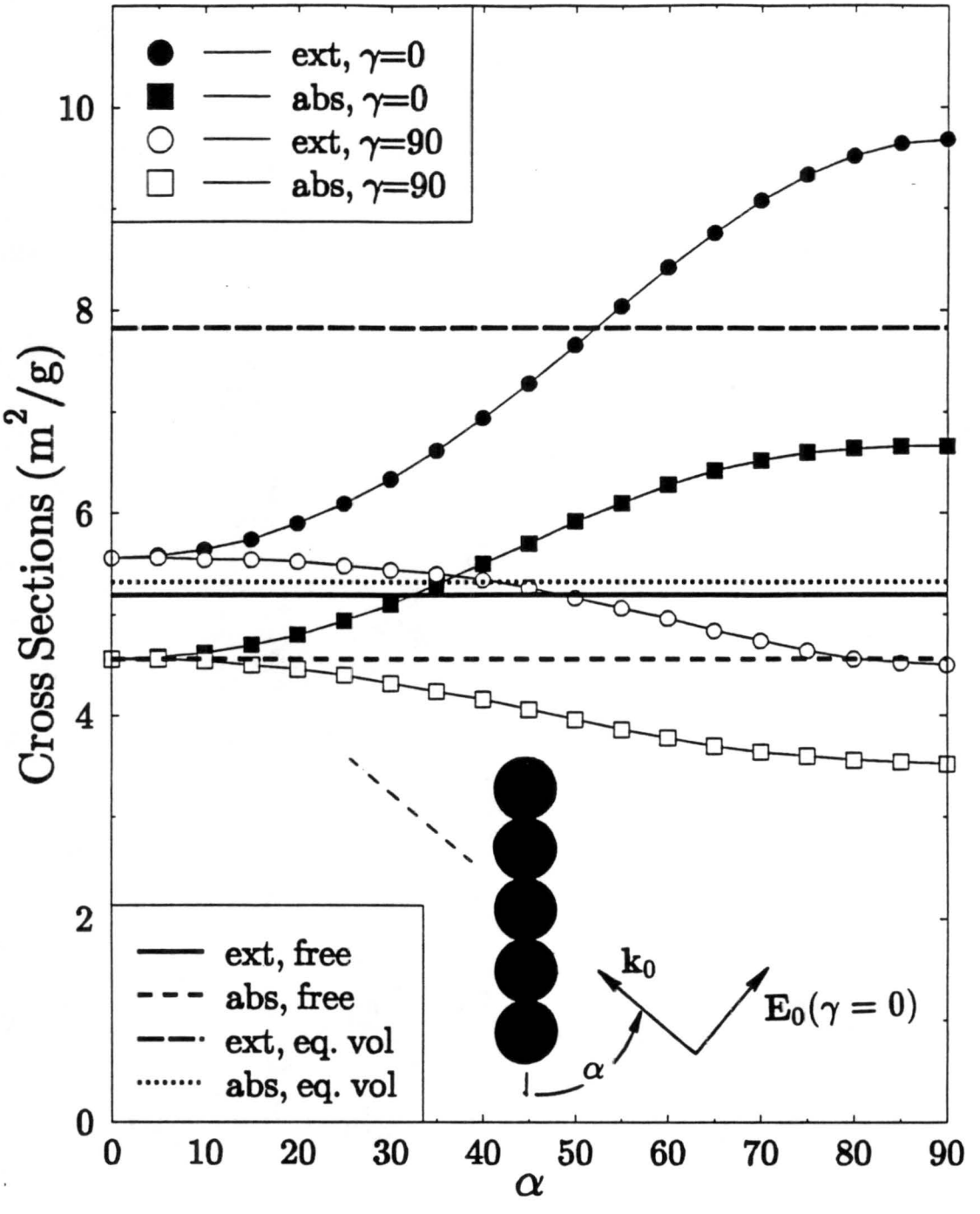
ext, γ=0
abs, γ=0
ext, γ=90
abs, γ=90
ext, free
abs, free
ext, eq. vol
abs, eq. vol
Cross Sections (m²/g)
α
k₀
E₀(γ = 0)
0
2
4
6
8
10
0
10
20
30
40
50
60
70
80
90

section of the equivalent volume sphere falls slightly while that of the free carbon increases by about 70%. The increase for the free carbon is accounted for by an increase in scattering and the decrease for the equivalent volume sphere is due to a decrease in absorption. This diminished absorption is in turn owed to strong attenuation near the surface of the particle which, at this size, is beginning to prevent radiation from interacting throughout the volume of the absorber.

To gauge the magnitude of the effect of electrodynamic coupling on the optical properties of the elongated particles under consideration, comparison should be made between the exact cross sections and those of the free carbon grains. It is noted that even though the chain with the smallest monomers displays in Fig. 11 an extinction (absorption) cross section with no orientational dependence when $\gamma = 90°$, this does not mean that the effects of mutual polarization are completely negligible: The extinction cross section of the chain for this polarization is about 20% lower than for the case of free carbon. (There is, of course neither a polarization nor orientation dependence for the cross sections of the noninteracting particles.) When $\gamma = 0°$ the optical properties of the chain become very sensitive to orientation, differing from those for $\gamma = 90°$ the most at $\alpha = 90°$. This is likely due to the dipolar nature of the small spherules. The radial components of the electric fields of the grains can be roughly proportional to r^{-3} near the surfaces, providing for a more efficient electrodynamic coupling between the particles as α approaches 90°. When γ and α are both 90°, the radial components of the electric dipolar fields vanish along the line of centers. These observations also apply to the results shown in Fig. 11 but, as noted earlier, scattering no longer makes an insignificant contribution to extinction. The anisotropy of the scattered field of these larger particles results in a stronger coupling between them when they are within each others geometric shadow than when they interact through side scattering at $\alpha = 90$, provided that $\gamma = 90°$. This accounts for the values of A_a being higher near 0° and then dropping off as α increases to 90°. If $\gamma = 0°$, the effect of the radial component of $\mathbf{E}$ still dominates the interaction as α increases from 0° to 90°. In Fig. 13 where the monomers are largest, the forward-scattered field provides for the greatest interaction, regardless of polarization.

For the aciniform (grape-like) clusters considered in Figs. 14–16, the agglomerates are elongated in the direction of $\mathbf{E}$ when $\gamma = 90°$, thus for the clusters made from the smallest ($ka = 0.1142$) spherules it is seen in Fig. 14 that this polarization produces extinction cross sections which are larger, by about 25%, than those of the free carbon. On the other hand, the extinction cross sections for $\gamma = 0°$ is almost identical to that of the noninteracting spheres. For the $ka = 0.5712$ monomers, the absorption cross section at $\gamma = 0°$ is still very nearly that of the free carbon (see Fig. 15), indicating that coupling is still weak, but the extinction has increased by about 40% due to the onsset of significant scattering by the monomers. Dependent scattering is still relatively strong at $\gamma = 90°$, producing an extinction cross section that is about 60% larger than that of free carbon. A similar increase in the extinction of the equivalent-volume sphere can also be seen. Fig. 16 shows the absorption and extinction cross sections for a cluster made up of primary spheres with $ka = 1.142$. For both polarizations, the absorption cross sections of the cluster are much closer to that of the equivalent-volume sphere than to that of the free carbon because the compact cluster serves to shield parts of its constituents from the incident light. The extinction values fall in between those of the free carbon and equivalent volume sphere. Due to their compact morphology, the

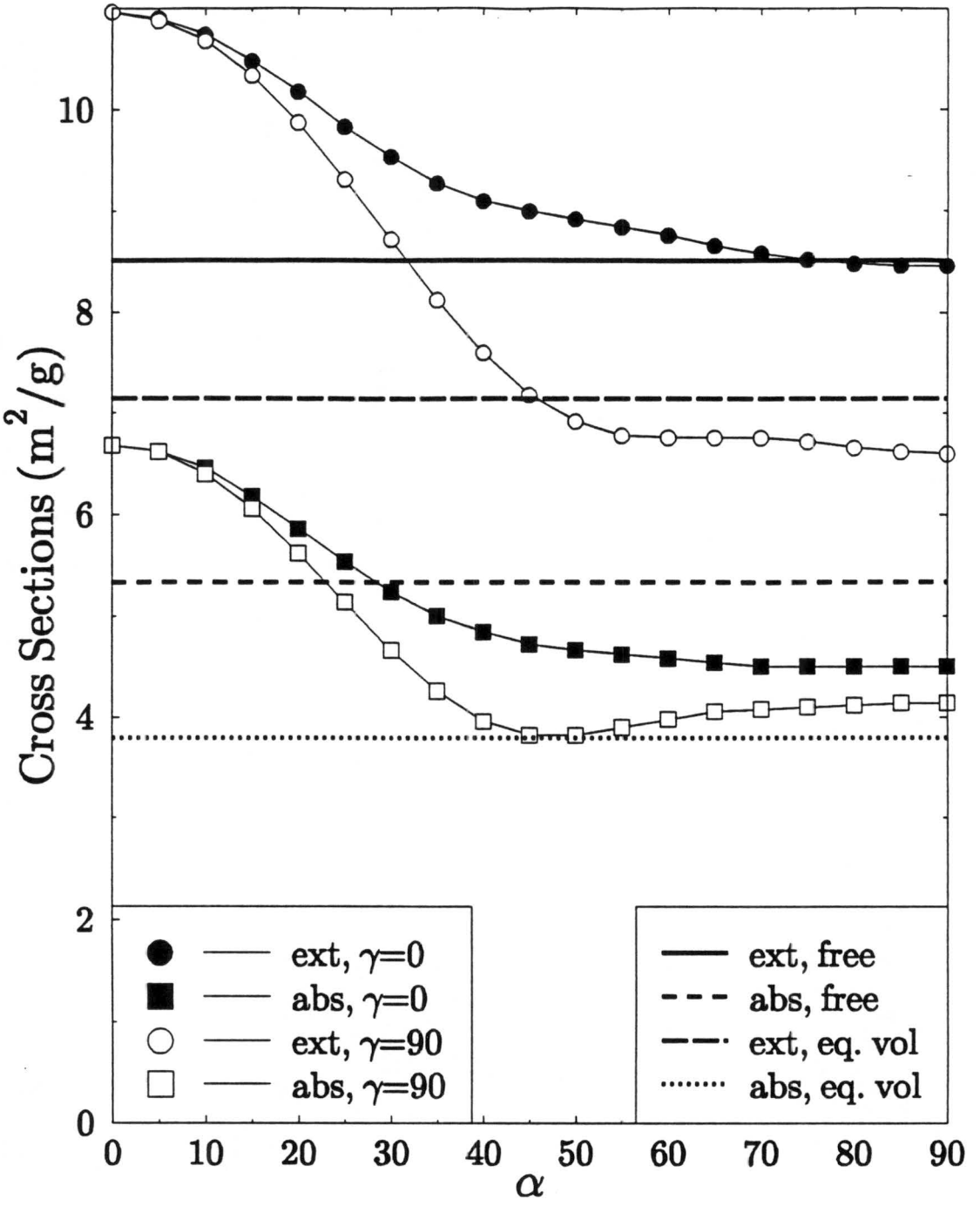
Cross Sections (m^2/g)
10
8
6
4
2
0
0
10
20
30
40
50
60
70
80
90
α
ext, γ=0
abs, γ=0
ext, γ=90
abs, γ=90
ext, free
abs, free
ext, eq. vol
abs, eq. vol

clusters display very little orientation dependence in there cross sections.

III.3. Ensemble-averaged cross sections

In order to better understand the effects that scavenging of soot by transparent droplets may have on the optical properties of haze and clouds, it is necessary to consider the orientation and polarization averages of the cross sections presented in Figs. 1–8. Cross sections for single carbon spheres are listed in Table I: The cross sections for spheres of the same size as the spherules that are scavenged or agglomerated are provided, as are the cross sections of single spheres having the same volume as five spherules. (This latter set of values will be used in further analyses of the extinction properties of the carbon agglomerates.) For a given polarization, the orientation-averaged A_a is taken to be

$$\langle A_a \rangle = \frac{1}{2} \int_0^\pi A_a(\alpha) \sin(\alpha)\, d\alpha. \tag{83}$$

If the particles are constrained to rotate in a plane that is, for example, perpendicular to the polarization direction given by $\gamma = 90°$ then the averages would take the form

$$\langle A \rangle = \frac{1}{\pi} \int_0^\pi A(\alpha)\, d\alpha. \tag{84}$$

Table II provides a summary of the averaged mass absorption cross sections for both incident polarizations. One sees that for $\gamma = 90°$, $\langle A_a \rangle$ increases as the size of the carbon grains is increased for all four classes of scavenging droplets. The same holds true for $\gamma = 0°$ when cloud droplets are involved, but $\langle A_a \rangle$ steadily decreases with increasing grain size when the grains are associated with the sulfate droplets.

As noted in the Introduction, an important consideration in the study of visibility and climate is the possible alteration of the single scatter albedo of carbon-containing aerosol and cloud volumes by dispersion of that carbon onto droplet surfaces. (Absorption by internally dispersed carbon grains is the subject of an upcoming publication.[16]) It is therefore useful to compare the mass absorption cross sections of externally mixed carbon to the those listed in Table II. Table III displays the ratios of $\langle A_a \rangle$ from Table II to the cross sections for the free carbon, say A_{fc}, is shown in Table I. The average of $\langle A_a \rangle / A_{fc}$ for the two polarizations is also shown. Relative to A_{fc}, $\langle A_a \rangle$ is seen to decrease with increasing grain size for most of the cases considered and never shows a significant increase. This is tendency is even more marked when the polarization-average is taken.

From Table III, it is also seen that the single scattering coalbedo associated with surface mixing can exceed that for externally mixed carbon by almost a factor of 2 when the carbon grains and haze elements both assume their smallest values. More importantly, perhaps, is that $\langle A_a \rangle$ typically lies below A_{fc} when cloud droplets are involved. There is here a clear tendency for the droplets to, on average, partially shield the carbon from the incident radiation: The strong enhancements of A_a near $\alpha = 0$ due to lensing effects of the host sphere are washed out by the $\sin\alpha$ term (i.e., by the low probability for realizing such an alignment) to a much greater degree than is the reduction in A_a that is due to refractive shielding. Carbon on the

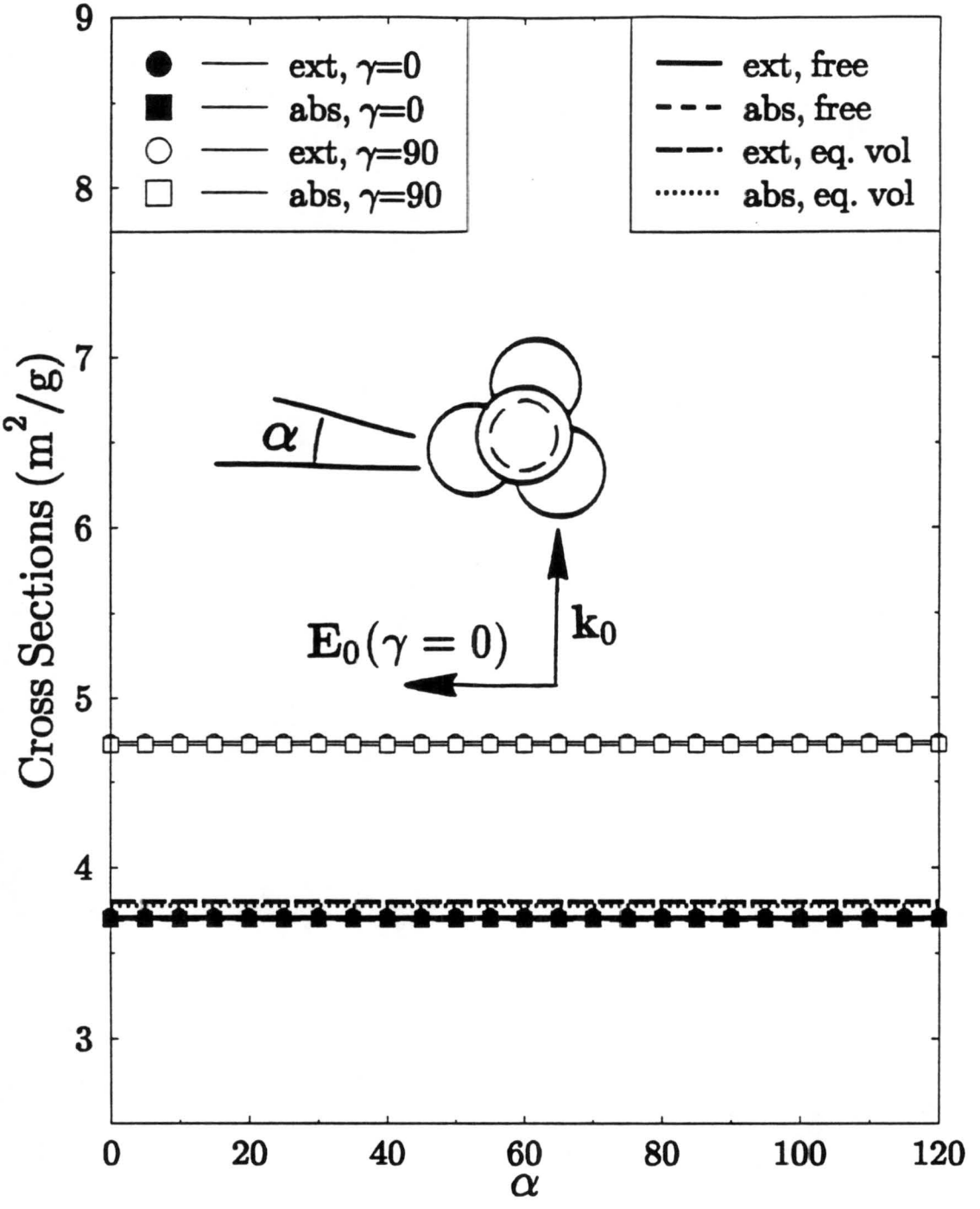
ext, γ=0
abs, γ=0
ext, γ=90
abs, γ=90
ext, free
abs, free
ext, eq. vol
abs, eq. vol
α
E0(γ = 0)
k0
Cross Sections (m²/g)
α
9
8
7
6
5
4
3
0
20
40
60
80
100
120

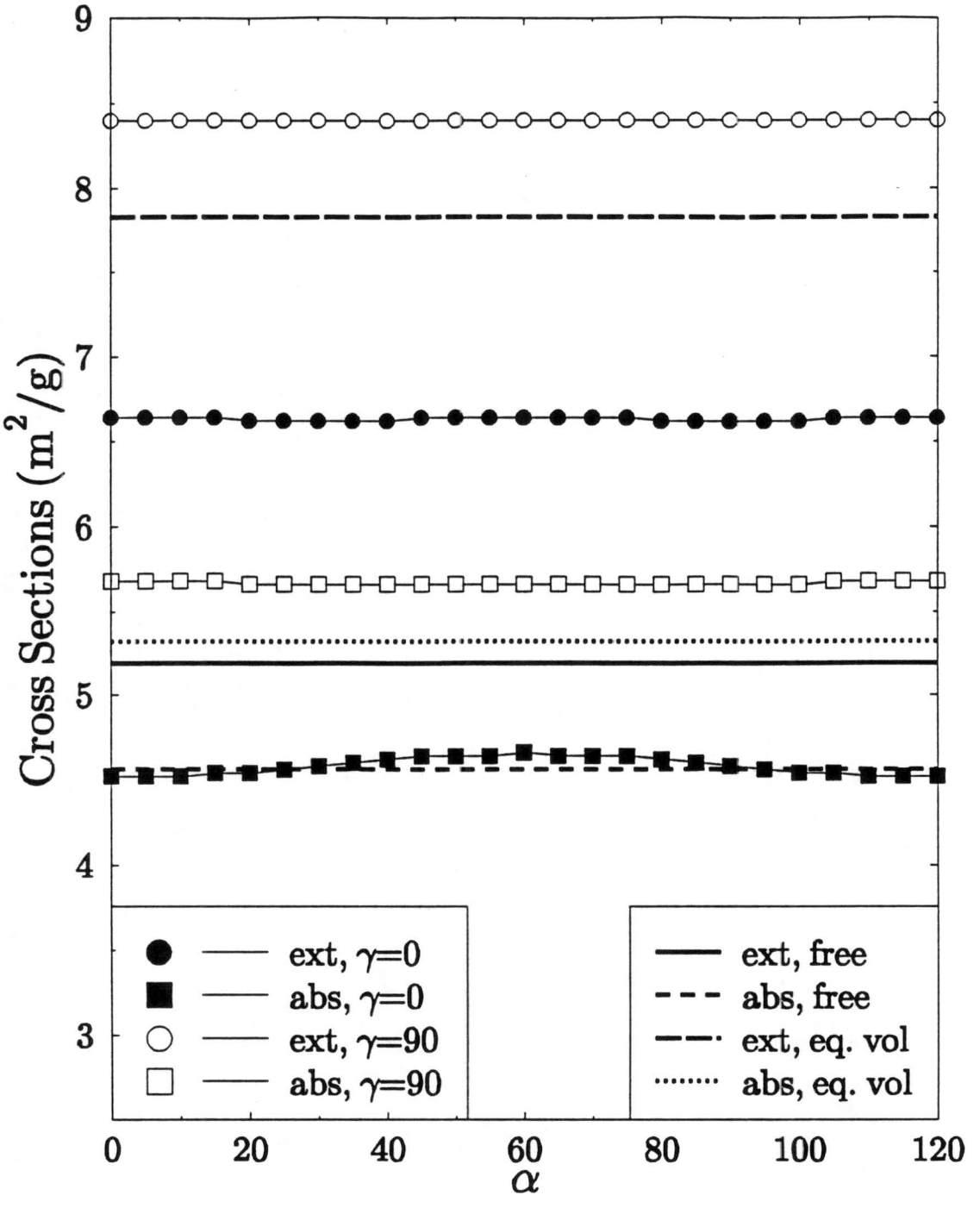
Cross Sections (m^2/g)
9
8
7
6
5
4
3
0
20
40
60
80
100
120
α
ext, γ=0
abs, γ=0
ext, γ=90
abs, γ=90
ext, free
abs, free
ext, eq. vol
abs, eq. vol

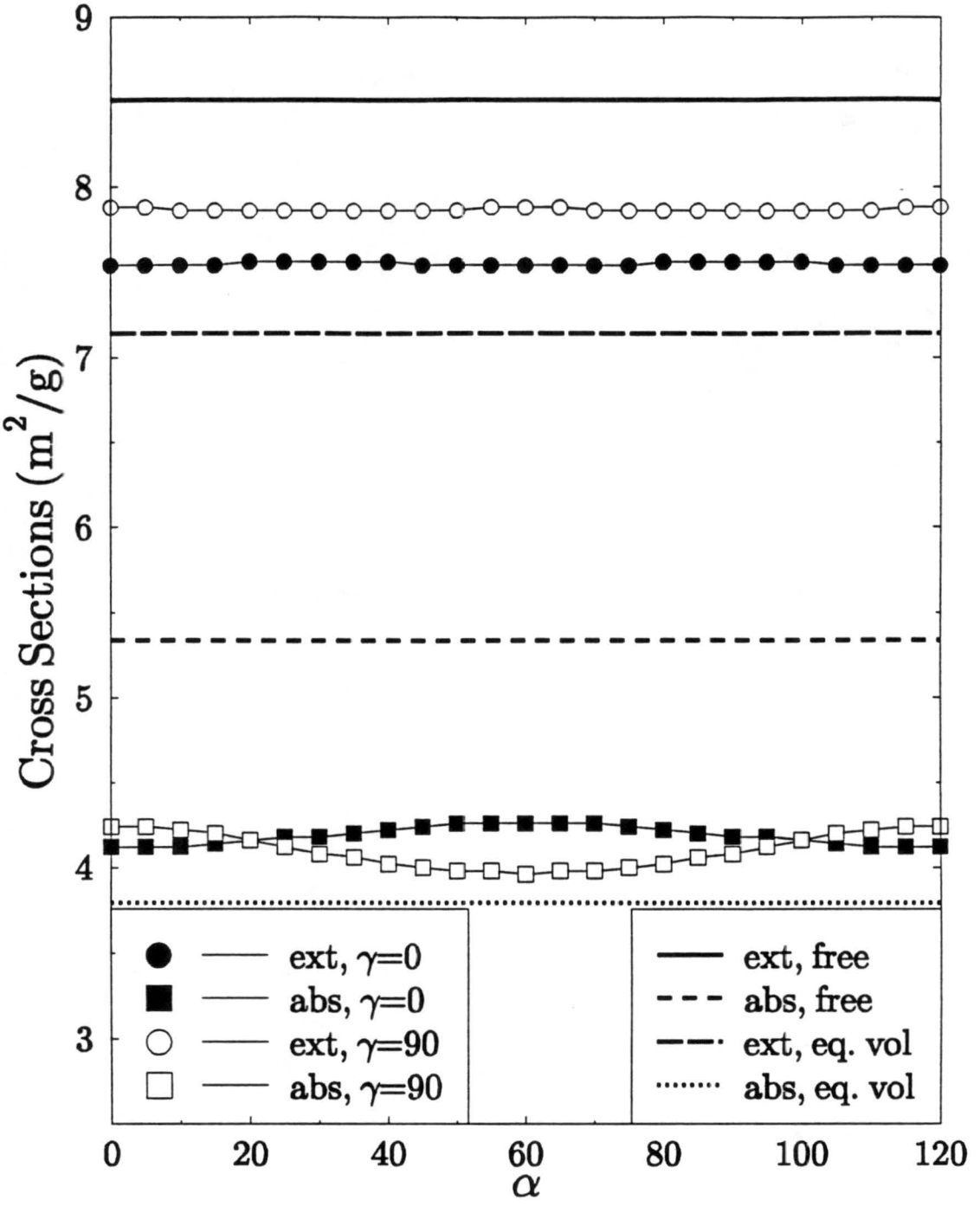
Cross Sections (m^2/g)
9
8
7
6
5
4
3
0
20
40
60
80
100
120
α
ext, γ=0
abs, γ=0
ext, γ=90
abs, γ=90
ext, free
abs, free
ext, eq. vol
abs, eq. vol

Table I. Single Particle Cross Sections for Carbon Spheres (m^2/g)

Free Carbon (fc)			Equivalent-volume sphere			size parameter
3.702	0.004	3.698	3.803	0.024	3.779	ka=0.1142
5.192	0.630	4.562	7.828	2.507	5.321	ka=0.5712
8.512	3.174	5.338	7.144	3.348	3.796	ka=1.1420

Table II. Orientaion-Averaged Specific Absorption of Scavenged Carbon Grains on Aerosol Surfaces (m^2/g)

C Radius (μm)	$\langle A_a \rangle$ $\gamma = 0$	$\gamma = 90$	Droplet Size/Species
0.01	8.574	4.893	
0.05	7.896	5.203	0.5 μm sulfate
0.10	6.503	5.337	
0.01	8.816	2.267	
0.05	6.845	3.072	1.0 μm sulfate
0.10	5.319	4.747	
0.01	4.136	2.469	
0.05	4.665	3.164	3.0 μm water
0.10	5.214	4.424	
0.01	4.236	3.586	
0.05	4.673	4.324	5.0 μm water
0.10	5.013	5.192	

Table III. Ratio of Specific Absorption of Scavenged Carbon to Free Carbon

C Radius (μm)	$\gamma = 0$	$\gamma = 90$	$\langle \rangle_\gamma$	Droplet Size/Species
0.01	2.320	1.324	1.822	
0.05	1.730	1.140	1.435	0.5 μm sulfate
0.10	1.218	0.999	1.109	
0.01	2.386	0.613	1.500	
0.05	1.499	0.673	1.086	1.0 μm sulfate
0.10	0.996	0.889	0.943	
0.01	1.119	0.668	0.894	
0.05	1.022	0.693	0.858	3.0 μm water
0.10	0.976	0.828	0.902	
0.01	1.146	0.971	1.059	
0.05	1.024	0.947	0.986	5.0 μm water
0.10	0.939	0.972	0.956	

surface of a cloud droplet can thus be expected to absorb slightly less sunlight than if it existed interstitially within the cloud.

It is not hard to visualize situations where ramified structures would display preferred orientations: Filaments aligned aerodynamically to maximize viscous drag or oriented in laminar flows so as to minimize torque are two obviuos examples. There are, however, more scattering geometries specific to particular problems than can be considered in this context at the present time. The linear chains, therefore, are allowed to assume all orientations and Eq. 4 will be used, as it was in the case of the droplet/soot composite particles. It is not difficult, given the data provided in Figs. 11–13, to estimate $\langle A \rangle$ using Eq. 5 should the need arise.

Eq. 5 is applied to the tightly packed carbon clusters considered in Figs. 14–16. An extensive investigation of ensemble averages of the optical properties of three-dimensionally configured sphere centers would be an appropriate topic for further research, but it is not the subject of the present study: Here the averages are taken in order to gain some initial insights into the influence of dependent scattering by comparing calculations made thus far with the properties of the single carbon spheres listed in Table I.

Averages, taken as described above, for the extinction, scattering, and aborption cross sections of the carbon agglomerates are provided in Table IV. As can be inferred from Figs. 11 and 14, scattering is negligible for the aggregates comprised of the 0.01μm spherules. Even where scattering is not negligible, it is still dominated by absorption, as is the case for the single spheres in Table 1.

As noted earlier, there are some approximations that are routinely used in the fractal analysis of light extinction by soot that can now be tested against exact calculations. The two approximations considered here are: (1) that multiple scattering within the aggregate is small and (2) that absorption by the cluster is proportional to the total volume of the absorbing material, i.e., the absorption cross section of the aggregate can be inferred from that of an equivalent volume sphere.[17] Table V lists the ratios of the respective cross sections of the straight chain and aciniform aggregates, after polarization-averaging, to those of free carbon and of equivalent volume spheres.

For the 0.01μm grains, the absorption cross sections of the aggregates are seen to be from 11 to 14% larger than those of the free carbon or of the equivalent volume sphere, with the larger difference involving the free carbon. For the 0.05μm spherules, A_{fc} underestimates σ_a for the aggregates by about 10%, whereas this cross section is overestimated by the equivalent volume sphere, although the error is still only a few percent. The reverse is true for the 0.10μm monomers and the error in the equivalent volume approximation is found to be about 20%. It should be pointed out that Sorensen et al.[17] employ monomers comparable to the 0.01μm grains.

A bit of caution is to be used in interpretating the ratios of the scattering cross sections of the aggregates to those of the free carbon. The number of monomers in a cluster of identical particles is implicit in the particle volume appearing in Eq. 2. For small particles, however, the scattering cross section is proportional to the square of the volume so that if a cluster of L small spheres is itself smaller than the wavelength, the above ratio would be L if there were no cross talk among the monomers. (This matter is discussed more fully in Section 4 of Part I.) The proportionality to L^2 is taken into account in fractal research and the scattering cross

Table IV. Mass Cross Sections for Sphere Aggregates

Linear Chains of Five Spheres (m^2/g)

$\gamma = 0°$			$\gamma = 90°$			monomer size
Ext	Sca	Abs	Ext	Sca	Abs	
5.368	0.032	5.335	3.118	0.019	3.098	ka=0.1142
8.132	2.103	6.030	4.975	1.099	3.873	ka=0.5712
8.926	4.150	4.778	7.323	3.076	4.247	ka=1.1420

Close-Packed Hexahedral Cluster

$\gamma = 0°$			$\gamma = 90°$			monomer size
Ext	Sca	Abs	Ext	Sca	Abs	
3.720	0.023	3.700	4.740	0.030	4.720	ka=0.1142
6.632	2.047	4.583	8.400	2.740	5.666	ka=0.5712
7.548	3.358	4.189	7.865	3.771	4.097	ka=1.1420

Table V. Ratios of Aggregate to Single Sphere Cross Sections

Linear Chains of Five Spheres

(Averaged cross sections)/fc			(Averaged cross sections)/eqv			monomer size
Ext	Sca	Abs	Ext	Sca	Abs	
1.146	6.384	1.140	1.115	1.063	1.116	ka=0.1142
1.262	2.541	1.085	0.837	0.639	0.931	ka=0.5712
0.954	1.138	0.845	1.137	1.079	1.189	ka=1.1420

Close-Packed Hexahedral Cluster

(Averaged cross sections)/fc			(Averaged cross sections)/eqv			monomer size
Ext	Sca	Abs	Ext	Sca	Abs	
1.143	6.663	1.139	1.112	1.110	1.114	ka=0.1142
1.448	3.799	1.123	0.960	0.955	0.963	ka=0.5712
0.905	1.123	0.776	1.079	1.065	1.091	ka=1.1420

sections of the 0.01μm sphere aggregates in Table V should be divided by another factor of five when testing the L^2 (Rayleigh) approximation of light scattering employed in the study of fractal aggregates. Thus the error in the approximation is about 30%, rather than the over 600% that one might infer from Table V. The use of the Rayleigh approximation for scattering by the 0.05μm grains breaks down and the scattering cross sections of the aggregates simply cannot be approximated in terms of free carbon. When these monomers are tightly clumped, their scattering cross section is approximated well by that of an equivalent volume sphere, but for the ramified structures, no reasonable approximation for the total scattering is obvious. (An equivalent area sphere was also considered, but the error for such an approximation was even greater than those for the free carbon and equivalent volume approximations.) The interactions between the 0.10μm spheres are not strong enough to produce an error of more than about 15% in the scattering cross sections of the aggregates relative to that of free carbon, but the agreement with the equivalent volume approximation is better still.

J. Quant. Spectrosc. Radiat. Transfer Vol. 48, No. 1, pp. 41–59, 1992
Printed in Great Britain.

0022-4073/92 $5.00 + 0.00

Chapter IV. Accelerated Quasi Monte Carlo Integration of the Radiative Transfer Equation

D. M. O'BRIEN
CSIRO, Division of Atmospheric Research, Private Bag No. 1, Mordialloc, Victoria 3195, Australia

(Received 7 October 1991)

Abstract—Backward Monte Carlo integration of the radiative transfer equation is the technique most easily adapted to complex scattering geometries. However, backward Monte Carlo integration suffers from two disadvantages: the accuracy is often low because the solution calls for the evaluation of high-dimensional integrals, and convergence of the multiple scattering series is slow if the photons are only weakly absorbed by the medium. In this paper, we demonstrate that the errors from both sources can be substantially reduced. First, the multi-dimensional integrals can be evaluated more accurately and more efficiently with *quasi* Monte Carlo integration, a technique in which photon trajectories are selected to sample the integration domain optimally. Second, the convergence of the multiple scattering series can be accelerated by estimating the rate of decay of the tail of the series. Each of the techniques described in the paper is both robust and applicable to scattering with any geometry.

1. INTRODUCTION

There are many problems in atmospheric radiation which require the solution of the radiative transfer equation (RTE) in complex media. Examples range from visibility studies, such as those undertaken to model haze in the Grand Canyon,[1] to efforts to model the shortwave and longwave fluxes transmitted by fields of broken cloud.[2,3] Although some attempts have been made to adapt techniques for plane parallel media to complex geometries,[4,5] essentially by developing the optical properties in Fourier series and replacing the RTE by coupled equations for the Fourier components, the technique which can be adapted most easily to complex geometries is that of Monte Carlo (MC) integration. Indeed, there is a distinguished history of applications of MC integration to cloud radiation, dating from the early studies by McKee and Cox,[6] which demonstrated the importance of the finite dimensions of clouds, through to more recent studies of ensembles of clouds.[7] An excellent treatment of Monte Carlo techniques in atmospheric optics can be found in the book by Marchuk et al.[8]

However, there are two serious difficulties with backward MC integration, both of which arise because the simulation of photon trajectories is logically equivalent to summation of the multiple scattering series. These difficulties are that (i) each term of the multiple scattering series requires evaluation of a high-dimensional integral, a process which can be very costly if high accuracy is required, and (ii) the accuracy of backward MC integration is poor when the medium is optically thick or has low absorption because the convergence of the multiple scattering series is then slow.

The first objective of this paper is to draw attention to work on quasi Monte Carlo (QMC) integration, a technique which can significantly reduce the costs incurred in the evalution of the integrals in the multiple scattering series. It is well known that the error in statistical, or random, Monte Carlo (RMC) estimation of integrals has order $N^{-1/2}$, where N is the number of simulated photon trajectories. Perhaps less well known in the radiation community is the existence of QMC techniques for which the error has order $N^{-1}(\log N)^d$, where d is the dimension of the integration. Examples will be given in the paper to illustrate the improvement in computational efficiency obtained with QMC integration of the RTE.

The second objective of the paper is to introduce a technique for accelerating the convergence of the multiple scattering series. If I_k denotes the contribution to the radiance from kth order scattering, and if S_n denotes the nth partial sum of the multiple scattering series

$$S_n = \sum_{k=0}^{n} I_k,$$

then the convergence of the sequence S_n to the radiance I is monotonic because the terms I_k are all positive. The error term, E_{n+1}, defined by

$$I = S_n + E_{n+1},$$

is unknown because it involves the radiance. However, a related quantity, R_{n+1}, obtained formally from the error term by setting the radiance to unity, can be computed for negligible extra cost as a by-product of the calculation of S_n. The sequence

$$Q_n(\nu) = \frac{S_n}{1 - \nu R_{n+1}}, \quad 0 \leqslant \nu \leqslant 1,$$

also converges to the radiance for any ν in the range (0, 1). It will be shown in this paper that there is a critical value of ν, denoted ν_*, for which the convergence of the sequence $Q_n(\nu_*)$ is both monotonic and optimal, in the sense that it is faster than the convergence of $Q_n(\nu)$ with any smaller ν. In particular, $Q_n(\nu_*)$ converges more rapidly than S_n. The estimation of ν_* is straightforward and computationally inexpensive. The importance of this convergence acceleration technique is that it significantly extends the range of optical thicknesses where both QMC and RMC integration are efficient.

Each of the techniques described in this paper is both robust and applicable to scattering with any geometry.

The paper contains four sections. The first is concerned with multiple scattering in an arbitrary medium. The second section outlines the essential elements of RMC and QMC integration and demonstrates that the standard variance reduction techniques of RMC integration are trivially included in QMC integration. Section 3 compares the computational efficiencies of RMC and QMC integration in solving the RTE for several test problems. Section 4 describes the convergence acceleration algorithm.

1. MULTIPLE SCATTERING

Consider a domain X of arbitrary shape containing a scattering medium whose coefficients of absorption, scattering and extinction, denoted by $\alpha(\mathbf{x})$, $\beta(\mathbf{x})$ and $\gamma(\mathbf{x})$, may depend upon position $\mathbf{x}$ within X. If there are no sources of radiation within the medium, then the radiance at point $\mathbf{x}$ in direction specified by unit vector $\mathbf{s}$, denoted $I(\mathbf{x}, \mathbf{s})$, satisfies the radiative transfer equation (RTE),

$$\mathbf{s} \cdot \nabla I(\mathbf{x}, \mathbf{s}) = -\gamma(\mathbf{x}) I(\mathbf{x}, \mathbf{s}) + \beta(\mathbf{x}) \int_\Omega \mathrm{d}\Omega(\mathbf{s}') p(\mathbf{x}, \mathbf{s}, \mathbf{s}') I(\mathbf{x}, \mathbf{s}'). \tag{1}$$

In this equation, $p(\mathbf{x}, \mathbf{s}, \mathbf{s}')$ denotes the phase function for scattering from direction $\mathbf{s}'$ into direction $\mathbf{s}$, and $\mathrm{d}\Omega(\mathbf{s}')$ denotes the solid angle centred on $\mathbf{s}'$,

$$\mathrm{d}\Omega(\mathbf{s}') = \frac{1}{4\pi} \sin\theta' \, \mathrm{d}\theta' \, \mathrm{d}\phi', \tag{2}$$

where θ' and ϕ' are the zenith and azimuth angles of $\mathbf{s}'$. The solid angle and the phase function are normalized so that

$$\int_\Omega \mathrm{d}\Omega(\mathbf{s}') = 1 \tag{3}$$

and

$$\int_\Omega \mathrm{d}\Omega(\mathbf{s}') p(\mathbf{x}, \mathbf{s}, \mathbf{s}') = 1. \tag{4}$$

In order to complete the specification of the scattering problem, a condition must be imposed on the radiance on the boundary of X. The condition will vary with the problem, but, for the purposes of this paper, it suffices to choose the canonical boundary condition in which the inward pointing radiance is specified at all boundary points of X. The extensions to cover the cases of polarized radiation, internal thermal sources and a partly reflecting boundary are straightforward.

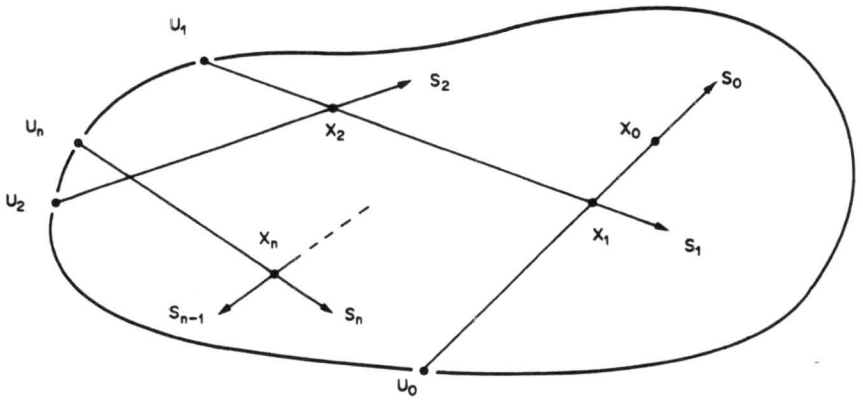

Fig. 1. Multiple scattering geometry.

The integral form of the RTE asserts that the radiance at point $\mathbf{x}_0$ in direction $\mathbf{s}_0$ is given by

$$I(\mathbf{x}_0, \mathbf{s}_0) = t(\mathbf{x}_0, \mathbf{u}_0) I(\mathbf{u}_0, \mathbf{s}_0) + \int_{\mathbf{u}_0}^{\mathbf{x}_0} \mathrm{d}\mathbf{x}_1 \, t(\mathbf{x}_0, \mathbf{x}_1) \beta(\mathbf{x}_1) \int_{\Omega} \mathrm{d}\Omega(\mathbf{s}_1) p(\mathbf{x}_1, \mathbf{s}_0, \mathbf{s}_1) I(\mathbf{x}_1, \mathbf{s}_1), \tag{5}$$

where $\mathbf{u}_0$ is the boundary point found by retracing the ray through point $\mathbf{x}_0$ in direction $\mathbf{s}_0$, the line integral along the ray from $\mathbf{u}_0$ to $\mathbf{x}_0$ is denoted by

$$\int_{\mathbf{u}_0}^{\mathbf{x}_0} \mathrm{d}\mathbf{x}_1 \ldots, \tag{6}$$

the transmittance of the medium between points $\mathbf{x}'$ and $\mathbf{x}$ is denoted by $t(\mathbf{x}, \mathbf{x}')$ and given by

$$t(\mathbf{x}, \mathbf{x}') = \exp[-l(\mathbf{x}, \mathbf{x}')], \tag{7}$$

with $l(\mathbf{x}, \mathbf{x}')$ representing the optical path length between the points,

$$l(\mathbf{x}, \mathbf{x}') = \int_{\mathbf{x}'}^{\mathbf{x}} \mathrm{d}\mathbf{x}'' \gamma(\mathbf{x}''). \tag{8}$$

The multiple scattering series solution of Eq. (5) is obtained by iterating the integral equation. With reference to Fig. 1, the radiance after n iterations may be written as

$$I(\mathbf{x}_0, \mathbf{s}_0) = \sum_{k=0}^{n} I_k(\mathbf{x}_0, \mathbf{s}_0) + E_{n+1}(\mathbf{x}_0, \mathbf{s}_0), \tag{9}$$

where I_0 denotes the radiance transmitted directly from the boundary,

$$I_0(\mathbf{x}_0, \mathbf{s}_0) = t(\mathbf{x}_0, \mathbf{u}_0) I(\mathbf{u}_0, \mathbf{s}_0), \tag{10}$$

while I_k, for $k \geqslant 1$, denotes the radiance which has been scattered k times,

$$I_k(\mathbf{x}_0, \mathbf{s}_0) = \int_{\mathbf{u}_0}^{\mathbf{x}_0} \mathrm{d}\mathbf{x}_1 \, t(\mathbf{x}_0, \mathbf{x}_1) \beta(\mathbf{x}_1) \int_{\Omega} \mathrm{d}\Omega(\mathbf{s}_1) p(\mathbf{x}_1, \mathbf{s}_0, \mathbf{s}_1) \cdots$$
$$\cdots \times \int_{\mathbf{u}_{k-1}}^{\mathbf{x}_{k-1}} \mathrm{d}\mathbf{x}_k \, t(\mathbf{x}_{k-1}, \mathbf{x}_k) \beta(\mathbf{x}_k) \int_{\Omega} \mathrm{d}\Omega(\mathbf{s}_k) p(\mathbf{x}_k, \mathbf{s}_{k-1}, \mathbf{s}_k) t(\mathbf{x}_k, \mathbf{u}_k) I(\mathbf{u}_k, \mathbf{s}_k). \tag{11}$$

In Eq. (11), $\mathbf{u}_i$ is the boundary point found by retracing the ray through scattering point $\mathbf{x}_i$ in direction $\mathbf{s}_i$, $i = 0, \ldots, k$. The remainder after n iterations, E_{n+1}, still involves the unknown radiance,

$$E_{n+1}(\mathbf{x}_0, \mathbf{s}_0) = \int_{\mathbf{u}_0}^{\mathbf{x}_0} \mathrm{d}\mathbf{x}_1 \, t(\mathbf{x}_0, \mathbf{x}_1) \beta(\mathbf{x}_1) \int_{\Omega} \mathrm{d}\Omega(\mathbf{s}_1) p(\mathbf{x}_1, \mathbf{s}_0, \mathbf{s}_1) \cdots$$
$$\cdots \times \int_{\mathbf{u}_n}^{\mathbf{x}_n} \mathrm{d}\mathbf{x}_{n+1} \, t(\mathbf{x}_n, \mathbf{x}_{n+1}) \beta(\mathbf{x}_{n+1}) \int_{\Omega} \mathrm{d}\Omega(\mathbf{s}_{n+1}) p(\mathbf{x}_{n+1}, \mathbf{s}_n, \mathbf{s}_{n+1}) I(\mathbf{x}_{n+1}, \mathbf{s}_{n+1}). \tag{12}$$

However, under rather general conditions which will be established later, the remainder converges to zero as $n \to \infty$, so the sequence of partial sums, defined by

$$S_n(\mathbf{x}_0, \mathbf{s}_0) = \sum_{k=0}^{n} I_k(\mathbf{x}_0, \mathbf{s}_0), \tag{13}$$

converges to the radiance.

Transformation of the line integrals

Each of the line integrals in Eq. (11) can be reduced to integration over the unit interval by simple changes of variable. First, the transmittance $t'(\mathbf{x}, \mathbf{x}')$ and the extinction $\gamma(\mathbf{x}')$ are related by

$$\mathrm{d}t'/\mathrm{d}\mathbf{x}' = \gamma(\mathbf{x}')t'(\mathbf{x}, \mathbf{x}'), \tag{14}$$

where the prime on t' indicates that it is to be regarded as a function of $\mathbf{x}'$. This approach permits a typical line integral to be transformed as follows:

$$\begin{aligned} \mathscr{X} &= \int_{\blacksquare}^{\mathbf{x}} \mathrm{d}\mathbf{x}' t'(\mathbf{x}, \mathbf{x}')\beta(\mathbf{x}') \cdots \\ &= \int_{\blacksquare}^{\mathbf{x}} \mathrm{d}\mathbf{x}' \frac{\mathrm{d}t'}{\mathrm{d}\mathbf{x}'} \beta(\mathbf{x}')/\gamma(\mathbf{x}') \cdots \\ &= \int_{t(\mathbf{x}, \mathbf{u})}^{1} \mathrm{d}t' \varpi(\mathbf{x}') \cdots, \end{aligned} \tag{15}$$

where $\varpi(\mathbf{x}')$ is the single scattering albedo,

$$\varpi(\mathbf{x}') = \beta(\mathbf{x}')/\gamma(\mathbf{x}'). \tag{16}$$

Second, if ϵ' denotes the distance to the next scattering point, expressed as a fraction of the total optical path length to the boundary along the ray through $\mathbf{x}$,

$$\epsilon' = \frac{t' - t(\mathbf{x}, \mathbf{u})}{1 - t(\mathbf{x}, \mathbf{u})}, \tag{17}$$

then it is clear that

$$0 \leqslant \epsilon' \leqslant 1 \tag{18}$$

and that

$$\mathscr{X} = a(\mathbf{x}, \mathbf{u}) \int_0^1 \mathrm{d}\epsilon' \varpi(\mathbf{x}') \cdots, \tag{19}$$

where $a(\mathbf{x}, \mathbf{u})$ is the absorption along the path from boundary point $\mathbf{u}$ to point $\mathbf{x}$,

$$a(\mathbf{x}, \mathbf{u}) = 1 - t(\mathbf{x}, \mathbf{u}). \tag{20}$$

The point $\mathbf{x}'$ which appears in the integrand of Eq. (19) must be determined from ϵ' by solving Eq. (17) for t' in terms of ϵ', and by solving Eqs. (7) and (8) for $\mathbf{x}'$ in terms of t'. It is in these calculations that the major cost of MC integration of the RTE is incurred.

Transformation of the angular integrals

In most applications the phase function depends only upon the scattering angle ψ', defined to be the angle between the vectors $\mathbf{s}$ and $\mathbf{s}'$,

$$\cos \psi' = \mathbf{s} \cdot \mathbf{s}', \tag{21}$$

and not upon the absolute orientation of the vectors. When this is the case, the polar axis of integration over $\mathbf{s}'$ appearing in a typical angular integration in Eq. (11),

$$\mathscr{Y} = \int_{\Omega} \mathrm{d}\Omega(\mathbf{s}') p(\mathbf{x}, \mathbf{s}, \mathbf{s}') \cdots, \tag{22}$$

may be aligned with **s** without changing the value of $\mathscr{Y}$. This permits $\mathscr{Y}$ to be written in the form

$$\mathscr{Y} = \int_0^{2\pi} \frac{d\phi'}{2\pi} \int_0^{\pi} \frac{d\psi'}{2} \sin\psi' p(\mathbf{x}, \cos\psi') \cdots . \tag{23}$$

The integration can be reduced to an integral over the unit square with new variables ζ' and η', defined by

$$\zeta' = \frac{\phi'}{2\pi} \tag{24}$$

and

$$\eta'(\mathbf{x}, \psi') = \frac{1}{2} \int_0^{\psi'} d\psi \sin\psi p(\mathbf{x}, \cos\psi). \tag{25}$$

Because

$$\frac{d\eta'}{d\psi'} = \tfrac{1}{2} \sin\psi' p(\mathbf{x}, \cos\psi'), \tag{26}$$

it follows easily that

$$\mathscr{Y} = \int_0^1 d\zeta' \int_0^1 d\eta' \cdots . \tag{27}$$

The integrand in Eq. (27) still depends upon both direction vectors **s** and **s'**, which must be reconstructed from ζ' and η' by reversing the mappings outlined above.

As a result of the coordinate changes discussed above, the contribution to the radiance from kth order scattering can be represented as an integral over the $3k$ dimensional unit cube,

$$I_k(\mathbf{x}_0, \mathbf{s}_0) = \int_0^1 d\epsilon_1 \int_0^1 d\zeta_1 \int_0^1 d\eta_1 \cdots \int_0^1 d\epsilon_k \int_0^1 d\zeta_k \int_0^1 d\eta_k \times \varpi(\mathbf{x}_1) \cdots \varpi(\mathbf{x}_k) a(\mathbf{x}_0, \mathbf{u}_0) \cdots a(\mathbf{x}_{k-1}, \mathbf{u}_{k-1}) t(\mathbf{x}_k, \mathbf{u}_k) I(\mathbf{u}_k, \mathbf{s}_k). \tag{28}$$

The integral can also be written in the more compact form

$$I_k = \int f_k(\mathbf{z})\, d\mathbf{z}, \tag{29}$$

where **z** denotes the point in the $3k$ dimensional cube with components

$$\mathbf{z} = (\epsilon_1, \zeta_1, \eta_1, \epsilon_2, \zeta_2, \eta_2, \ldots, \epsilon_k, \zeta_k, \eta_k) \tag{30}$$

and

$$f_k(\mathbf{z}) = \varpi(\mathbf{x}_1) \cdots \varpi(\mathbf{x}_k) a(\mathbf{x}_0, \mathbf{u}_0) \cdots a(\mathbf{x}_{k-1}, \mathbf{u}_{k-1}) t(\mathbf{x}_k, \mathbf{u}_k) I(\mathbf{u}_k, \mathbf{s}_k). \tag{31}$$

The conditions for convergence of the series are now apparent from Eq. (28): the medium must either be absorbing, so that $\varpi(\mathbf{x}) < 1$ for all **x**, or be finite in optical thickness, so that $a(\mathbf{x}, \mathbf{u}) < 1$ for all **x** and **u**.

It is worth noting the special (but important) case in which the source of illumination consists of a collimated beam from direction $\mathbf{s}_*$ with flux density F, together with a diffuse incident radiance denoted by J. The radiance incident upon the medium at boundary point **u** in direction **s** becomes

$$I(\mathbf{u}, \mathbf{s}) = \frac{F}{4\pi} \delta(\mathbf{s}, \mathbf{s}_*) + J(\mathbf{u}, \mathbf{s}) \tag{32}$$

and the kth order scattering term can be decomposed into a 'solar' component A_k and a 'diffuse' component B_k, i.e.

$$I_k(\mathbf{x}_0, \mathbf{s}_0) = A_k(\mathbf{x}_0, \mathbf{s}_0) + B_k(\mathbf{x}_0, \mathbf{s}_0), \tag{33}$$

given by

$$A_k(\mathbf{x}_0, \mathbf{s}_0) = \frac{F}{4\pi} \int_0^1 d\epsilon_1 \int_0^1 d\zeta_1 \int_0^1 d\eta_1 \cdots \int_0^1 d\epsilon_{k-1} \int_0^1 d\zeta_{k-1} \int_0^1 d\eta_{k-1} \int_0^1 d\epsilon_k$$
$$\times \varpi(\mathbf{x}_1) \cdots \varpi(\mathbf{x}_k) a(\mathbf{x}_0, \mathbf{u}_0) \cdots a(\mathbf{x}_{k-1}, \mathbf{u}_{k-1}) t(\mathbf{x}_k, \mathbf{u}_k) p(\mathbf{x}_k, \mathbf{s}_{k-1}, \mathbf{s}_*) \quad (34)$$

and

$$B_k(\mathbf{x}_0, \mathbf{s}_0) = \int_0^1 d\epsilon_1 \int_0^1 d\zeta_1 \int_0^1 d\eta_1 \cdots \int_0^1 d\epsilon_k \int_0^1 d\zeta_k \int_0^1 d\eta_k$$
$$\times \varpi(\mathbf{x}_1) \cdots \varpi(\mathbf{x}_k) a(\mathbf{x}_0, \mathbf{u}_0) \cdots a(\mathbf{x}_{k-1}, \mathbf{u}_{k-1}) t(\mathbf{x}_k, \mathbf{u}_k) J(\mathbf{u}_k, \mathbf{s}_k). \quad (35)$$

In summary, the contribution to the radiance from processes involving k scattering events can be reduced by simple changes of the variables to an integration over the $3k$ dimensional unit cube. If the source is collimated, as in the case of the solar beam, then the dimension can be further reduced to $3k - 2$. The next section discusses the evaluation of such integrals and their connection with the conventional, statistical interpretation of RMC integration, according to which radiances are computed as weighted averages of photon trajectories.

2. MONTE CARLO INTEGRATION

The simplest estimate of the integral

$$\mathscr{I} = \int f(\mathbf{z})\, d\mathbf{z} \quad (36)$$

of the function f over a d dimensional cube is

$$\mathscr{I}^{(N)} = \frac{1}{N} \sum_{i=1}^{N} f(\mathbf{z}_i), \quad (37)$$

where the points $\mathbf{z}_i$, $i = 1, 2, \ldots, N$, are chosen within the cube. The estimate $\mathscr{I}^{(N)}$ is just the average value of the integrand at the selected points. Alternatively, $f(\mathbf{z}_i)$ may be interpreted as a statistical weight associated with the 'event' $\mathbf{z}_i$, in which case the integral value is the weighted average of all the sampled events. For example, in the evaluation of I_k in Eq. (28), the components of each point $\mathbf{z}_i$ determine a photon trajectory whose associated weight is f_k, defined in Eq. (31), so the integral estimate afforded by Eq. (37) becomes a weighted sum of photon trajectories. Furthermore, the weight f_k has a simple physical interpretation. Each of the factors $\varpi(\mathbf{x}_i)$ represents the probability of survival of the photon in the corresponding collision. The factor $a(\mathbf{x}_{i-1}, \mathbf{u}_{i-1})$ is a weight introduced to remove the bias caused by forcing collisions to occur within the medium along the path from $\mathbf{u}_{i-1}$ to $\mathbf{x}_{i-1}$. The variable change from ψ' and η' ensures representative sampling of the phase function. In the parlance of RMC integration, the purpose of the weight is to bias the distribution of photon trajectories towards the physical distribution. This process is an example of the general procedure of 'variance reduction'. The weights described above are the most commonly used because they are universally applicable and do not rely upon specific properties of the scattering medium. It is clear that variance reduction is implicit in Eq. (28).

In RMC integration, the points $\mathbf{z}_i$, $i = 1, 2, \ldots N$, are chosen randomly in the unit cube. It is well known that the error in the corresponding estimate $\mathscr{I}^{(N)}$ has order $N^{-1/2}$:

$$|\mathscr{I} - \mathscr{I}^{(N)}| = O(N^{-1/2}). \quad (38)$$

However, in QMC integration the points $\mathbf{z}_i$ are chosen according to a strategy designed to minimize the *discrepancy* of the set of points, a quantity which measures the uniformity with which the points are distributed in the unit cube. In order to define the discrepancy, let (i) $\mathbf{z}$ denote any point in the unit cube, (ii) $M(\mathbf{z})$ denote the number points in the rectangular subregion with its minimum vertex at the origin and its maximum vertex at the point $\mathbf{z}$, (iii) $\Delta^{(N)}(\mathbf{z})$ denote the difference between the fraction of points in the subregion and the volume of the subregion, i.e.,

$$\Delta^{(N)}(\mathbf{z}) = \frac{M(\mathbf{z})}{N} - z_1 z_2 \cdots z_d, \quad (39)$$

where $z_1, z_2, \cdots, z_d$ denote the components of the vector $\mathbf{z}$. The discrepancy is the maximum value of the function $\Delta^{(N)}(\mathbf{z})$ as the point $\mathbf{z}$ varies over the unit cube,

$$D^{(N)} = \sup_{\mathbf{z}} \Delta^{(N)}(\mathbf{z}). \tag{40}$$

If the points are distributed uniformly, then the fraction of points in any subregion ought to be nearly proportional to the volume of the subregion, in which case the discrepancy ought to be small.

The importance of the discrepancy to QMC integration lies in the following inequality for the error in the estimate $\mathscr{I}^{(N)}$:

$$|\mathscr{I} - \mathscr{I}^{(N)}| \leqslant V(f)D^{(N)}, \tag{41}$$

where $V(f)$ is the *variation*[9] of the function f and $D^{(N)}$ is the discrepancy of the selected set of points. Thus, the error is bounded by the product of two factors, one of which measures the 'lumpiness' of the function, and the other the 'lumpiness' of the distribution of points. Clearly, without *a priori* information regarding the integrand, the best strategy for minimizing the error in the estimate of the integral is to choose points with small discrepancy.

The search for point sets with low discrepancy is an active area of mathematics, whose principal results can be found in a survey by Niederreiter.[10] However, in this paper attention will be focused on one particular set of points, called the Halton[11] sequence, for which

$$D^{(N)} = O[N^{-1}(\log N)^d]. \tag{42}$$

The Halton sequence consists of points

$$\mathbf{z}_i = (\varphi_{R_1}(i), \varphi_{R_2}(i), \ldots, \varphi_{R_d}(i)), \tag{43}$$

where $\varphi_R(\mathrm{i})$ is the *radical inverse function*, which maps each integer i into a real number in the interval (0, 1) by reflecting the representation of i in base R arithmetic in the decimal point. The bases $R_1, R_2, \ldots R_d$ must be relatively prime and are usually taken to be the first d prime numbers. Details of a computationally efficient algorithm for calculating the sequence are given by Halton and Smith.[12]

Figure 2 compares randomly selected points in two dimensions with the Halton sequence. For $N = 10$ there is little to choose between the coverage of the two sets of points, but for $N = 100$

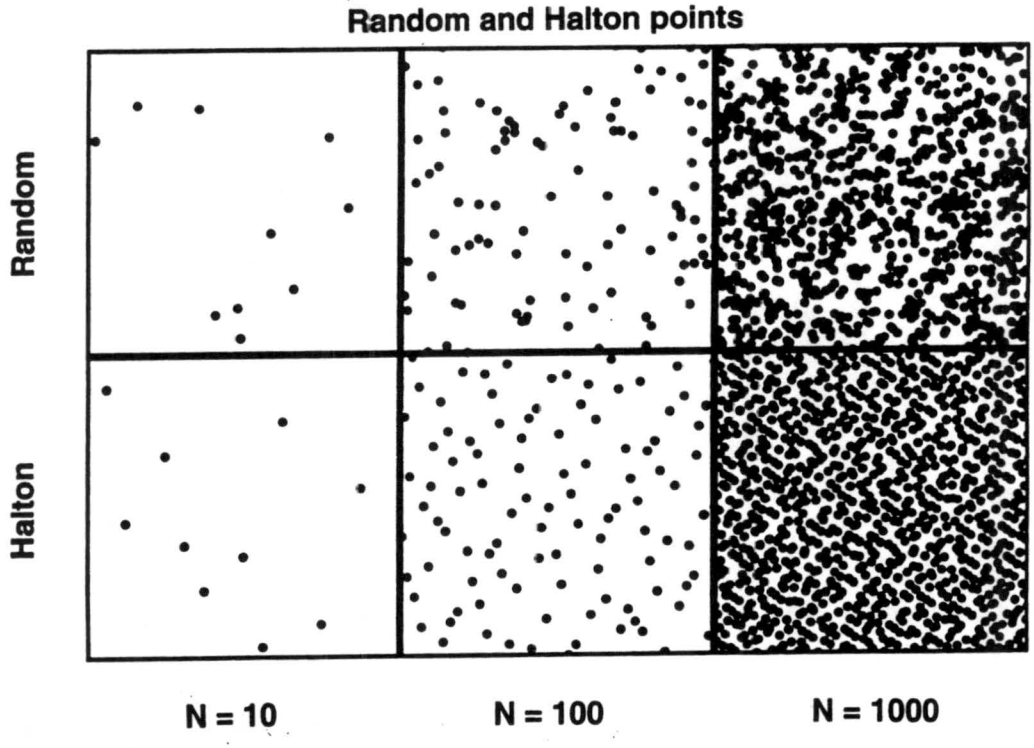

Fig. 2. Distribution of random and Halton points in two dimensions for $N = 10$, 100, 1000.

and $N = 1000$ the more uniform coverage of the Halton sequence is obvious. In the context of integration over the unit square, the Halton sequence will sample the integrand uniformly, whereas randomly selected points will undersample the integrand in some regions while oversampling in others, leading inevitably to greater variance in the estimate of the integral. However, as the panel of Fig. 2 with only $N = 10$ points shows, the advantage of greater uniformity is only obtained if sufficiently many points of the Halton sequence are used in the integration. In practice, a good rule of thumb appears to be that the Halton points will be significantly more uniformly distributed than randomly selected points if $N \sim e^{d/2}$.

An important feature of the Halton sequence is that the points do not depend upon the number N. Consequently, if it is found that the error in the integration is too large after N points, then additional points can be generated without affecting the preceding calculations.

The cost of generating the Halton sequence is typically less than twice the cost of generating a corresponding sequence of random numbers. For example, 10,000 points of the Halton and random sequences in 60 dimensions were generated on a 386SX PC in 47 and 26 sec respectively. In the context of solving the RTE, the additional cost of the Halton sequence is negligible compared with the total cost of simulating the photon trajectories.

The Halton sequence is near optimal, in the sense that most other sequences with the same number of points will have a larger discrepancy. As an extreme example, N points selected on a uniform rectangular grid in d dimensions have discrepancy

$$D^{(N)} = O(d/N^{1/d}). \tag{44}$$

If d is large, then it is clear that the discrepancy of this set of points decreases very slowly with N. Indeed, once $d \geqslant 4$, integration using a rectangular grid of points becomes prohibitively expensive.

3. INTEGRATION OF THE RADIATIVE TRANSFER EQUATION

In order to demonstrate the greater efficiency of QMC integration of the RTE, both QMC and RMC integration were applied to the following test problems: (i) a uniform slab with conservative, isotropic scattering; (ii) a uniform slab with conservative scattering prescribed by a Henyey–Greenstein phase function with asymmetry $g = 0.75$; (iii) a Gaussian slab with conservative, isotropic scattering and an extinction coefficient given by

$$\gamma(\mathbf{x}) = 2z \exp(-\pi x^2), \tag{45}$$

for which the optical thickness varies along the x axis according to

$$\tau(\mathbf{x}) = \exp(-\pi x^2). \tag{46}$$

Conservative scattering provides the most stringent test for MC integration because the multiple scattering series is then most slowly convergent. Furthermore, the peaked phase function of problem 2 and the non-uniform geometry of problem 3 test the robustness and adaptability of QMC integration. In each case, the source was assumed to be the solar beam, and no diffuse radiance was assumed to be incident upon the medium.

The computer code followed photons backwards through the medium from collision to collision, up to a maximum of n collisions. The photon trajectories were generated from points z in the $(3n - 2)$ dimensional unit cube with components

$$\mathbf{z} = (\epsilon_1, \zeta_1, \eta_1, \epsilon_2, \zeta_2, \eta_2, \ldots, \epsilon_{n-1}, \zeta_{n-1}, \eta_{n-1}, \epsilon_n). \tag{47}$$

For each scattering order $k = 1, \ldots, n$, the trajectory from the exit point to the point of the kth collision was computed as follows: ϵ_1 determined the distance from the exit point, $\mathbf{x}_0$, to the previous scattering point, $\mathbf{x}_1$, while ζ_1 and η_1 determined the incident direction, $\mathbf{s}_1$, of the photon at $\mathbf{x}_1$; the next three components, $\epsilon_2, \zeta_2, \eta_2$, determined the distance from $\mathbf{x}_1$ to $\mathbf{x}_2$ and the incident direction, $\mathbf{s}_2$, of the photon at $\mathbf{x}_2$, and so on; ϵ_k determined the distance from $\mathbf{x}_{k-1}$ to $\mathbf{x}_k$, where the incident photon direction was taken to be that of the solar beam, $\mathbf{s}_*$. After computing the kth order radiance, the code continued the trajectory to the $(k + 1)$st collision. For QMC integration, the point $\mathbf{z}$ was selected from the Halton sequence, whereas for RMC integration all components of

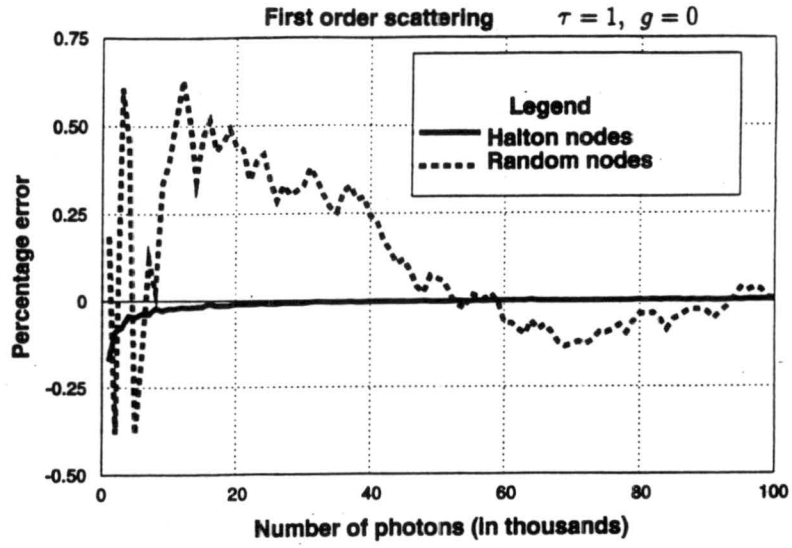

Fig. 3. First order scattering integral, $I_1^{(N)}$, plotted as a function of N for QMC and RMC integration of test problem 1. The scattering is conservative and isotropic. The medium is a uniform slab with optical thickness $\tau = 1$. The incident and exit zenith angles are $\cos\theta_* = -0.5$ and $\cos\theta_0 = 0.5$.

z were chosen randomly in the unit interval (0, 1). Thus, apart from the mechanism used to generate the sampling points, the same computer code was used for both QMC and RMC integration.

Values are given below for both the individual terms I_k and the partial sums S_n of the multiple scattering series. The estimates of these quantities, obtained by either QMC or RMC integration with N photon trajectories, are denoted by $I_k^{(N)}$ and $S_n^{(N)}$ respectively.

3.1. Test problem 1

Figures 3, 4, 5 and 6 show the convergence of $I_1^{(N)}$, $I_2^{(N)}$, $I_3^{(N)}$ and $S_{30}^{(N)}$ as functions of N, the number of photon trajectories, for both QMC and RMC in the case of a uniform slab with optical thickness $\tau = 1$. The scattering is in the principal plane with incident and exit zenith angles, denoted θ_* and θ_0, specified by

$$\mu_* = \cos\theta_* = -0.5, \quad \mu_0 = \cos\theta_0 = 0.5.$$

The faster convergence of QMC integration is clear. However, it is also apparent that the improvement in convergence deteriorates with increasing order of scattering. The reason is that the

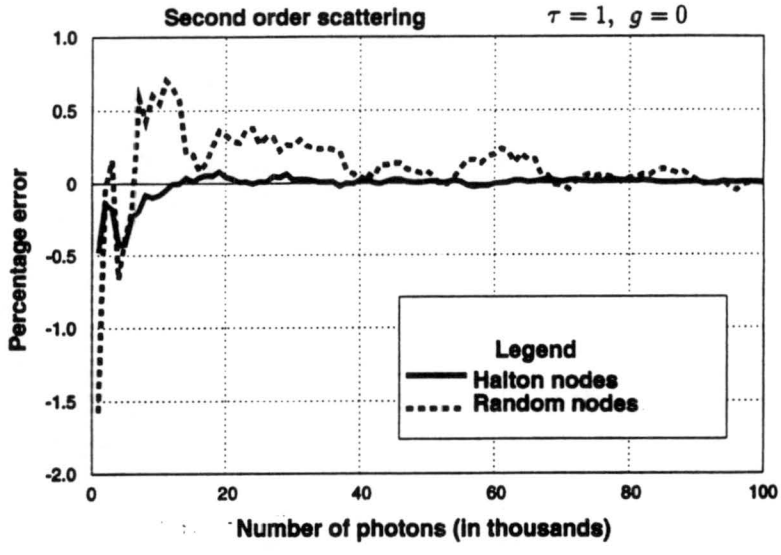

Fig. 4. Second order scattering integral, $I_2^{(N)}$, for the same conditions as Fig. 3.

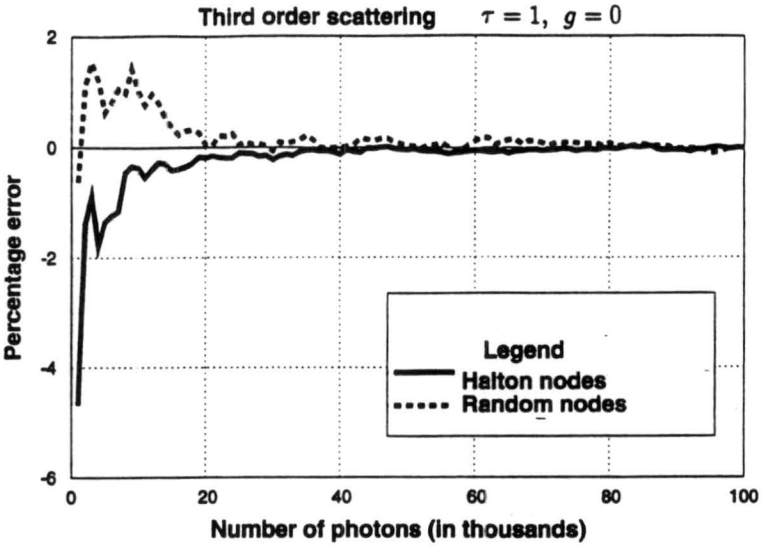

Fig. 5. Third order scattering integral, $I_3^{(N)}$, for the same conditions as Fig. 3.

dimension of the corresponding integration also increases, and QMC integration with the Halton sequence requires approximately $N \sim e^{d/2}$ points in order to cover the integration domain more effectively than randomly selected points. Therefore, it follows that the greatest advantage of QMC integration of the RTE will occur in optically thin media, where the multiple scattering series converges rapidly.

A more revealing comparison of the performance of QMC and RMC integration is the cost, measured in terms of the number of photons (in units of hundreds), required to achieve an accuracy of $\epsilon\%$. The cases displayed in Table 1 correspond to scattering in the principal plane, with

$$\mu_* = \cos\theta_* = -0.5,$$

$$\mu_0 = \cos\theta_0 = 0.9, 0.5, 0.1, -0.1, -0.5, -0.9, -1.0,$$

and optical thicknesses in the range

$$\tau = 1/8, 1/4, 1/2, 1, 2.$$

The prescribed error takes the values

$$\epsilon = 0.1, 0.2, 0.5, 1.0.$$

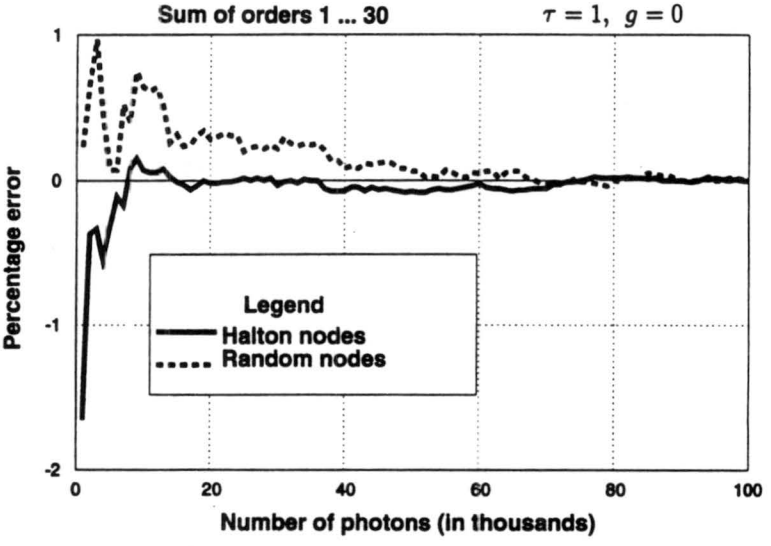

Fig. 6. Sum of the first 30 terms of the multiple scattering series, $S_{30}^{(N)}$, for the same conditions as Fig. 3.

Table 1. Comparison of the number of photons (in hundreds) required to achieve a specified accuracy of ϵ% for QMC and RMC integration of the RTE for test problem 1. An asterisk (*) indicates that the required accuracy was not reached after 10^5 photons. The reference values were taken from the Tables compiled by van de Hulst.[13] The column labels Q and R denote QMC and RMC, respectively. Also $\mu_* = \cos\theta_* = -0.5$, $\mu_0 = \cos\theta_0$.

τ	ϵ	$\mu_0 = 0.9$		$\mu_0 = 0.5$		$\mu_0 = 0.1$		$\mu_0 = -0.1$		$\mu_0 = -0.5$		$\mu_0 = -0.9$		$\mu_0 = -1.0$	
	%	Q	R	Q	R	Q	R	Q	R	Q	R	Q	R	Q	R
1/8	0.1	60	*	67	670	85	*	43	310	120	*	53	*	32	*
	0.2	43	730	20	380	8	*	28	200	39	*	44	*	9	970
	0.5	12	14	9	120	4	17	11	130	12	83	10	26	2	13
	1.0	3	12	2	1	2	5	3	15	5	6	4	16	1	2
1/4	0.1	61	*	76	670	90	*	60	*	110	*	71	*	37	*
	0.2	43	*	62	380	50	*	35	260	40	*	53	*	33	*
	0.5	20	160	14	130	4	18	11	170	16	83	17	29	9	41
	1.0	8	13	4	16	4	12	5	63	8	7	4	21	2	9
1/2	0.1	200	*	76	970	120	*	85	*	190	*	95	*	280	*
	0.2	180	*	71	320	60	*	70	*	40	*	53	*	58	960
	0.5	21	990	45	130	8	65	17	160	13	77	21	77	32	41
	1.0	12	17	12	17	4	18	8	63	8	8	4	17	9	13
1	0.1	350	*	100	*	93	*	650	*	290	*	580	*	350	970
	0.2	220	*	88	140	85	*	240	*	250	*	220	*	95	880
	0.5	35	*	46	100	26	120	77	*	13	30	20	33	58	50
	1.0	12	25	12	17	4	60	16	32	8	11	17	13	33	40
2	0.1	380	*	700	*	740	*	*	*	*	*	530	*	410	970
	0.2	240	*	97	*	85	*	960	*	730	*	240	990	350	930
	0.5	180	*	40	80	34	121	140	*	32	220	42	250	58	110
	1.0	30	*	12	16	4	63	39	*	13	23	31	81	39	90

The reference values of the radiance were taken from tables compiled by van de Hulst.[13] The multiple scattering series was summed to 30 orders in order to eliminate errors due to slow convergence. Where the specified accuracy was not achieved with 10^5 photons, an asterisk (*) has been inserted in the Table. Several conclusions are immediate. In nearly every case, QMC integration achieves the specified accuracy with far fewer photons than RMC integration. The cost increases steadily with the required precision for QMC integration, but not for RMC integration. Only rarely does RMC integration achieve an accuracy of 0.2% with fewer than 10^5 photons and, on the occasions it does, the cost jumps significantly above the cost of 0.5% accuracy. The cost of achieving a specified precision with QMC integration increases with optical thickness. The reason is that the contribution of higher order scattering becomes more significant with increasing optical thickness, necessitating more photons in order to evaluate the correspondingly higher dimensional integrals.

3.2. Test problem 2

The cost of obtaining high accuracy radiances increases when the phase function is sharply peaked, as in test problem 2. This is not surprising because the integrands in the multiple scattering integrals are now 'lumpy' functions, so many of the integration points are poorly targeted and fall outside the region where the integrands are large. In some problems, where the phase function is known only poorly, this problem can be avoided by replacing the phase function by a "ball and stick" model,

$$p(\mathbf{x}, \mathbf{s}, \mathbf{s}') = g(\mathbf{x})\delta(\mathbf{s}, \mathbf{s}') + (1 - g(\mathbf{x}))p'(\mathbf{x}, \mathbf{s}, \mathbf{s}'), \tag{48}$$

in which g is the asymmetry parameter of p, and p' is a smooth phase function whose asymmetry is zero. With this definition, the singular part of the phase function can be integrated analytically and the RTE reduces to scattering with phase function p' and modified scattering and extinction coefficients given by

$$\beta'(\mathbf{x}) = (1 - g(\mathbf{x}))\beta(\mathbf{x}), \tag{49}$$

and

$$\gamma'(\mathbf{x}) = \gamma(\mathbf{x}) - g(\mathbf{x})\beta(\mathbf{x}). \tag{50}$$

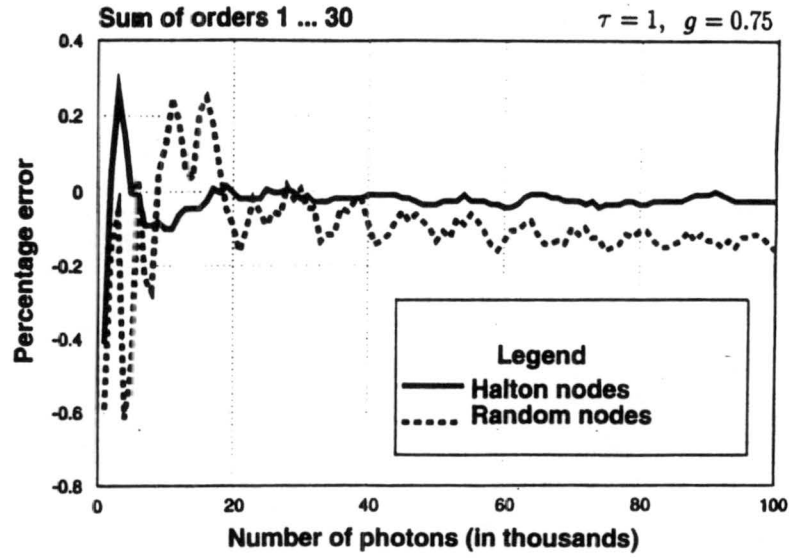

Fig. 7. Sum of the first 30 terms of the multiple scattering series, $S_{30}^{(N)}$, plotted as a function of N for QMC and RMC integration of test problem 2. The scattering is conservative with a Henyey–Greenstein phase function with asymmetry $g = 0.75$. The medium is a uniform slab with optical thickness $\tau = 1$. The incident and exit zenith angles are $\cos\theta_* = -0.5$ and $\cos\theta_0 = -0.5$.

However, if high accuracy calculations are required for a precisely specified phase function, then the additional cost is unavoidable.

Figure 7 shows the convergence of $S_{30}^{(N)}$ as a function of N, the number of photon trajectories, for both QMC and RMC. The optical thickness is $\tau = 1$, the scattering is in the principal plane, and the incident and exit zenith angles are given by

$$\mu_* = \cos\theta_* = -0.5, \quad \mu_0 = \cos\theta_0 = -0.5.$$

Table 2. Comparison of the number of photons (in hundreds) required to achieve a specified accuracy of ϵ% for QMC and RMC integration of the RTE for test problem 2. An asterisk (*) indicates that the required accuracy was not reached after 10^5 photons. The reference values were computed by QMC integration with 10^6 photons. The column labels Q and R denote QMC and RMC, respectively. Also $\mu_* = \cos\theta_* = -0.5$, $\mu_0 = \cos\theta_0$.

τ	ϵ	$\mu_0 = 0.9$		$\mu_0 = 0.5$		$\mu_0 = 0.1$		$\mu_0 = -0.1$		$\mu_0 = -0.5$		$\mu_0 = -0.9$		$\mu_0 = -1.0$	
	%	Q	R	Q	R	Q	R	Q	R	Q	R	Q	R	Q	R
1/8	0.1	*	*	470	*	97	*	39	*	2	17	21	240	240	*
	0.2	320	*	110	*	43	*	10	280	2	6	8	220	28	230
	0.5	120	*	30	89	16	*	2	60	1	2	1	14	19	170
	1.0	43	*	7	79	6	4	2	15	1	1	1	3	3	14
1/4	0.1	*	*	890	*	680	*	49	*	2	42	53	360	300	*
	0.2	*	*	120	260	54	*	39	320	2	17	9	240	230	*
	0.5	290	*	43	94	20	*	5	220	1	5	8	210	28	220
	1.0	62	*	30	89	6	8	2	34	1	2	2	7	19	130
1/2	0.1	*	*	*	760	*	*	450	*	11	*	290	*	410	*
	0.2	*	*	800	440	520	*	48	590	11	50	51	310	220	*
	0.5	510	*	120	150	56	*	39	240	2	7	10	220	120	*
	1.0	55	*	13	140	17	12	24	34	1	6	2	66	61	210
1	0.1	*	*	800	*	*	*	690	*	96	*	*	*	*	*
	0.2	*	*	380	*	*	*	450	*	40	170	*	*	*	*
	0.5	890	*	240	180	270	*	160	*	5	50	51	220	350	*
	1.0	490	*	63	140	20	32	49	240	2	7	10	100	140	*
2	0.1	*	*	*	*	*	*	*	*	820	*	*	*	*	*
	0.2	*	*	950	990	*	*	990	*	96	*	*	970	*	*
	0.5	920	*	380	170	360	*	280	*	61	220	110	540	*	*
	1.0	510	*	68	140	20	180	85	420	57	83	31	290	900	*

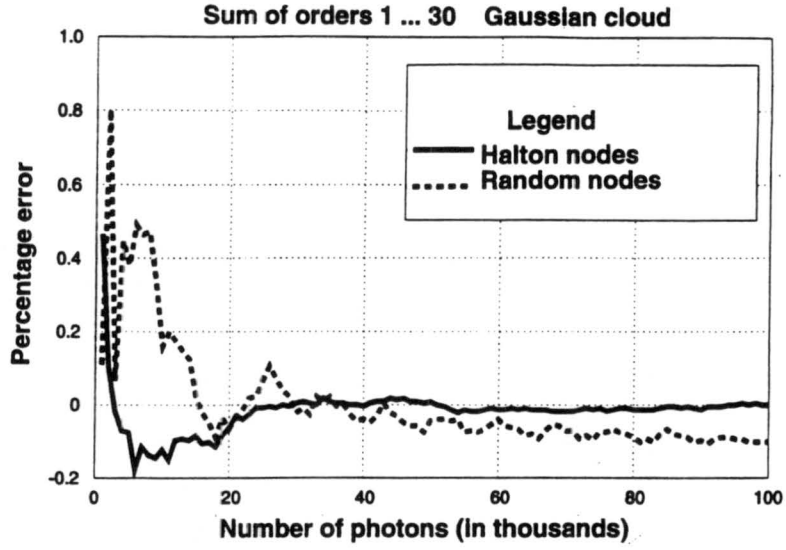

Fig. 8. Sum of the first 30 terms of the multiple scattering series, $S_{30}^{(N)}$, plotted as a function of N for QMC and RMC integration of test problem 3. The scattering is conservative and isotropic. The medium is a Gaussian slab with optical thickness $\tau = 1$ at the observation point. The incident and exit zenith angles are $\cos\theta_* = -0.5$ and $\cos\theta_0 = -0.5$.

Not only does the QMC integration converge more rapidly, but the RMC integration is slowly diverging from the correct answer after 10^5 photons. The faster convergence of QMC integration is typical of all the forward scattering directions.

The cost of achieving a specified accuracy is summarized for QMC and RMC integration in Table 2, the format of which is identical to Table 1. The reference values of the radiance were computed by QMC integration with 10^6 photons, sufficient to guarantee convergence. It is apparent from Table 2 that the costs are higher than for isotropic scattering, exactly as anticipated. Nevertheless, QMC integration is still more efficient.

3.3. Test problem 3

The results and conclusions for test problem 3 are very similar to those for problems 1 and 2. In order to make the test more stringent, the reflected and transmitted radiances were evaluated at the points (0, 0, 1) and (0, 0, 0) respectively, where the slab has its maximum optical thickness ($\tau = 1$). Figure 8 shows the convergence of $S_{30}^{(N)}$ as a function of N, the number of photon trajectories, for both QMC and RMC integration. The scattering is in the principal plane with incident and exit zenith angles given by

$$\mu_* = \cos\theta_* = -0.5, \quad \mu_0 = \cos\theta_0 = -0.5.$$

Table 3 shows the number of photons required to achieve an accuracy of $\epsilon\%$. The reference values were computed by QMC integration with 10^5 photons as it was clear that these values had converged. Both Fig. 8 and Table 3 demonstrate the superiority of QMC integration in this application with spatially varying optical properties.

Table 3. Comparison of the number of photons (in hundreds) required to achieve a specified accuracy of $\epsilon\%$ for QMC and RMC integration of the RTE for test problem 3. An asterisk (*) denotes that the specified accuracy was not reached after 10^5 photons. The reference values were computed by QMC integration with 10^5 photons. The column labels Q and R denote QMC and RMC, respectively. Also $\mu_* = \cos\theta_* = -0.5$, $\mu_0 = \cos\theta_0$.

τ	ϵ	$\mu_0 = 0.9$		$\mu_0 = 0.5$		$\mu_0 = 0.1$		$\mu_0 = -0.1$		$\mu_0 = -0.5$		$\mu_0 = -0.9$		$\mu_0 = -1.0$	
	%	Q	R	Q	R	Q	R	Q	R	Q	R	Q	R	Q	R
1	0.1	61	*	57	510	93	*	39	280	190	*	43	*	57	*
	0.2	35	*	54	380	17	*	19	140	18	99	17	79	51	*
	0.5	14	58	12	60	7	120	11	82	8	80	4	14	22	24
	1.0	8	14	2	16	1	58	3	21	1	1	1	11	2	13

4. ACCELERATED CONVERGENCE OF THE MULTIPLE SCATTERING SERIES

When scattering is nearly conservative, the number of terms required in the multiple scattering series increases so rapidly with the optical thickness that the cost of accurate MC calculations can become prohibitive when $\tau \geqslant 2$. For plane parallel geometry it is possible to estimate the rate of decay of the terms of the multiple scattering series,[13] thereby enabling the tail of the series to be summed analytically. However, for other geometries it is as costly to estimate the rate of decay of the terms of the series as it is to compute them, so other techniques are required. This section outlines one such technique.

After n iterations of the integral equation of radiative transfer, the radiance can be written

$$I = S_n + E_{n+1}, \tag{51}$$

where S_n is the partial sum of the first n terms and E_{n+1} is the error term defined in Eq. (12). Because the error term involves radiance that has been scattered at least n times, it might be argued in an intuitive way that this radiance ought to be diffuse when n is large, in which case the error term might be approximated by setting the radiance to a constant value, denoted C. This argument leads to

$$E_{n+1} = CR_{n+1}, \tag{52}$$

where

$$R_{n+1}(\mathbf{x}_0, \mathbf{s}_0) = \int_{u_0}^{x_0} d\mathbf{x}_1 \, t(\mathbf{x}_0, \mathbf{x}_1)\beta(\mathbf{x}_1) \int_\Omega d\Omega(\mathbf{s}_1) p(\mathbf{x}_1, \mathbf{s}_0, \mathbf{s}_1) \cdots$$
$$\cdots \times \int_{u_n}^{x_n} d\mathbf{x}_{n+1} \, t(\mathbf{x}_n, \mathbf{x}_{n+1})\beta(\mathbf{x}_{n+1}) \int_\Omega d\Omega(\mathbf{s}_{n+1}) p(\mathbf{x}_{n+1}, \mathbf{s}_n, \mathbf{s}_{n+1}). \tag{53}$$

The coordinate changes discussed in Sec. 1 allow R_{n+1} to be reduced to

$$R_{n+1}(\mathbf{x}_0, \mathbf{s}_0) = \int_0^1 d\epsilon_1 \int_0^1 d\zeta_1 \int_0^1 d\eta_1 \cdots \int_0^1 d\epsilon_n \int_0^1 d\zeta_n \int_0^1 d\eta_n \int_0^1 d\epsilon_{n+1}$$
$$\times \varpi(\mathbf{x}_1) \cdots \varpi(\mathbf{x}_{n+1}) a(\mathbf{x}_0, \mathbf{u}_0) \cdots a(\mathbf{x}_n, \mathbf{u}_n), \tag{54}$$

in which form it is clear that

$$0 \leqslant R_n \leqslant 1,$$

that R_n is a decreasing sequence,

$$R_{n+1} \leqslant R_n,$$

and that

$$\lim_{n \to \infty} R_n = 0.$$

If the radiance is also replaced by C on the left of Eq. (51), so that

$$C = S_n + CR_{n+1}, \tag{55}$$

then the following suggestive result is obtained:

$$I = C = \frac{S_n}{1 - R_{n+1}}. \tag{56}$$

With this motivation, define

$$Q_n(\nu) = \frac{S_n}{1 - \nu R_{n+1}} \tag{57}$$

for any ν in the range (0, 1), and observe that, whatever the value of ν, the sequence so defined converges to the true radiance I because R_{n+1} converges to zero. It is easy to establish the following result.

Let T_n denote the sequence,

$$T_n = \frac{I_n}{R_n S_n - R_{n+1} S_{n-1}}, \tag{58}$$

and let ν_* denote its minimum value,

$$\nu_* = \inf_{n \geq 0} T_n. \tag{59}$$

Then, for all ν in the range $0 \leq \nu \leq \nu_*$, (i) the sequence $Q_n(\nu)$ is monotonically increasing, and (ii) the sequence $Q_n(\nu_*)$ converges to the true radiance faster than $Q_n(\nu)$,

$$|I - Q_n(\nu)| \geq |I - Q_n(\nu_*)| \text{ for all } n. \tag{60}$$

In particular, $Q_n(\nu_*)$ converges to the true radiance faster than S_N. Consequently, by computing the terms of the sequence T_n and estimating ν_* by the minimum of the computed terms, it is possible to construct a sequence which converges to the true radiance faster than the standard sequence of partial sums.

The proof of the accelerated convergence result is straightforward. First, the condition that $Q_n(\nu)$ should be monotonic leads, after a little manipulation, to the result that

$$Q_n - Q_{n-1} = \frac{I_n + \nu Q_{n-1}(R_{n+1} - R_n)}{1 - \nu R_{n+1}} \geq 0. \tag{61}$$

The denominator is positive because both ν and R_{n+1} are bounded above by 1, so the numerator also must be positive,

$$I_n + \nu Q_{n-1}(R_{n+1} - R_n) \geq 0. \tag{62}$$

After insertion of the definition of $Q_n(\nu)$, the inequality reduces to

$$I_n \geq \nu(R_n S_n - R_{n+1} S_{n-1}), \tag{63}$$

or

$$\nu \leq T_n, \tag{64}$$

an inequality which is certainly true for all $\nu \leq \nu_*$. In order to prove that $Q_n(\nu_*)$ converges more rapidly that $Q_n(\nu)$, note that

$$Q_n(\nu) \leq Q_n(\nu_*) \quad \text{if} \quad \nu \leq \nu_*. \tag{65}$$

Consequently,

$$I - Q_n(\nu) \geq I - Q_n(\nu_*). \tag{66}$$

Because both sequences $Q_n(\nu)$ and $Q_n(\nu_*)$ converge to I monotonically from below, the result quoted in Eq. (60) follows.

Figure 9 compares the convergence of the sequences S_n and $Q_n(\nu^*)$ for test problem 1 with an optical thickness of $\tau = 2$ and incident and exit zenith angles of $\cos\theta_* = -0.5$ and $\cos\theta_0 = 0.5$. The parameter ν_* was estimated from the first 30 terms of the multiple scattering series, which were calculated by QMC integration with 10^5 photons to minimize errors. It is apparent that the Q_n sequence converges more rapidly. Figures 10, 11 and 12 show the corresponding results for optical thicknesses of $\tau = 4$, 8 and 16. Although the sequence S_n shows no sign of convergence in Figs. 10, 11 and 12, the Q_n sequence converges rapidly and the final values are in error by 0.08, 1.4 and 6.3% respectively.

Figure 13 compares the standard and accelerated series for test problem 2 with $\tau = 4$ and $g = 0.75$, while Fig. 14 shows the corresponding result for the Gaussian slab of test problem 3. In each case the acceleration technique leads to improved convergence, demonstrating that the technique is applicable to peaked phase functions and non-uniform spatial distributions of the optical properties. If the improvement in the rate of convergence is less dramatic for the Gaussian slab, the reason is simply that the cloud is so thin (with maximum optical thickness of 1) that the multiple scattering series converges rapidly in any case.

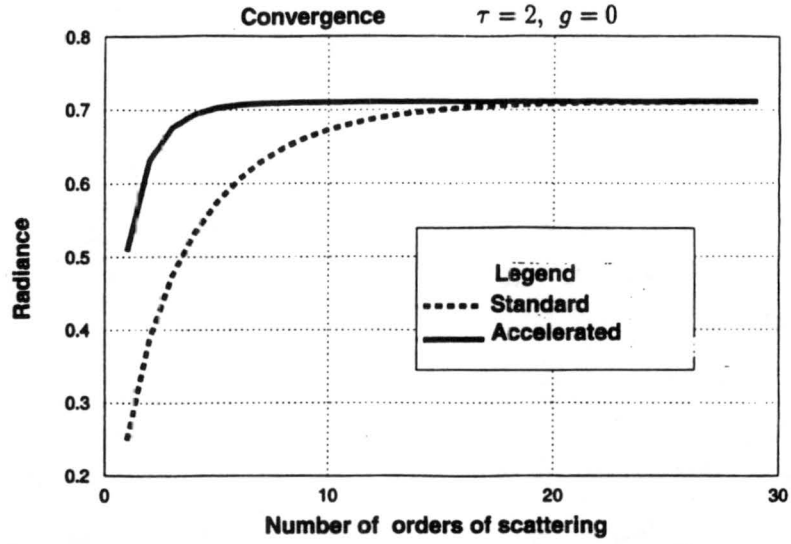

Fig. 9. Convergence of the sequences S_n and $Q_n(v^*)$ for test problem 1. The scattering is conservative and isotropic. The medium is a uniform slab with optical thickness $\tau = 2$. The incident and exit zenith angles are $\cos\theta_* = -0.5$ and $\cos\theta_0 = 0.5$.

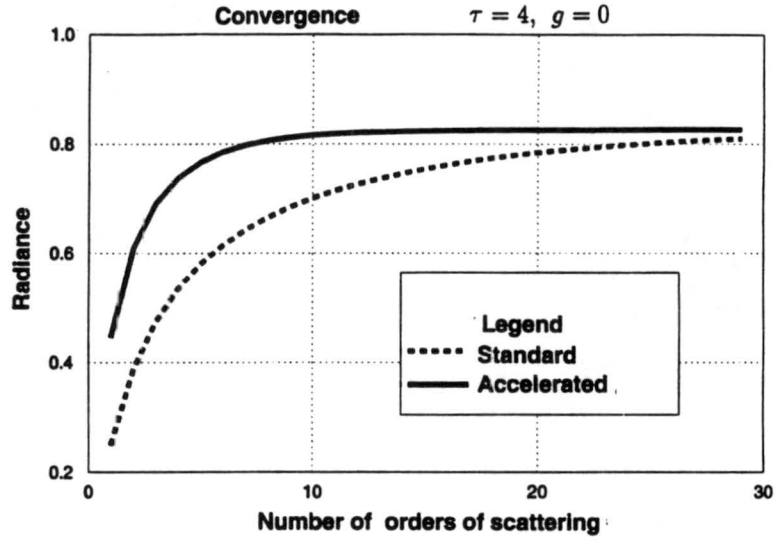

Fig. 10. As for Fig. 8 except $\tau = 4$.

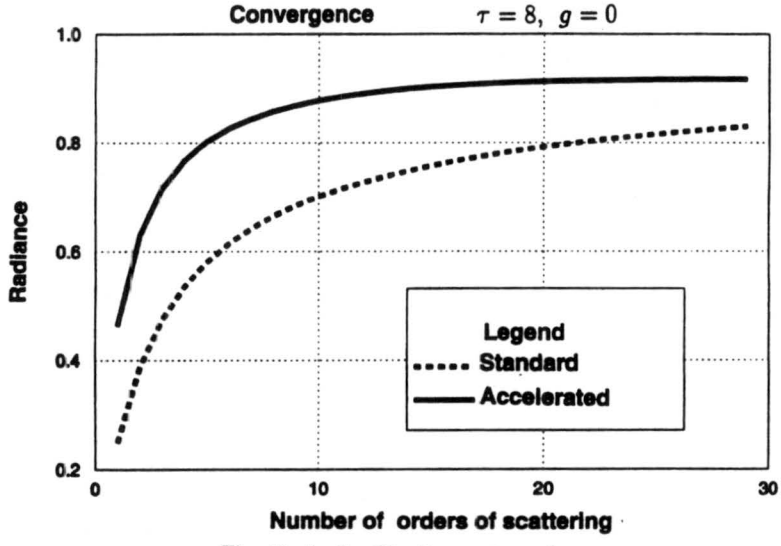

Fig. 11. As for Fig. 8 except $\tau = 8$.

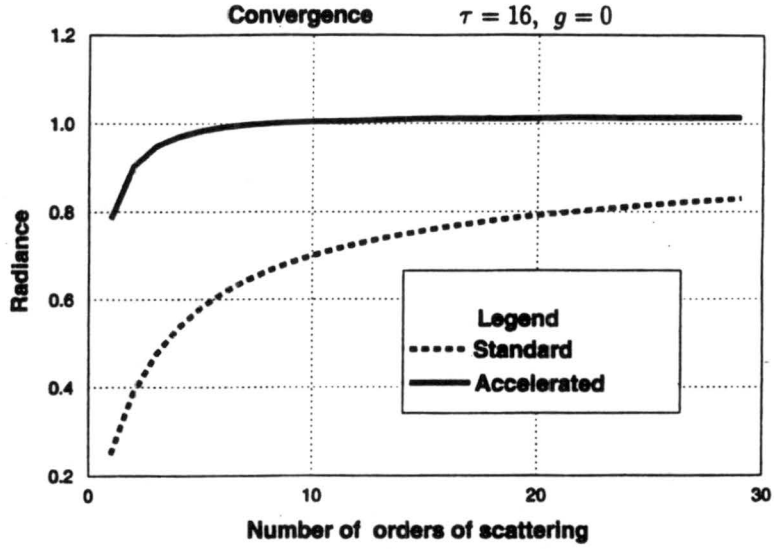

Fig. 12. As for Fig. 8 except $\tau = 16$.

The practical implementation of the convergence acceleration strategy calls for the calculation of the remainder integrals R_n. Fortunately, the additional cost is negligible compared with the cost of simulating the photon trajectories.

The accelerated convergence technique will fail if $\nu_* = 0$. However, it is possible to prove that ν_* is strictly positive under a wide variety of conditions, perhaps the simplest of which is the common assumption that the phase function is bounded away from zero. More precisely, let $p^{(-)} > 0$ denote the minimum value of $p(\mathbf{x}, \mathbf{s}, \mathbf{s}')$ for any position $\mathbf{x}$ in the medium and any incident and exit directions $\mathbf{s}'$ and $\mathbf{s}$, and let $t^{(-)} > 0$ denote the minimum of the transmittance $t(\mathbf{x}, \mathbf{u})$ for any $\mathbf{x}$ in the medium with boundary point $\mathbf{u}$ determined by the direction of the solar beam. Then it follows easily from Eq. (28) that

$$I_{n+1} \geqslant \frac{F}{4\pi} p^{(-)} t^{(-)} \int_0^1 d\epsilon_1 \int_0^1 d\zeta_1 \int_0^1 d\eta_1 \cdots \int_0^1 d\epsilon_n \int_0^1 d\zeta_n \int_0^1 d\eta_n \int_0^1 d\epsilon_{n+1} \times \varpi(\mathbf{x}_1) \cdots \varpi(\mathbf{x}_{n+1}) a(\mathbf{x}_0, \mathbf{u}_0) \cdots a(\mathbf{x}_n, \mathbf{u}_n). \quad (67)$$

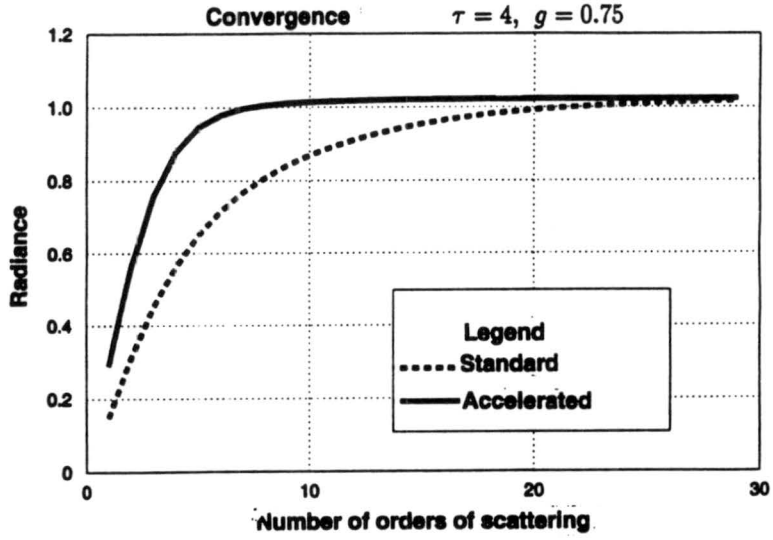

Fig. 13. Convergence of the sequences S_n and $Q_n(\nu^*)$ for test problem 2. The scattering is conservative with a Henyey–Greenstein phase function with asymmetry $g = 0.75$. The medium is a uniform slab with optical thickness $\tau = 4$. The incident and exit zenith angles are $\cos\theta_* = -0.5$ and $\cos\theta_0 = 0.5$

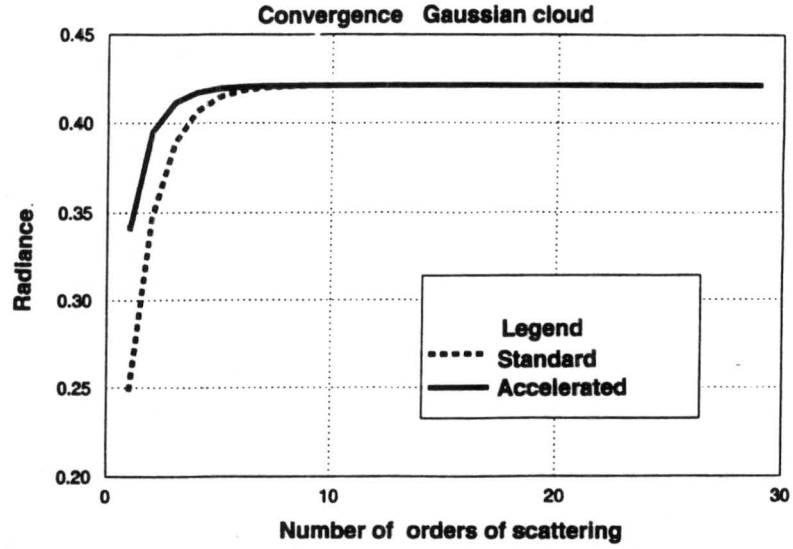

Fig. 14. Convergence of the sequences S_n and $Q_n(\nu^*)$ for test problem 3. The scattering is conservative and isotropic. The medium is a Gaussian slab with optical thickness $\tau = 1$ at the observation point. The incident and exit zenith angles are $\cos\theta_* = -0.5$ and $\cos\theta_0 = 0.5$.

Consequently, if

$$c = \frac{F}{4\pi} p^{(-)} t^{(-)}, \tag{68}$$

then

$$I_{n+1} \geqslant cR_{n+1} \tag{69}$$

and straightforward manipulation yields that

$$T_n \geqslant \frac{cR_n}{R_n S_n - R_{n+1} S_{n-1}} \geqslant \frac{c}{S_n} \geqslant \frac{c}{I} > 0. \tag{70}$$

This establishes that ν_* is bounded away from zero.

It is to be stressed that the technique described here is not particular to any scattering phase function or scattering geometry. It is robust and can be applied equally to RMC and QMC, although the latter has the advantage that the individual terms of the scattering series will be calculated more accurately for less cost.

CONCLUSIONS

The numerical experiments described in this paper show that (i) QMC integration with the Halton sequence of points is more efficient than RMC integration with randomly chosen points; (ii) the efficiency gain is greatest when the medium is optically thin, so that low order scattering dominates; (iii) the extra overhead incurred with QMC integration is negligible; (iv) the convergence acceleration technique is robust and leads to a significant improvement in the range of optical thicknesses to which Monte Carlo integration can be applied efficiently.

Acknowledgements—This work was carried out while the author was on sabbatical leave from CSIRO at the Department of Atmospheric Sciences, Colorado State University. It is a pleasure to acknowledge the hospitality of the department as well as enjoyable discussions with both K. A. Fuller and G. L. Stephens. Funding was provided in part by DOE grant DE-FG02-90ER61067 and NPS grant NOAA-NPS-NA90RAH00077.

REFERENCES

1. M. J. Weissbluth, J. M. Davis, and S. K. Cox, *Atmos. Environ.* **21,** 703 (1987).
2. T. Kobayashi, *J. Atmos. Sci.* **46,** 2208 (1989).
3. R. M. Welch and B. A. Wielicki, *J. Atmos. Sci.* **46,** 1384 (1989).
4. G. L. Stephens, *J. Atmos. Sci.* **45,** 1818 (1988).
5. G. L. Stephens, *J. Atmos. Sci.* **45,** 1837 (1988).

6. T. B. McKee and S. K. Cox, *J. Atmos. Sci.* **31,** 1885 (1974).
7. G. A. Titov, *J. Atmos. Sci.* **47,** 24 (1990).
8. G. I. Marchuk, G. A. Mikhailov, M. A. Nazaraliev, R. A. Darbinjan, B. A. Kargin, and B. S. Elepov, *The Monte Carlo Methods in Atmospheric Optics*, Springer Series in Optical Sciences, Springer, Berlin (1980).
9. E. W. Hobson, *The Theory of Functions of a Real Variable and the Theory of Fourier's Series*, Vol. I, Cambridge Univ. Press, London (1927).
10. H. Niederreiter, *Bull. Am. Math. Soc.* **84,** 957 (1978).
11. J. H. Halton, *Numer. Math.* **2,** 84 (1960).
12. J. H. Halton and G. B. Smith, *Commun. ACM* **7,** 701 (1964).
13. H. C. van de Hulst, *Multiple Light Scattering. Tables, Formulas and Applications*, Vols. 1 and 2, Academic Press, New York, NY (1980).

Chapter V Summary and Conclusions

An expression for the scattering cross sections of externally aggregated spheres has been obtained as a sum over cross sections associated with all realizable pairings of spheres in the cluster. This expression can be recast into a form which closely parallels that found for the scattering cross sections of single spheres wherein the the Lorenz-Mie coefficients are replaced by coefficients that characterize the geometry of the cluster and its electrodynamic response to the incident radiation. The summation over pairwise cross sections is found to offer an important numerical advantage over the Lorenz-Mie analogue for clusters.

Four relations satisfied by the translation coefficients have been derived for, it is believed, the first time. These relations provide useful convergence criteria for calculation of the pairwise cross sections. Comparisons of the scattering cross sections found in this work are made with those derived in two other investigations. An expression for the scattering cross sections of noninteracting dipoles is also provided. Applications of the theory developed in the present work will be made to particles of interest in climate and visibility studies in Chapter III.

In summarizing the findings of Chapter 2, it is important to first note the numerical efficacy of the series expansions for the scattering cross sections of clusters given in Eqs. 59 and 60 of Chapter I compared to straightforward numerical integration of the Poynting flux. The expansions avoid the following pitfalls: (1) The number of oscillations in the differential scattering cross section of a droplet increases dramatically with optical size, thereby requiring very high angular resolution of the integrand when hosts with large size parameters are involved. (2) When the carbon grains are very small relative to the host particle, the extinction cross section of the carbon/droplet system is dominated almost entirely by the scattering cross section of the host. The quantity $\sigma_e - \sigma_s$ can easily be of the order 10^{-6} or less and hence the integral must be evaluated with a very high precision. (3) The structure of the electric field at the surface of the host is quite complicated and therefore the absorption cross section of a small carbon grain is extremely sensitive to orientation. Orientation averages require a high resolution in α. (The calculations summarized in Tables I-III were based on a sampling frequency of 1°.) This makes it all the more imperative that the integrals over the scattering angles θ and ϕ be evaluated expeditiously. It is here that the order-of-scattering approach[5] plays its most important role, from a numerical standpoint, since the smaller the adsorbed grain, the fewer terms are needed in the multiple scattering series from which the scattering coefficients and cross sections are found. In fact, only one exchange between the 0.01μm carbon grains and droplets was necessary in order to determine σ_s to the required precision. For larger grains, as many as five orders of scattering were needed. (4) When large numbers of spheres are involved the intereference between them will impose an additional oscillation in the differential cross sections of the clusters. The more monomers there are comprising the cluster, the greater the number of these interference fringes. These oscillations are analogous to multiple slit diffration patterns. (The number of spherules in the carbon aggregates studied thus far has not been sufficient for this effect to have been of significance.)

The effects of scavenging of atmospheric carbon by haze and cloud droplets has been considered in terms of the orientations of the resulting composite particles—carbon grains

residing on droplet surfaces—with respect to the incident fields. Orientation- and polarization-averaged absorption efficiencies were then determined and from these it appears that the more finely divided the carbon, the more efficient is its absorption of light when it resides on the surface of a sulfate host. This efficiency, however, has not been found to be more than about a factor of two greater than that of free carbon. Carbon adsorbed onto cloud droplets appears thus far to absorb slightly less light than when it exists as isolated grains within the cloud volume.

Approximations of the absorption properties of soot aggregates at visible wavelenghts in terms of single sphere properties appear, within the limits of the work presented here, to produce errors of not more than about $10-15\%$ for monomers less than about 0.05μm in radius. The scattering properties likewise approximated, tend to produce similar errors for monomer radii less than about 0.01μm or on the order of 0.10μm, but there is a transition region which includes radii of 0.05μm for which these single sphere approximations for scattering may be grossly in error.

Appendix

The translation coefficients $\widetilde{A}_{\mu\nu}^{mn}$ and $\widetilde{B}_{\mu\nu}^{mn}$ appearing in Eq. (54) are of the form

$$\widetilde{A}_{\mu\nu}^{mn} = \sum_{p=|n-\nu|}^{n+\nu} [n(n+1)+\nu(\nu+1)-p(p+1)]\tilde{w}_p(\ell,\ell';m,n,\mu,\nu) \tag{A.1}$$

and

$$\begin{aligned}\widetilde{B}_{\mu\nu}^{mn}(k\mathbf{d}_{\ell,\ell'}) = \imath\, kd_{\ell,\ell'} \Bigg[& 2\mu\cos\theta_{\ell,\ell'} \sum_p \tilde{w}_p(\ell,\ell';m,n,\mu,\nu) + \\ \sin\theta_{\ell,\ell'} \Big(& (\nu-\mu)(\nu+\mu+1)\exp[\imath\phi_{\ell,\ell'}] \sum_p \tilde{w}_p(\ell,\ell';m,n,\mu{+}1,\nu) + \\ & \exp[-\imath\phi_{\ell,\ell'}] \sum_p \tilde{w}_p(\ell,\ell';m,n,\mu{-}1,\nu) \Big) \Bigg],\end{aligned} \tag{A.2}$$

where

$$\begin{aligned}\tilde{w}_p(\ell,\ell';m,n,\mu,\nu) = (-1)^{\mu}\imath^{(n-\nu-p)} & \frac{2\nu+1}{2\nu(\nu+1)} \times \\ & a(m,n,-\mu,\nu,p)\, j_p(kd_{\ell,\ell'})\, P_p^{m-\mu}(\cos\theta_{\ell,\ell'})\exp[\imath(m-\mu)\phi_{\ell,\ell'}.\end{aligned} \tag{A.3}$$

The $a(m,n,\mu,\nu,p)$ are known as Gaunt coefficients and are defined by the expression

$$P_n^m(\cos\theta)P_\nu^\mu(\cos\theta) = \sum_{p=|n-\nu|}^{n+\nu} a(m,n,\mu,\nu,p)P_p^{m+\mu}(\cos\theta),$$

and hence

$$a(m,n,\mu,\nu,p) = \frac{2p+1}{2}\frac{(p-m-\mu)!}{(p+m+\mu)!}\int_{-1}^{1} P_n^m(x)P_\nu^\mu(x)P_p^{m+\mu}(x)\,dx. \tag{A.4}$$

In Eqs. (A3) and (A4) $kd_{\ell,\ell'}$ is the line segment joining the centers of spheres ℓ and ℓ', $\theta_{\ell,\ell'}$ corresponds to the angle between $kd_{\ell,\ell'}$ and the ${}^{\ell}z$-axis, and $\phi_{\ell,\ell'}$ is the azimuthal coordinate of the ℓth sphere in the ℓth coordinate system.

$$\lim_{kd_{\ell,\ell'}\to 0} \widetilde{A}_{\mu,\nu}^{m,n}(kd_{\ell,\ell'}) = \begin{cases} 0, & \text{if } m \neq \mu; \\ \lim\limits_{kd_{\ell,\ell'}\to 0} \widetilde{A}_{m,n}^{m,n}(kd_{\ell,\ell'}), & \text{if } m = \mu, \end{cases} \tag{A.5}$$

but

$$\begin{aligned}\lim_{kd_{\ell,\ell'} \to 0} \widetilde{A}^{m,n}_{m,n}(kd_{\ell,\ell'}) &= (-1)^m(2n+1)\frac{1}{2}\int_{-1}^{1} P_n^m(x)P_n^{-m}(x)\,dx \\ &= (-1)^m(2n+1)\frac{1}{2}\frac{(n-m)!}{(n+m)!}\int_{-1}^{1} P_n^m(x)P_n^m(x)\,dx\end{aligned} \tag{A.6}.$$

Thus

$$\lim_{kd_{\ell,\ell'} \to 0} \widetilde{A}^{m,n}_{\mu,\nu}(kd_{\ell,\ell'}) = \delta_{m,\mu}\delta_{n,\nu} \tag{A.7}$$

Clearly,

$$\lim_{kd_{\ell,\ell'} \to 0} \widetilde{B}^{m,n}_{\mu,\nu}(kd_{\ell,\ell'}) = 0 \tag{A.8}$$

References

1. K. A. Fuller, "Optical resonances and two-sphere systems," Appl. Opt. **30** 4716–4731 (1991)

2. F. Borghese, P. Denti, R. Saija, G. Toscano, and O. I. Sindoni, "Multiple electromagnetic scattering from a cluster of spheres. I. Theory," Aerosol Sci. Technol. **4**, 227–235(1987).

3. D. W. Mackowski, "Analysis of radiative scattering for multiple sphere configurations," Proc. R. Soc. Lond. A **433**, 599–614(1991).

4. J. Podzimek, "Physical properties of coarse aerosol particles and haze elements in a polluted urban-marine environment," J. Aerosol Sci. **21**, 299–308(1990).

5. G. L. Stephens and S.-C. Tsay, "On the cloud absorption anomaly," Q. J. R. Meteorol. Soc. **116**, 671–704(1990).

6. K. A. Fuller, Ph.D. dissertation, Department of Physics, Texas A&M University, 1987

7. G. Arfken, *Mathematical Methods for Physicists, 3rd Edition*, (Academic Press, Orlando, 1985).

8. C. F. Bohren and D. R. Huffman, *Absorption and Scattering of Light by Small Particles*, (John Wiley and Sons, New York, 1983).

9. J. H. Bruning and Y. T. Lo, "Multiple scattering of em waves by spheres parts I & II," IEEE Trans. Ant. Prop. **AP-19**, 378–400 (1971), J. H Bruning and Y. T. Lo, "Multiple Scattering by Spheres," Antenna Laboratory Report No. 69-5, Antenna Laboratory, Department of Electrical Engineering, Engineering Experiment Station, University of Illinois, Urbana, Illinois.

10. S. Stein, "Addition theorems for spherical wave functions," Quart. Appl. Math. **19**, 15–24 (1961).

11. O. R. Cruzan, "Translation addition theorems for spherical vector wave functions," Quart. Appl. Math. **20**, 33–40 (1962).

12. K. A. Fuller and G. W. Kattawar, "Consummate solution to the problem of classical electromagnetic scattering by ensembles of spheres. I: Linear Chains," Opt. Lett. **13**, 90–92 (1988).

13. K. A. Fuller and G. W. Kattawar, "Consummate solution to the problem of classical electromagnetic scattering by ensembles of spheres. II: Clusters of arbitrary configuration," Opt. Lett. **13**, 1063–1065 (1988).

14. F. Borghese, P. Denti, R. Saija, and O. I. Sindoni, "Reliability of the theoretical description of electromagnetic scattering from non-spherical particles," J. Aerosol Sci. **20**, 1079–1081(1989).

15. M. A. Jarzembski and V. Srivastava , "Electromagnetic field enhancement in small liquid droplets using geometric optics," Appl. Opt. **28**, 4962–4965 (1989).

16. K. A. Fuller, "Scattering and absorption by inhomogeneous spheres and sphere aggregates," in *Laser Applications in Combustion and Combustion Diagnostics*, L. C. Liou, ed. (Proceedings of SPIE Conference 1862, 1993).

17. C. M. Sorensen, J. Cai, and N. Lu, "Light-scattering measurements of monomer size, monomers per aggregate, and fractal dimension for soot aggregates in flames," Appl. Opt. **31**, 6547-6557(1992).

Figure Captions

Figure 1. The single sphere scattering geometry: reduced symmetry case.

Figure 2. The scattering geometry for the multiple-origin system used in the study of sphere clusters.

Figure 3. Gram-specific absorption cross sections for a carbon grain located on the surface of a spherical sulfate aerosol. The carbon particle has a radius of 0.05 μm and a refractive index of $1.80+0.5i$. The radius and refractive index of the sulfate particle are 0.50 μm and $1.52 + 0.0i$, respectively. The straight line corresponds to the gram-specific absorption cross section of an isolated carbon grain. In the inset, the size of the carbon particle relative to the sulfate aerosol is drawn to scale.

Figure 4. Same as Figure 1, but with either a 0.1 or 0.01 μm carbon grain. The heavy and light lines show the absorption cross sections of isolated 0.1 and 0.01 μm grains, respectively. The inset is drawn to scale for the 0.1μm carbon sphere.

Figure 5. Same as Figure 1, but with a 1.0 μm sulfate particle.

Figure 6. Same as Figure 2, but with a 1.0 μm sulfate particle.

Figure 7. Same as Figure 1, but with a 3.0 μm water droplet. The refractive index of water is taken to be $1.33 + 0.0i$.

Figure 8. Same as Figure 2, but with a 3.0 μm water droplet.

Figure 9. Same as Figure 1, but with a 5.0 μm water droplet.

Figure 10. Same as Figure 2, but with a 5.0 μm water droplet.

Figure 11. Mass extinction and absorption cross sections of a linear chain of five carbon spheres. Each of the monomers has a radius of 0.01 μm and a refractive index of $1.8 + 0.5i$. The respective cross sections of an isolated sphere and an equivalent volume sphere are also shown.

Figure 12. Same as Fig. 9, but with monomer radii of 0.05 μm.

Figure 13. Same as Fig. 9, but with monomer radii of 0.10 μm.

Figure 14. Same as Figure 9, but the monomers now form a close-packed hexahedron.

Figure 15. Same as Fig. 12, but with monomer radii of 0.05 μm.

Figure 16. Same as Fig. 12, but with monomer radii of 0.10 μm.